

Active Metal-Insulator-Metal Plasmonic Devices

Thesis by
Kenneth Alexander Diest

In Partial Fulfillment of the Requirements
for the Degree of
Doctor of Philosophy



California Institute of Technology
Pasadena, California

2010

(Defended September 8, 2009)

© 2010

Kenneth Alexander Diest

All Rights Reserved

This thesis is dedicated to

Carol Ann Diest, Hadley Ann Diest, and Edison Allen Diest

who will have the chance to read this thesis

and

Professor Richard Wood, Mr. Robert Stewart, and Hanna Diest

who will not.

Acknowledgements

They say that life's all about the journey, and at the start of this journey I was working as an engineer at Hewlett-Packard. After deciding I didn't have enough expertise in any one area to really drive the field in which I was working, I headed off to graduate school. After five years at Caltech, it's definitely about the journey just as much as it is the goal. On paper, you're a doctor the day you graduate from the Ph.D. program. In reality, it happens somewhere along the way. As painful and stressful as the whole process was, it's definitely made me a better person. Not only because of the additional mountain of knowledge I've digested, but because of the people I've met along the way. Without the help of a great many people, I would not have written this thesis.

The first person I need to thank is my advisor, Harry Atwater. As well as providing all the labs and funding necessary for me to do my research; he was also a constant source of ideas for the projects I was involved in. He encouraged me to attend conferences and made it possible to work with other groups on campus as well as with LETI in France.

My parents deserve as much thanks as anyone. I always tell people that the greatest blessing that my sister and I had was our parents dedication to our educations'. They gave up a great many things so that we could have every opportunity to grow academically, athletically, and musically.

The five years here at Caltech weren't always easy and my close friends were extremely helpful in getting through all the challenges, academic and otherwise. I couldn't have gotten through graduate school without the help of Merrielle Spain, Melissa Archer, Eyal Feigenbaum, Ryan Briggs, Glenn Garrett, and Krista Langeland.

Young-Bae Park was very helpful as a mentor for my first two years at Caltech. He taught me about ferroelectrics, ion implantation-induced layer transfer, piezoresponse force microscopy, how to write a scientific paper, and where to find the best Korean food near Caltech. He was a constant source of new ideas, and discussions with him lead me to the idea for the silver bonding project.

The difficulty in navigating all the labs and equipment within the Atwater Group is on the order of developing cold fusion. A number of individuals within the lab were especially helpful with this task over the years. Luke Sweatlock and Matt Dicken used their wit and sarcasm to guide me through the first few years of graduate school and introduced me to the art of poker. In addition, Luke's work on the plasMOSTor project as well as all things plasmonic were key in getting helping me get up to speed. Luke also provided plenty of "help" with the more subtle aspects of L^AT_EX. Mike Kelzenberg knows everything about the optics labs and his desk is the best place

on campus to find batteries. Vivian Ferry was especially helpful when analyzing FDTD and the slit scattering results. Imogen Pryce was helpful with everything in the lab and group during my final years at Caltech. Stan Burgos was helpful with questions about the FIB and FDTD. Jennifer Dionne deserves thanks for extracting the TEM sample for the silver bonding paper and her FIB and simulation work on the plasMOSTor project.

I also want to thank everyone else in the Atwater Group including: Koray Aydin, Julie Biteen-Johnson, Shannon Boettcher, Dennis Callahan, Davis Darvish, Michael Deceglie, Michael Filler, Carrie Hofmann, Seokmin Jeon, Greg Kimball, Marina Leite, Henri Lezec, Jeremy Munday, Keisuke Nakayama, April Neidholdt, Deirdre O'Carroll, Domenico Pacifici, Morgan Putnam, Christine Richardson, Katsu Tanabe, Dan Turner-Evans, and Emily Warmann.

The staff of the Kavli Nanoscience Institute were very helpful. Thanks to Guy Derosé, Mary Sikora, Nils Asplund, Bophan Chhim, Carol Garland, and Melissa Melendes. None of the focused ion beam work or the silver bonding transmission electron microscope work would have been possible without them. Also, thanks to the administrators that ran Watson while I was there: Eleonora Vorobieff, Irene Loera, and Cierina Marks.

I apologize to anyone I've forgotten, or anything people have helped me with that I've left off the list.

Finally, I'd like to thank my thesis examination committee: Professors Amnon Yariv, Kaushik Bhattacharya, Chiara Daraio, and Harry A. Atwater.

Kenneth Diest
September 2009
Pasadena, CA

Abstract

As the field of photonics constantly strives for ever smaller devices, the diffraction limit of light emerges as a fundamental limitation in this pursuit. A growing number of applications for optical “systems on a chip” have inspired new ways of circumventing this issue. One such solution to this problem is active plasmonics. Active plasmonics is an emerging field that enables light compression into nano-structures based on plasmon resonances at a metal-dielectric interface and active modulation of these plasmons with an applied external field. One area of active plasmonics has focused on replacing the dielectric layer in these waveguides with an electro-optic material and designing the resulting structures in such a way that the transmitted light can be modulated. These structures can be utilized to design a wide range of devices including optical logic gates, modulators, and filters.

This thesis focuses on replacing the dielectric layer within a metal-insulator-metal plasmonic waveguide with a range of electrically active materials. By applying an electric field between the metal layers, we take advantage of the electro-optic effect in lithium niobate, and modulating the carrier density distribution across the structure in n-type silicon and indium tin oxide.

The first part of this thesis looks at fabricating metal-insulator-metal waveguides with ion-implantation induced layer transferred lithium niobate. The process is analyzed from a thermodynamic standpoint and the ion-implantation conditions required for layer transfer are determined. The possible failure mechanisms that can occur during this process are analyzed from a thin-film mechanics standpoint, and a metal-bonding method to improve successful layer transfer is proposed and analyzed. Finally, these devices are shown to naturally filter white light into individual colors based on the interference of the different optical modes within the dielectric layer. Full-field electromagnetic simulations show that these devices can preferentially couple to any of the primary colors and can tune the output color of the device with an applied field.

The second part of this thesis looks at fabricating metal-insulator-metal waveguides with n-type silicon and indium tin oxide. With the silicon device, by tuning the thicknesses of the layers used in a metal-oxide semiconductor geometry, the device we call the “plasMOSter” can support plasmonic modes as well as exactly one photonic mode. With an applied field, this photonic mode is pushed into cutoff and modulation depths of 11.2 dB are achieved. With the indium tin oxide device, the doping density within the material is changed and as a result, the plasma frequency is shifted into the near-infrared and visible wavelengths. Using spectroscopic ellipsometry, the

structure is characterized with and without an applied electric field, and measurements show that when an accumulation layer is formed within the structure, the index of refraction within that layer is significantly changed and as a result, will change the optical modes supported in such a structure.

Contents

List of Figures	xii
List of Tables	xv
List of Publications	xvi
1 Introduction	1
1.1 Materials and Light	1
1.2 Glass	1
1.3 Optical Properties of Materials	4
1.4 Metals	5
1.4.1 Dispersion and Surface Plasmons	6
1.4.2 Metal Insulator Metal Waveguides	7
1.5 Scope of this Thesis	8
1.5.1 Part I: Ferroelectric Slot Waveguides	9
1.5.2 Part II: Semiconductor Slot Waveguides	11
I Ferroelectric Slot Waveguides	12
2 Ferroelectrics	13
2.1 Introduction	13
2.2 Point Groups and Crystal Symmetry	13
2.2.1 Symmetry	13
2.2.2 Crystal Polarization	14
2.3 Landau-Ginsburg Theory of Ferroelectrics	16

2.4	Electro-optic Effects	17
2.5	Piezoresponse Force Microscopy	19
2.6	Ion Implantation Induced Layer Transfer	20
3	Ion-Implantation Induced Layer Transfer of Single Crystalline Barium Titanate	
	Thin Films	23
3.1	Introduction	23
3.2	Ferroelectric Materials	23
3.3	Experimental Work	25
3.4	Analysis of the Layer Transfer Process	25
	3.4.1 Hydrogen Behavior in Ba-Ti-O-H Phases	27
	3.4.2 Cavity Formation and Real Hydrogen Behavior	30
	3.4.3 Microstructure of Ion Damaged Barium Titanate	33
	3.4.4 Domain Characterization of the Transferred Ferroelectric Layer	35
3.5	Conclusion	37
4	Analysis of Competing Failure Mechanisms in Layer Transferred Thin Films	39
4.1	Introduction	39
4.2	Layer Transfer and Lithium Niobate	40
4.3	Geometry of the System and Stress State of the Film	40
4.4	Stability of Microcracks in the Film	42
4.5	Buckling, Delamination, and Failure of the Film	46
	4.5.1 Delamination of a Film with a Semi-Infinite Defect	46
	4.5.2 Buckling of the Film	47
	4.5.3 Propagation of the Delamination Front Induced by Film Buckling	48
	4.5.4 Failure of the Thin Film Induced by Bending	50
	4.5.5 Comparisons of the Various Length Scales of the Problem and Criterion for Film Failure	52
4.6	Discussion and Comparison with Experimental Results	54
	4.6.1 Effect of the Compressive/Tensile State of the Stress on the Stability of Cracks	55
	4.6.2 Effect of a High Compressive Stress on the Film	56
4.7	Conclusion	60

5	Silver Diffusion Bonding and Layer Transfer of Lithium Niobate to Silicon	62
5.1	Introduction	62
5.2	Wafer Bonding Limitations	62
5.3	Experimental Work	64
5.4	Analysis of Silver Diffusion Bonding	65
5.5	Conclusion	69
6	Tunable Color Filters Based on Metal-Insulator-Metal Resonators	71
6.1	Introduction	71
6.2	Color Filtering and Plasmonics	71
6.3	Metal-Insulator-Metal Color Filtering	72
6.3.1	Determining the Experimentally Observed Color	74
6.4	Results from Passive Silicon Nitride Color Filtering	74
6.5	Modeling Active Color Filters	77
6.5.1	Varying the Output Coupling Separation	77
6.5.2	Varying the Output Coupling Depth	80
6.6	Losses	82
6.7	Increasing Slit Transmission	83
6.8	High Density Color Filtering Design	85
6.9	Conclusion	86
II	Semiconductor Slot Waveguides	88
7	The plasMOS_{tor}: A Metal/Oxide/Si Field Effect Plasmonic Modulator	89
7.1	Introduction	89
7.2	CMOS and the Emergence of Plasmonics	89
7.3	Design and Fabrication of the plasMOS _{tor}	90
7.4	Switching Behavior	96
7.5	Time Response Analysis	102
7.6	Conclusion	103
8	Transparent Conducting Oxides for Active Plasmonics	105
8.1	Introduction	105

8.2	Carrier Modulation in Active Plasmonics	105
8.3	Fabrication and Characterization	107
8.4	Index Shifting in Indium Tin Oxide	109
8.5	Mode Modulation in Metal/ InTiO₃ /Metal Waveguides	110
8.6	Conclusion	112
9	Conclusions	114
III	Appendices	118
A	Dispersion Relations for Metal-Insulator-Metal Waveguides	119
A.1	The General Solution	121
A.2	Boundary Conditions	123
A.2.1	E_x and D_z are continuous:	124
A.2.2	E_y is continuous:	125
A.2.3	H_z , H_y , and B_z are continuous:	125
B	Tensor Representation of Crystals	127
B.1	Tensor Notation	127
B.2	Orientation Effects of Crystal Properties	130
C	Spectroscopic Ellipsometry	132
D	Lithium Niobate Optical Properties	135
	Bibliography	142

List of Figures

1.1	The Lycurgus Cup.	3
1.2	Surface Plasmons	8
1.3	The Metal-Insulator-Metal Waveguide	9
1.4	Metal-Insulator-Metal Generalized Schematic.	10
2.1	32 Crystal System Symmetries	14
2.2	ABO ₃ Perovskite Unit Cell	15
2.3	Landau Spontaneous Polarization	18
2.4	Piezoresponse Force Microscopy	19
2.5	Contact Angle Measurements	21
2.6	The Layer Transfer Process	22
3.1	Contact Angle Measurements	26
3.2	Equilibrium concentration of available species in implanted BaTiO ₃ as a function of temperature and pressure	28
3.3	Equilibrium concentrations in the Ba-Ti-O-H system during cavity formation	29
3.4	Cracking and blistering during layer transfer	31
3.5	Forward recoil electron spectroscopy of implanted BaTiO ₃	32
3.6	Raman spectroscopy of BaTiO ₃ before, during, and after layer transfer and post-bond annealing	33
3.7	TEM of layer transfered BaTiO ₃	34
3.8	AFM and PFM of bulk and layer transfered BaTiO ₃	35
3.9	AFM and PFM of BaTiO ₃ films using PLD and layer transfer	36
3.10	Hysteresis curves of PLD and layer transfered BaTiO ₃	37
4.1	Layer transfer geometry	41

4.2	Geometry of a perturbed crack propagating in a film	43
4.3	Debonding with and without buckling	48
4.4	Energy release rate of an interfacial crack	49
4.5	Crack evolution diagrams thick and thin transferred layers	51
4.6	Transverse cracks during layer transfer under no applied stress	55
4.7	Telephone-cord-like cracks in compressively stressed LiNbO_3	56
4.8	A buckled region of LiNbO_3	57
4.9	Crack evolution diagram for the experimentally tested LiNbO_3	59
5.1	TEM sample extraction in the FIB	65
5.2	TEM of Lithium Niobate Sample	66
5.3	Formation of the Silver Bond	67
5.4	Silver Grain Growth	68
5.5	Silver XRD before and after annealing	69
6.1	Lithium Niobate MIM Device Schematic	72
6.2	Lithium niobate membrane fabrication	73
6.3	Lithium niobate membranes before and after FIB	74
6.4	1964 CIE RGB Color Matching Functions	75
6.5	1964 CIE RGB Color Matching Functions	76
6.6	Silicon Nitride MIM Device Dispersion	76
6.7	Lithium Niobate Output Colors with Varying Slit Spacing	78
6.8	Power transmission through LiNbO_3 waveguides	79
6.9	Lithium Niobate MIM Dispersion Diagram	80
6.10	Mode Profiles within MIM Waveguides	81
6.11	Trapezoidal Slit Transmission with varying Dimensions	84
6.12	Trapezoid/Rectangle Hybrid Slit Transmission with varying Dimensions	85
6.13	Three-dimensional Implementation of MIM Color Filters	87
7.1	plasmistor Membrane Fabrication	91
7.2	XRD and Raman measurements of Silicon Membrane Strain	92
7.3	plasmistor Device Schematic	93
7.4	plasmistor Membrane Overview	94

7.5	plasMOS _{tor} Dispersion	95
7.6	plasMOS _{tor} Dispersion	96
7.7	plasMOS _{tor} FDTD Simulations at $\lambda = 1550$ nm	97
7.8	plasMOS _{tor} FDTD Simulations at $\lambda = 685$ nm	98
7.9	Capacitance-voltage and switching behavior of individual devices.	99
7.10	plasMOS _{tor} Switching	100
7.11	plasMOS _{tor} Circuit Analysis	104
8.1	Plasma Frequency as a Function of Carrier Density	107
8.2	MOS Structure Studied for InTiO ₃ Ellipsometry	108
8.3	Ellipsometry of InTiO ₃ Under Applied Field	109
8.4	Calculated Broadband Complex Index of InTiO ₃	110
8.5	Accumulation Layer Complex Index in InTiO ₃	111
8.6	Optical Modes in a Au/InTiO ₃ /SiO ₂ /Au Waveguide	112
9.1	Summary of Parameters Studied to Affect Color Filter Output Spectrum	115
9.2	Summary of Parameters Studied to Affect plasMOS _{tor} Output Spectrum	116
A.1	Coordinates for MIM Dispersion Calculations	119
B.1	Three-Dimensional Piezoresponse Plot for Barium Titanate	131
C.1	Schematic of Spectroscopic Ellipsometry	133
C.2	Ellipsometry of InTiO ₃	134

List of Tables

3.1	Possible equilibrium species in the Ba-Ti-O-(H)	28
7.1	5-layer Stack Used in plasMOSstor Modeling	96
8.1	Drude Model Parameters with Voltage	112

List of Publications

Portions of this thesis have been drawn from the following publications:

Tunable Color Filters Based on Metal-Insulator-Metal Resonators. K. Diest, J.A. Dionne, M. Spain, and H.A. Atwater, Nano Letters, **9**, 2579 July 2009

Competing failure mechanisms in thin films: application to layer transfer. L. Ponson, K. Diest, H.A. Atwater, G. Ravichandran, and K. Bhattacharya, Journal of Applied Physics, **105**, 073514 April 2009

PlasMOSStor: a metal-oxide-Si field effect plasmonic modulator. J.A. Dionne*, K. Diest*, L.A. Sweatlock, and H.A. Atwater, Nano Letters, **9**, 897 January 2009

Silver diffusion bonding and layer transfer of lithium niobate to silicon. K. Diest, M.J. Archer, J.A. Dionne, Y.B. Park, M.J. Czubakowski, and H.A. Atwater, Applied Physics Letters, **93**, 092906 September 2008

Single crystalline BaTiO₃ thin films synthesized using ion implantation induced layer transfer. Y.B. Park, K. Diest, and H.A. Atwater, Journal of Applied Physics **102**, 074112 October 2007

Growth and optical property characterization of textured barium titanate thin films for photonic applications. M.J. Dicken, K. Diest, Y.B. Park, and H.A. Atwater, Journal of Crystal Growth **300**, 330 March 2007

The effect of biaxial texture on the effective electromechanical constants of polycrystalline barium

titanate and lead titanate thin films. J.L. Ruglovsy, J. Li, K. Diest, K. Bhattacharya, and H.A. Atwater, *Acta Materialia* **54**, 3657 May 2006

Chapter 1

Introduction

1.1 Materials and Light

Light, earth (materials), and their interaction; these topics have been studied for thousands of years. The materials that make up our world truly are the “Substance of Civilization” [104]. In many ways, the history of our world has been defined by the materials we have had at our disposal. Many of the periods in human history have been characterized by the materials that were available: the stone age, the bronze age, the iron age, the industrial revolution (which came about in no small part from the development of manufactured steel), and the silicon age. Many periods of human advancement can be attributed to materials development for military and scientific applications. In addition, civilizations that had not developed militarily, historically fell victim to civilizations that had. As Tadahiro Sekimoto, former president of Nippon Electric Corporation, said:

“Those who dominate materials, dominate technology.”

This holds true for the future as well as the past. Recent research on plasmonics has demonstrated negative refraction at visible frequencies [66]. This advancement could lead to optical superlenses which may rival the best microscopes in existence today, as well as the possibility of “cloaking” objects from an outside observer [92]. Finally, work by Roddenberry et al. has looked at using dilithium crystals to travel faster than the speed of light [7]. Until that time comes, we must focus on materials currently available to us, and by far, the most prevalent optical material is glass.

1.2 Glass

In its most basic form, glass is a combination of silicon (the 2nd most abundant material in the earth’s crust) with oxygen (the most abundant material in the earth’s crust). This simple combination is a key component in windows, computer chips, fiber optic cable, the sand at the beach,

optical telescopes, and a vast number of other applications. A metastable material, glass is basically a supercooled liquid frozen in place at room temperature. The fact that it's flowing, just extremely slowly, is evident from looking at the wavy windows in an old house or church that are actually thicker at the bottom than the top.

The first use of glass was not for optical purposes; rather, obsidian (volcanic glass which cools as it reaches the earth's surface) was cleaved into pieces and used as weapons and tools in the 7th millennium B.C.E. The first evidence of glass making was around 3000 B.C.E. in an area called the Canaanite-Phoenician coast near the Mediterranean (just north of present-day Haifa). The sand from this region contained the right concentrations of lime and silica, so that the traders of this region needed only to mix in natron (a mix of soda ash, baking soda, salt, and sodium sulfate) while the melt was placed into a hot fire [104].¹

The earliest glasses developed in this manner were opaque rather than transparent due to scattering from small air bubbles or particles trapped within the glass during formation. Later, during the 1st millennium B.C.E., hotter kilns were developed and artisans began to introduce metal oxides into the glass to control the color. By forming the glass either with or without charcoal present, the glassworkers were able to either reduce or oxidize the copper, respectively, and as a result, produce glass that was either red or blue, respectively.

One of the most famous examples of metal being introduced into glass is the Lycurgus Cup. This glass was produced during the 4th century A.D. during the Roman Empire (Figure 1.1). The cup depicts the death of King Lycurgus in Thrace at the hands of Dionysus. As can be seen from Figure 1.1, the glass appears red (a) when seen with light transmitted through the cup, and green (b) when seen with light reflected off the surface of the cup. This remarkable behavior results from the introduction of colloidal gold and silver into the glass during formation. The resulting gold-silver nanoparticles within the glass reflect the green portion of the visible spectrum while transmitting the red portion of the visible spectrum. A theory for this type of scattering from metal spheres would not be formalized until 1908 by Gustav Mie [72], \simeq 2200 years after the cup was made.

It was not until the 13th century that people began developing glass for scientific purposes and the idea of using glass to focus light became a reality. In the 1200s, the Italians invented eyeglasses

¹Interestingly enough, around 1400 - 1300 B.C.E. the Phoenicians and Aramaeans of this trade route needed a method for recording all the financial information from their trades and as a result, developed the alphabetic language [104].

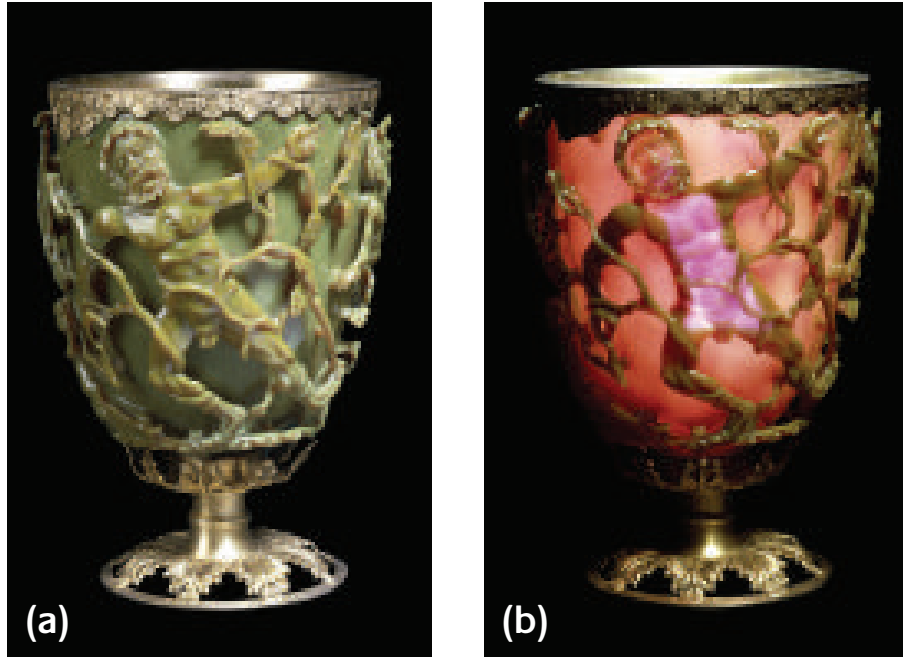


Figure 1.1. The Lycurgus cup shown in both reflection (a) and transmission (b). Gold-silver nanoparticles are responsible for the strong reflection of green light and transmission of red light [1].

which focused the direct and scattered light from objects whose sizes normally spanned millimeters to kilometers. At the end of the 16th century, Hans Lippershey and Zacharias Janssen produced two inventions that have changed the world. One, which was also developed by Jacob Metius, was the refracting telescope. A year later, an improved version was used by Galileo Galilei to focus light from the stars whose sizes spanned kilometers to billions of light years. Around the same time, with the help of Sacharias Jansen (Zacharias' dad), these men invented the microscope. Since then, this tool and its successors have focused light from millimeters down to nanometers.

Scientists have since been “focused” on exploring and manipulating nature on a smaller and smaller scale. Unfortunately, in the field of optics, this trend of ever smaller optics eventually reached a fundamental limit, diffraction. When the smallest dimension of an optical system, such as a waveguide, reaches $\frac{\lambda}{2n}$ where λ is the wavelength of the light and n is the refractive index of the waveguiding material, the device is diffraction limited. Below this limit, the waveguide will no longer be guided through the optical system. One method of getting around this diffraction limit that has evolved over the past 100 years, but has only taken off in the past 10, has been the field of plasmonics.

Plasmons have been studied since the beginning of the 20th century. Sommerfeld and Zenneck

studied the effects of radio waves propagation along the surfaces of conductors in 1899 and 1907, respectively [106, 128]. As mentioned above, Gustav Mie published work on scattering from metal spheres in 1908 [72]. In 1957, Ritchie studied electrons at the surface of metallic films using electron energy loss spectroscopy [99], and in 1968, Ritchie published work on optical interactions with metallic gratings [100]. In the 1960's, methods for prism coupling free-space light into surface plasmons was reported by Otto [82] as well as Kretschmann and Raether [60]. Since then, there have been thousands of papers published in the field of surface plasmons including the paper by Ebbesen et al. in 1998 which described enhanced optical transmission through sub-wavelength arrays [39]. This discovery was followed by the emerging field of “plasmonics” which is focused on developing device applications that utilize plasmonic effects.

1.3 Optical Properties of Materials

Any rigorous discussion of the interaction between light and materials begins with Maxwell's equations. In the absence of space charge and currents, we have:

$$\nabla \cdot \vec{E} = 0 \tag{1.1a}$$

$$\nabla \cdot \vec{B} = 0 \tag{1.1b}$$

$$\nabla \times \vec{E} = -\frac{1}{c} \frac{\partial \vec{B}}{\partial t} \tag{1.1c}$$

$$\nabla \times \vec{B} = \frac{1}{c} \epsilon_i(\omega) \frac{\partial \vec{E}}{\partial t} \tag{1.1d}$$

In addition, we have the following constitutive relations for linear, non-magnetic materials:

$$\vec{D} = \epsilon_0 \epsilon \vec{E} \tag{1.2a}$$

$$\vec{B} = \mu_0 \mu \vec{H} \tag{1.2b}$$

$$\vec{P} = \epsilon_0 \chi \vec{E} \tag{1.2c}$$

where Equation 1.2a relates the dielectric displacement, \vec{D} , to the electric field, \vec{E} , through the dielectric constant, ϵ ; Equation 1.2b relates the magnetic induction, \vec{B} , to the magnetic field, \vec{H} , through the permeability, μ ; and Equation 1.2c relates the polarization, \vec{P} , to the electric field, \vec{E} , through the dielectric susceptibility, χ . In these equations, $\epsilon = \epsilon_1 + i\epsilon_2$ represents the complex

dielectric function of a material. While this representation of the material's optical constants is more explicitly used with Maxwell's equations, an equivalent form of this property is given by the complex index of refraction: $\tilde{n} = n + i\kappa$. Here, n is the ratio of the speed of light in vacuum to the speed of light in the material, and κ is the extinction coefficient of light within the material. This representation is more directly related to the experimental observation of light interacting with matter. Depending on the situation, the two equivalent forms will be used in this thesis, and related by:

$$\epsilon_1 = n^2 - \kappa^2 \quad (1.3a)$$

$$\epsilon_2 = 2n\kappa \quad (1.3b)$$

$$n = \sqrt{\frac{\epsilon_1}{2} + \frac{1}{2}\sqrt{\epsilon_1^2 + \epsilon_2^2}} \quad (1.3c)$$

$$\kappa = \frac{\epsilon_2}{2n} \quad (1.3d)$$

and κ is related to the absorption coefficient “ α ” of light propagating through a material by: $\alpha = \frac{2\kappa\omega}{c}$.

1.4 Metals

Traditionally, when materials are considered to design optical waveguides, metals are not the first thing that come to mind. Metals can be thought of as a sea of free electrons oscillating around a lattice of fixed ion cores. These electrons are free to move throughout the metal and respond when the metal experiences an applied external field. When exposed to an optical field at microwave and far-infrared frequencies, many metals behave like a perfect electrical conductor. The electrons are able to respond to the external stimulus with the same frequency as the applied field. This gives rise to the high reflectivities and negligible electromagnetic field penetration traditionally associated with metals. As the frequency of the field increases, so does the response of the electrons. For noble metals like gold, silver, and copper, this process continues up to visible frequencies. In this regime, metals reach a point of maximum oscillation where the driving field strongly couples into the longitudinal oscillations of the bulk electrons within the metal. This is known as the plasma frequency of the metal:

$$\omega_p = \sqrt{\frac{4\pi n e^2}{m^*}} \quad (1.4)$$

where “n” is the density of electrons within the metal and “m*” is the effective mass of the electrons. Above this frequency, the metal behaves as a dielectric and experiences significant electromagnetic field penetration into the metal.

Separate from these “bulk plasmons” are a type of electron wave within metals known as a surface plasmon polaritons (SPPs). A SPP is a collective electron density oscillation at the interface between a metal and a dielectric; these SPPs will be the focus of this thesis. Hereafter, when the phrase “plasmon” is used, surface plasmon polaritons will be the intended meaning.

1.4.1 Dispersion and Surface Plasmons

Even though ϵ and \tilde{n} are referred to as constants, in many situations, these properties can vary significantly depending on the configurations in which they are used as well as the frequency of the light involved. This property of materials is known as dispersion.

To calculate the dispersion of these structures, we start with an incident electromagnetic wave of the form:

$$\vec{E}(x, y, z) \sim E_0 e^{i(k_x x - k_z |z| - \omega t)} \quad (1.5)$$

whose electric field has a perpendicular component to the waveguide (transverse-magnetic polarization). Here the components of the electric field within the metal are given by:

$$E_x^{metal} = E_0 e^{i(k_x x - k_{z1} |z| - \omega t)} \quad (1.6a)$$

$$E_y^{metal} = 0 \quad (1.6b)$$

$$E_z^{metal} = E_0 \left(\frac{-k_x}{k_{z1}} \right) e^{i(k_x x - k_{z1} |z| - \omega t)} \quad (1.6c)$$

and the components of the electric field within the dielectric are given by:

$$E_x^{dielectric} = E_0 e^{i(k_x x - k_{z2} |z| - \omega t)} \quad (1.7a)$$

$$E_y^{dielectric} = 0 \quad (1.7b)$$

$$E_z^{dielectric} = E_0 \left(\frac{-\epsilon_1 k_x}{\epsilon_2 k_{z1}} \right) e^{i(k_x x - k_{z2} |z| - \omega t)} \quad (1.7c)$$

where k_{z1} and ϵ_1 represent the wave vector and dielectric constant within the metal layer and k_{z2}

and ϵ_2 represent the wavevector and dielectric constant within the dielectric layer. For both sets of equations, k_x represents the component of the wave vector in the direction of propagation along the metal-dielectric interface. Similarly, k_z represents the component of the wave vector perpendicular to the metal-dielectric interface and from this, we obtain the decay length of the electro-magnetic field into the layers:

$$\hat{z} = \frac{1}{|k_z|} \quad (1.8)$$

By requiring continuity of the \vec{E} and \vec{B} fields at the interface between the two layers, we obtain the dispersion relation for a single metal-dielectric interface [71, 108]:

$$k_x = \frac{\omega}{c} n_{spp} \quad (1.9a)$$

$$k_{z1,2}^2 = \epsilon_{1,2} \left(\frac{\omega}{c} \right)^2 - k_x^2 \quad (1.9b)$$

where the effective surface plasmon index is given by:

$$n_{spp} = \sqrt{\frac{\epsilon_1 \epsilon_2}{\epsilon_1 + \epsilon_2}} \quad (1.10)$$

1.4.2 Metal Insulator Metal Waveguides

One of the benefits of coupling light from free space into surface plasmons, is that you can significantly reduce the wavelength of the light. Taking this design one step further, by placing a second metal layer above the dielectric layer as well as below, one can fabricate a metal-insulator-metal (MIM) waveguide. These structures allow extremely high modal confinement of light.

Dispersion calculations for the MIM geometry are reported in Appendix A and the results are reported here. For transverse-magnetic polarized light, the dispersion relations for MIM waveguides are given by:

$$\epsilon_2 k_{z1} + \epsilon_1 k_{z2} \left\{ \begin{array}{l} \coth(k_{z1}d/2) \\ \tanh(k_{z1}d/2) \end{array} \right\} = 0 \quad (1.11)$$

where d represents the thickness of the dielectric layer. A schematic of such a structure and a representative plot of the dispersion relation is shown in Figure 1.3. Seen in the dispersion diagram are the different plasmonic and photonic modes that would be supported within this structure over the visible spectrum as a function of the real part of k_x . As a reference, the light line for this structure is plotted as the dotted line, and the surface plasmon and bulk plasma frequencies are

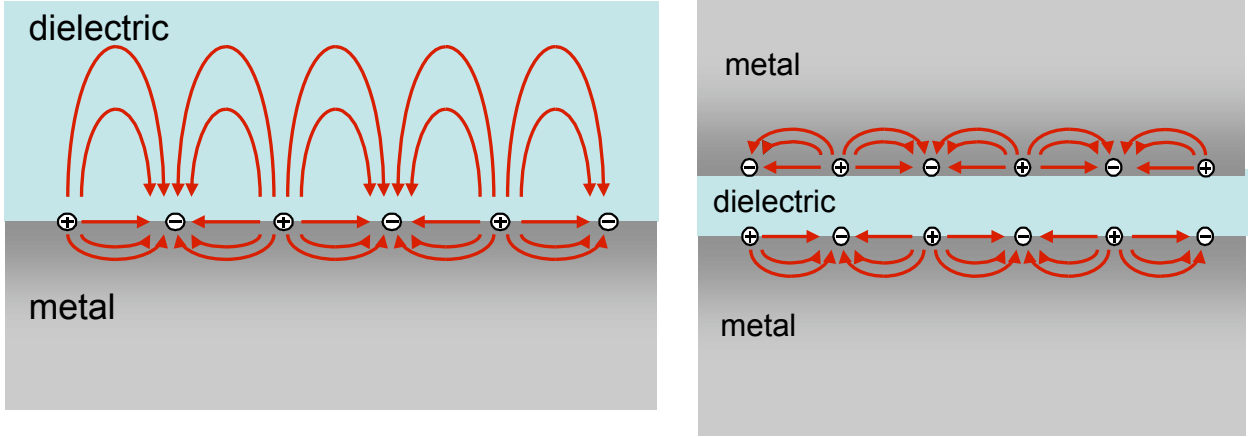


Figure 1.2. The figure on the left shows the electric field lines of a surface plasmon at a metal-dielectric interface. The figure on the right shows the same schematic for a metal-insulator-metal waveguide.

also labeled. This plot shows the existence of the plasmonic mode as well as one photonic mode within the structure. Here the plasmonic mode lies to the right of the light line because of the fact that this mode has a higher momentum than a free-space wave that would couple into it. In contrast, the photonic mode, whose momentum is strictly less than a free-space wave to which it would couple, lies to the left of the light line.

The phase and group velocities for these optical modes are defined by:

$$v_p = \frac{\omega}{k} \tag{1.12a}$$

$$v_g = \frac{\partial\omega}{\partial k} \tag{1.12b}$$

We can see that near the plasmon resonance in Figure 1.3, $v_g \rightarrow 0$, and this “slow wave” is characteristic of surface plasmons.

1.5 Scope of this Thesis

As the title suggests, the scope of this thesis is the design and fabrication of active MIM waveguides that support plasmonic and photonic modes. The idea is that by replacing the insulator layer with an active material and applying an electric field across the device, the output of the devices can be

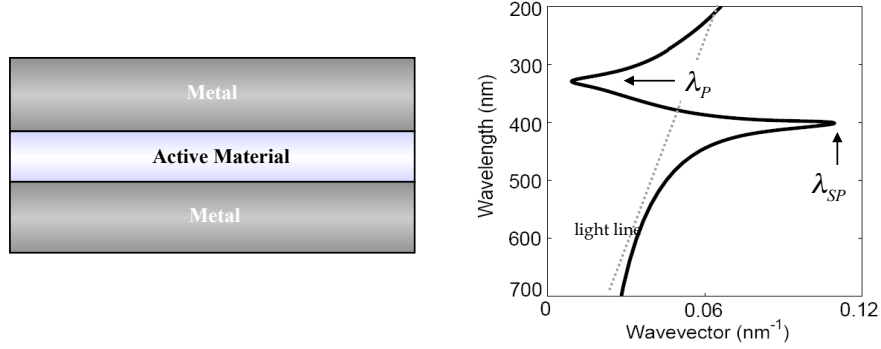


Figure 1.3. The figure on the left shows a generalized schematic of the semi-infinite metal-insulator-metal waveguide. The plot on the right shows a typical dispersion diagram for this type of structure. Both the plasma and surface plasmon resonances can be tuned over a wide range of the electromagnetic spectrum by changing the dimensions of and materials that make up the layers within the waveguide.

tuned across the visible and infrared portions of the electromagnetic spectrum.

By changing each of the materials in the three layer stack (Figure 1.4), as well as their relative thicknesses, the dispersion properties of the device as well as the resonance and filtering properties can be tuned over a wide range of the electromagnetic spectrum. In addition, by changing the dimensions of the in-coupling and out-coupling structures, as well as the distance between them, we can selectively access a large range of the different waveguide mode profiles that are present within the structure.

To this end, there are two main sections of the thesis. Each focuses on active MIM waveguides that utilize a different physical mechanism to induce a change in the region that supports the various optical modes. The first section looks at the utilizing electro-optic effect in lithium niobate to create tunable color filters, and the second section looks at modulating the carrier density distribution across the structure in n-type silicon and indium tin oxide to change the mode profiles within the waveguide.

1.5.1 Part I: Ferroelectric Slot Waveguides

Part I of this thesis deals with using ferroelectric materials as the active layer between the two metal cladding layers of the waveguide. The idea is to take advantage of the electro-optic effect in ferroelectric materials and change the index of refraction within the waveguide under an ap-

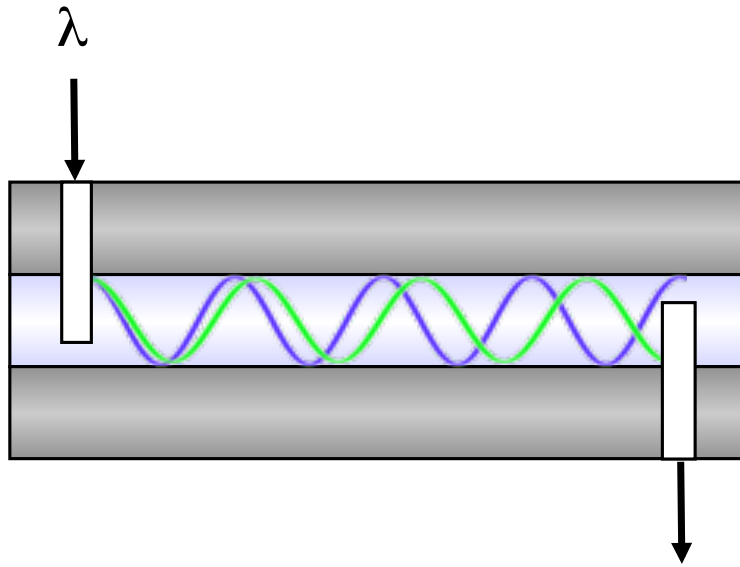


Figure 1.4. The schematic on the right shows a typical device that was fabricated using the basic metal-insulator-metal geometry.

plied electric field. In addition, all the ferroelectric layers used in this thesis were single crystal and obtained using ion-implantation induced layer transfer. This process has many benefits over conventional thin-film growth techniques and will be discussed in detail in Chapters 2, 3, and 4.

Chapter 2 is an overview of ferroelectric materials and the specific materials properties that enable them to perform the electro-optic switching discussed above. The chapter finishes with an overview of ion implantation induced layer transfer which is the method by which the thin film, single crystal ferroelectric layer are produced in this thesis. In Chapter 3, the ion-implantation induced layer transfer process is analyzed from a thermodynamic standpoint and the ion-implantation conditions required for layer transfer are determined. Assuming the sample has been properly ion-implanted, Chapter 4 analyzes the possible failure mechanisms that can occur in the layer transferred thin-film from the standpoint of thermal expansion-induced stress. The chapter then goes on to determine the necessary requirements for thin-film and substrate to ensure a coherent layer is transferred. This analysis is then done for the case of lithium niobate transferred onto a silicon substrate.

One of the largest difficulties in successful layer transfer is producing a strong, robust bond between the two materials in question. In Chapter 5, a new technique for metal bonding is introduced and analyzed. This process involves evaporating a layer of silver on both surfaces before

the layer transfer process, and during the course of the bonding/layer transfer step, Chapter 5 shows that diffusion bonding causes the two silver layers to become one, continuous layer. The last chapter in Part I, Chapter 6, looks at passive and active MIM waveguides with silicon nitride and lithium niobate in the optical channel. These devices are shown to naturally filter white light into individual colors based on the interference of the different optical modes within the dielectric layer. Full-field electromagnetic simulations show that these devices can preferentially couple to any of the primary colors and can tune the output color of the device with an applied field.

1.5.2 Part II: Semiconductor Slot Waveguides

Part II of this thesis deals with using two semiconductor materials (n-type silicon and indium tin oxide) as the active layer between the two metal cladding layers of the waveguide. Here the idea is to apply an electric field across the semiconductor layers and modulate the carrier distribution within the waveguide.

Chapter 7 examines a new type of plasmonic/photonic waveguide whose thickness is carefully chosen to support one plasmonic mode and exactly one photonic mode very close to cut-off. Through an extensive experimental analysis and full-field electromagnetic simulations, the device is shown to behave like an MOS capacitor and with an applied field, push the photonic mode into cutoff.

Chapter 8 looks at changing the doping density within transparent conducting oxides (like indium tin oxide) to shift the plasma frequency into the near-infrared and visible wavelengths. The material is incorporated into an MOS structure similar to that in Chapter 7 and through extensive characterization using spectroscopic ellipsometry (Appendix C), the thin film stack is characterized with and without an applied electric field. The measurements show that when an accumulation layer is formed within the structure, the index of refraction within that layer is significantly changed and as a result, will change the optical modes supported in such a structure.

Part I

Ferroelectric Slot Waveguides

Chapter 2

Ferroelectrics

2.1 Introduction

The first part of this thesis is focused on producing an active MIM waveguide with a ferroelectric layer as the active material. Henceforth, the analysis of ferroelectrics will be done with two materials which accurately represent the field, barium titanate (BaTiO_3) and lithium niobate (LiNbO_3). In this chapter, we will introduce ferroelectrics and motivate why these materials present a unique opportunity for use in active plasmonic devices. These materials exhibit a wide range of properties including piezoelectricity, ferroelectricity, pyroelectricity, and electro-optic effects. The intensity of these effects within the materials is directly related to the quality of the crystal in question. As a result, ion implantation induced layer transfer is introduced at the conclusion of this chapter as a method of producing single crystal thin film ferroelectrics.

2.2 Point Groups and Crystal Symmetry

2.2.1 Symmetry

All crystalline materials can be represented by a crystal lattice and a basis. The lattice represents the three-dimensional periodic array of points in space. These points form individual “unit cells” which represent the smallest repeat unit of the lattice. The basis represents the atom or atoms which lie on each point within the lattice. These crystals can be organized by their symmetry operations and divided into 32 distinct “point groups”. Of these 32 groups, 11 have a well defined center of symmetry and are defined as centrosymmetric. Out of the remaining 21 groups, 20 are piezoelectric [the (432) point group being the only exception]. Out of the 20 piezoelectric point groups, 10 have a unique polar axis and are referred to as ferroelectric. Below a critical transition temperature, the Curie temperature (T_c), ferroelectric materials exhibit a spontaneous polarization due to a distortion in the crystal structure. A diagram of the different crystal systems is shown in

Figure 2.1, and the piezoelectric point groups are shown in the boxed, grey region.

Polarity	Symmetry	Crystal system										
		Cubic		Hexagonal		Tetragonal		Rhombic		Orthorhombic	Monoclinic	Tridinic
Non-polar (22)	Centro (11)	$m\bar{3}m$	$m\bar{3}$	$6/mmm$	$6/m$	$4/mmm$	$4/m$	$\bar{3}m$	$\bar{3}$	mmm	$2/m$	
	Non-centro (21)	432	23	622	$\bar{6}$	422	$\bar{4}$	32		222		
Polar (Piezo-electric) (10)		$43m$	$\bar{6}m2$	$6mm$	6	$4mm$	4	$3m$	3	$mm2$	$2m$	1

Figure 2.1. Shown here are the 32 crystal point groups. The piezoelectric groups are shown in the boxed, grey region.

2.2.2 Crystal Polarization

The two ferroelectrics that will be studied throughout this thesis are barium titanate (BaTiO_3) and lithium niobate (LiNbO_3). BaTiO_3 is one of the most well studied and widely used ferroelectrics. It belongs to a category of materials called ABO_3 perovskites. Above T_c , these materials have a cubic unit cell and below T_c , they have a tetragonal unit cell, Figure 2.2. In the cubic state, the A atom resides in the center of the unit cell, the B atoms reside on the 8 corners, and the oxygen atoms lie in the 6 face-centered positions. From a physical standpoint, when cubic BaTiO_3 is cooled below T_c , there is a contraction along the \bar{a} -axis and a corresponding elongation along the \bar{c} -axis. As a result, above T_c , the Ba atom sits in the center of the cubic unit cell and is surrounded by the 4 oxygen atoms in the central plane of the unit cell. Upon cooling below T_c , the contraction in the \bar{a} -axis results in the oxygen atoms moving towards the center of the unit cell, and this forces the Ba atom to move either above or below the central plane of oxygen atoms, Figure 2.2. This produces the spontaneous polarization that is associated with ferroelectrics. When the crystal is subjected to an external pressure, the crystal structure will realign to relieve this force and as a

result, generate a net electric field. This is the *direct piezoelectric effect*. The converse of this is also true. Under an applied electric field, the unit cell dipoles will realign themselves with the field and change the crystal dimensions. This is known as the *converse piezoelectric effect*.

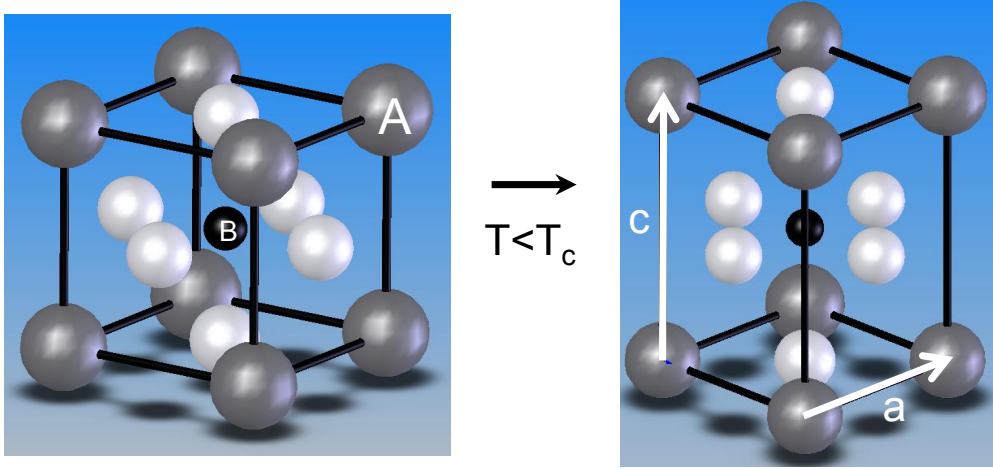


Figure 2.2. The ABO_3 perovskite unit cell is shown above (left) and below (right) the Curie temperature. The A atom is shown in the center, the B atoms are shown on 8 corner sites, and the oxygen atoms are shown on the face-centered sites.

From an energetics standpoint, Uchino gives the energy of the spontaneous dipole for N atoms per unit volume as [116]:

$$E_{dipole} = -\frac{N\alpha\gamma^2}{9\epsilon_0^2}\vec{\mathcal{P}}^2 \quad (2.1)$$

where α is the ionic polarizability of the ion, γ is the Lorentz factor, ϵ_0 is permittivity of vacuum, and \mathcal{P} is the surrounding polarization. In addition, the elastic energy associated with ion displacement from its equilibrium position, \vec{u} , is given by:

$$E_{elastic} = N \left[\left(\frac{k}{2} \right) \vec{u}^2 + \left(\frac{k'}{2} \right) \vec{u}^4 \right] \quad (2.2)$$

where k and k' represent the two spring constants associated with the energy between ions within a unit cell and between different unit cells, respectively. By assuming $\mathcal{P} = Nq\vec{u}$, where q is electric charge, we arrive at:

$$E_{total} = E_{dipole} + E_{elastic} = \left[\left(\frac{k}{2Nq^2} \right) - \left(\frac{N\alpha\gamma^2}{9\epsilon_0^2} \right) \right] \vec{\mathcal{P}}^2 + \left[\frac{k'}{4N^3q^4} \right] \vec{\mathcal{P}}^4 \quad (2.3)$$

This says that if the elastic energy within the crystal is greater than the dipole-dipole interactions, then there is no spontaneous polarization, $T > T_c$. If the converse is true, then there will be a spontaneous polarization, $T < T_c$.

2.3 Landau-Ginsburg Theory of Ferroelectrics

One analytic method of formalizing the second-order phase transition that occurs upon cooling a ferroelectric below its Curie temperature is to use the Landau Theory of phase transitions. This theory, which was developed by the Nobel Prize winning physicist Lev Landau, represents the free energy of a crystal as a phenomenological expression based on the order parameter, Ψ , of the total polarization. The generalized expression for the Landau free energy of the system, \mathcal{F} , is given by [112]:

$$\mathcal{F} = \mathcal{F}_0 + \frac{1}{2}\alpha\Psi^2 + \frac{1}{4}\beta\Psi^4 + \frac{1}{2}\delta\left(\vec{\nabla}\Psi\right)^2 - \vec{E}\Psi \quad (2.4)$$

Here, α and β are temperature dependent coefficients, and δ represents a restoring force which limits the minimum size of ferroelectric domains. This representation, which neglects terms higher than fourth order, and includes a term for polarization gradients, $\frac{1}{2}\delta\left(\vec{\nabla}\Psi\right)^2$, as well as an applied electric field, $-\vec{E}\Psi$. Due to the fact that the energy must be invariant under polarization reversal, the coefficients of all the odd powers of Ψ are zero.

For the case of ferroelectrics, the order parameter, Ψ , represents the polarization, \mathcal{P} , of the unit cell. Landau theory assumes that below the critical temperature, T_c , a spontaneous polarization will occur and that the components of \mathcal{P} vary continuously across T_c . For the case of BaTiO₃, the change from a cubic to tetragonal unit cell will result in a spontaneous polarization and can be written as [56]:

$$\begin{aligned} \mathcal{F} = \mathcal{F}_0 + \frac{1}{2}\left(\alpha_z\mathcal{P}_z^2 + [\mathcal{P}_x^2 + \mathcal{P}_y^2]\right) \alpha_{xy} \\ + \frac{1}{4}\left(\beta_1\mathcal{P}_z^4 + \beta_2[\mathcal{P}_x^2 + \mathcal{P}_y^2]^2 + \beta_3[\mathcal{P}_x^2 - \mathcal{P}_y^2]^2 + \beta_4[\mathcal{P}_x^2\mathcal{P}_y^2] + \beta_5\mathcal{P}_z^2[\mathcal{P}_x^2 + \mathcal{P}_y^2]\right) \\ + \frac{1}{2}\delta\left(\vec{\nabla}\Psi\right)^2 - \vec{E}\Psi \end{aligned} \quad (2.5)$$

For simplicity, we will assume that the spontaneous polarization is in the $\pm\mathcal{P}_z$ direction. In this

case, the Landau free energy of the crystal is given by:

$$\mathcal{F} = \mathcal{F}_0 + \frac{1}{2}\alpha\mathcal{P}_z^2 + \frac{1}{4}\beta_1\mathcal{P}_z^4 \quad (2.6)$$

and the equilibrium polarization of the crystal below the critical temperature is found by:

$$\frac{\partial\mathcal{F}}{\partial\mathcal{P}} = 0 = \alpha\mathcal{P} + \beta\mathcal{P}^3 = \mathcal{P}(\alpha + \beta\mathcal{P}^2) \quad (2.7)$$

which has the solutions:

$$\mathcal{P}_0 = 0, \pm\sqrt{\frac{-\alpha}{\beta}} \quad (2.8)$$

Here we let $\alpha = \alpha_0(T - T_c)$ where $\alpha_0 = \frac{C}{\epsilon_0}$. This gives the final form of the spontaneous polarization as:

$$\mathcal{P}_0 = 0, \pm\sqrt{\frac{\alpha_0(T_c - T)}{\beta}} \quad (2.9)$$

From this we can see that above T_c , when the material is paraelectric, there are no real solutions for \mathcal{P} , and below T_c there are two minima which correspond to the two-fold degeneracy in \mathcal{P} . For the case of the tetragonal unit cell of BaTiO₃, this corresponds to the $\pm\mathcal{P}_z$ polarization. Also, for the fourth order expansion, we require that $\beta > 0$ to ensure real solutions to \mathcal{P} for $T < T_c$. We also note here that $\mathcal{P} \sim |T - T_c|^\beta$, and as a result, the critical exponent $\beta = \frac{1}{2}$.

A plot of this is shown in Figure 2.3. Here, $\pm\mathcal{P}_z$ can be seen below the x-axis and no spontaneous polarization can be seen in the curve representing $T > T_c$. Additionally, $\Delta = \alpha\Psi^2$ is shown below the x-axis which represents the energy penalty for wide domain walls within the ferroelectric.

Although it is beyond the scope of this thesis, at T_c this formalism for ferroelectrics can be used to analyze: the absence of any latent heat; a discontinuity in the specific heat; and a divergence in the susceptibility [112].

2.4 Electro-optic Effects

The response of any crystal to an external field will depend strongly on the frequency of that field. With visible light, the frequency is $\sim 430 - 750$ THz and as a result, only the electrons within a solid can respond. For electro-optic materials, the application of an external electric field will induce a displacement of the ion cores within the material. This results in a change in the electron density distribution throughout the material, and as a result, a change in the materials index of

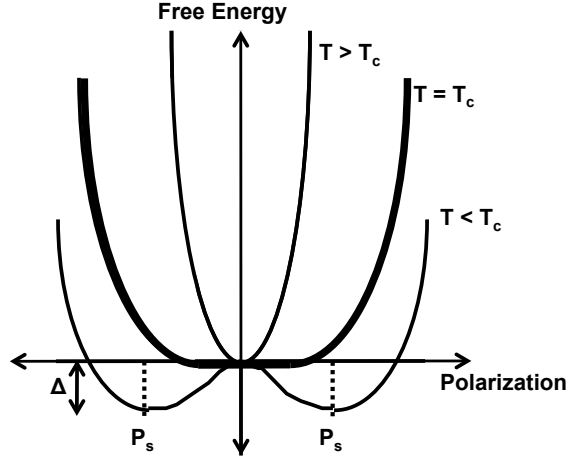


Figure 2.3. Landau Free Energy of the crystal as a function of polarization at three temperatures: $T > T_c$ which exhibits no spontaneous polarization, $T = T_c$, and $T < T_c$ which has a two-fold solution.

refraction. For the case of an electric field applied in the \hat{z} direction, the redistribution of the ions within the lattice would produce an elongation in the \hat{z} direction and a corresponding contraction in the \hat{x} and \hat{y} directions. As a result, the electron density (and index or refraction) would decrease in the \hat{z} direction and would increase in the \hat{x} and \hat{y} directions.

As discussed in Appendix B, we know that the index within a material is a second-rank tensor which is given by [116]:

$$\frac{1}{n_{ij}^2(E)} - \frac{1}{n_{ij}^2(0)} = \sum_k r_{ijk} E_k + \sum_{kl} R_{ijkl} E_k E_l \quad (2.10)$$

where $n_{ij}(E)$ and $n_{ij}(0)$ are the indices of refraction with and without an applied electric field, respectively. r_{ijk} is the Pockels coefficient which represents the linear electro-optic effect, and R_{ijkl} is the Kerr coefficient which represents the quadratic electro-optic effect.

As an example, the ABO_3 perovskites discussed in Section 2.2.2 (Figure 2.1) show that in their paraelectric phase, these materials belong to the $m3m$ symmetry group. As a result, the Kerr

coefficients for this crystal structure are given by [116]:

$$\begin{bmatrix} R_{11} & R_{12} & R_{12} & 0 & 0 & 0 \\ R_{12} & R_{11} & R_{12} & 0 & 0 & 0 \\ R_{12} & R_{12} & R_{11} & 0 & 0 & 0 \\ 0 & 0 & 0 & R_{44} & 0 & 0 \\ 0 & 0 & 0 & 0 & R_{44} & 0 \\ 0 & 0 & 0 & 0 & 0 & R_{44} \end{bmatrix} \quad (2.11)$$

2.5 Piezoresponse Force Microscopy

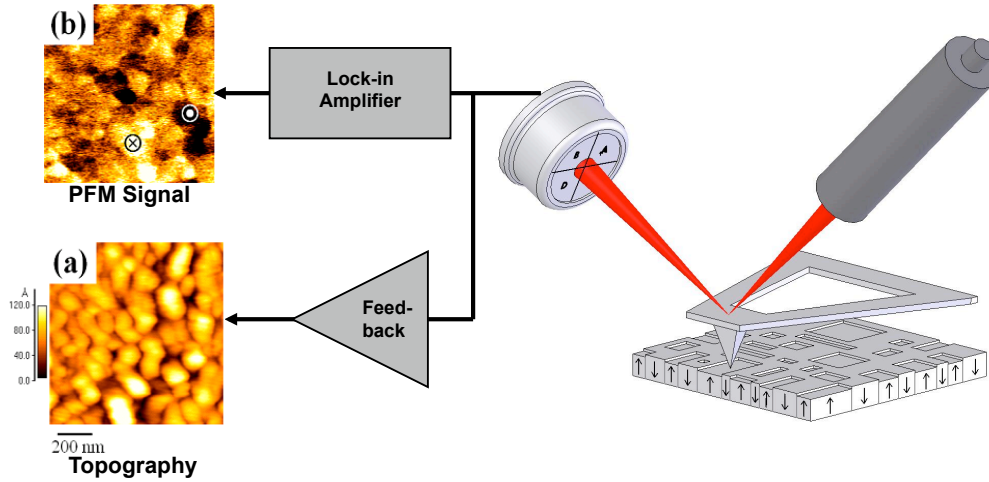


Figure 2.4. A schematic of a typical PFM setup is shown. Both topography (a) and piezoresponse (b) as a function of position on the sample are shown.

One method of investigating the behavior of piezoelectrics that will be utilized in Chapter 3 is Piezoresponse Force Microscopy (PFM). This technique utilizes a standard atomic force microscope (AFM) with a conductive scanning tip. The tip is rastered across the sample surface in a series of line scans which are compiled to produce a topological image of the surface of the sample. At the same time, a lock-in amplifier is used to apply a DC offset to the tip as well as an AC voltage (traditionally from 1 - 5 kHz). The applied electric fields cause the piezoelectric material to expand and contract with the AC voltage and this time-dependent response (whose frequency is that of the drive signal) is separated from the rest of the topological data using the same lock-in amplifier,

Figure 2.4. This is necessary because the piezoresponse signal from the sample is usually near the lower detection limit of the AFM and as a result, the topography will dominate the output signal. This is especially true with rough samples which might also have surface oscillation frequencies which are similar to those of the piezoresponse!

In general, the piezoresponse from the sample is given by:

$$\Delta z = -d^*V \quad (2.12)$$

where d^* is the piezoelectric coefficient of the material and is > 0 for positive domains, Δz is the change in height of the sample from the converse piezoelectric effect, and V is the applied voltage. Including the AC voltage gives:

$$V = V_{DC} + V_{AC}\sin(\omega t) \quad (2.13)$$

$$\Delta z = d_{33}^*V_{AC}\sin(\omega t + \Phi) \begin{cases} \Phi = \pi \text{ for } P_z > 0 \\ \Phi = 0 \text{ for } P_z < 0 \end{cases} \quad (2.14a)$$

where $P_z > 0$ indicates that there is a spontaneous positive polarization at the crystal/tip interface, ω is the drive frequency of the AC voltage, and d_{33}^* is the constrained out-of-plane piezoelectric coefficient. This value is less than d_{33} for an individual unit cell because of the fact that it is constrained by the film around it. The two constants are related by the compliance of the film “ s_{ij} ” and the shear components of the piezoresponse:

$$d_{33}^* = d_{33} - \frac{2d_{31}s_{12}}{s_{11} + s_{12}} \quad (2.15)$$

2.6 Ion Implantation Induced Layer Transfer

To fabricate single crystals of the ferroelectrics studied in this thesis, we utilize a technique known as ion implantation induced layer transfer (or layer transfer for short). The process consists of four main steps. The first, which will be discussed in Chapter 3, is ion implantation. This step consists of sending high energy H^+ ions into a single crystal of the material to be transferred. Often times, the material is also co-implanted with either He^+ or B^+ . The depth of implantation is determined by the energy of implantation and a gaussian distribution of the implanted depths is obtained. If

two ions are co-implanted, the energies of implantations should be tuned so that the peaks of the implantation distributions overlap, and these calculations are done using Stopping and Range of Ions in Matter (SRIM) software [6].

Upon implantation of the single crystal sample, the surfaces of both the implanted sample as well as the substrate to which it will be bonded are cleaned and “activated” using a plasma treatment process. The effectiveness of the plasma activation can be determined using contact angle measurements of the “as treated” surface with a microsyringe imaging system, Figure 2.5.

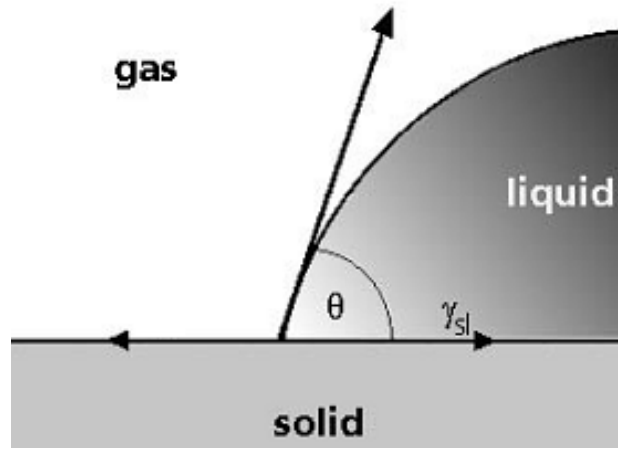
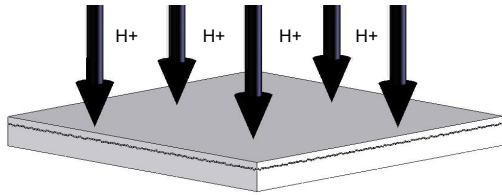


Figure 2.5. Typical solid-liquid-gas contact angle schematic used in determining the effectiveness of plasma treatment before wafer bonding.

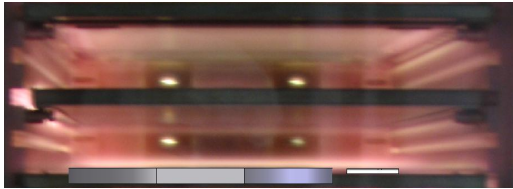
After surface treatment of the implanted sample and substrate are complete, the two surfaces are brought in contact under high temperature and pressure. At high temperature, the implanted species preferentially diffuse through the implanted crystal along the plane of implantation. This process induces the formation of gas voids. Provided the crystal is under an acceptable amount of compressive stress during this process (Chapter 4), the edges of these voids grow along the plane of implantation, join with other voids, and eventually cleave off a thin film single crystal layer of the implanted material. A schematic of this process is shown in Figure 2.6.

Optimizing each of the different steps in Figure 2.6 is non-trivial and Chapters 2, 3, and 4 will discuss research that was done to produce a coherent, layer transferred film. As difficult as this process is, there are significant benefits to using this method of fabrication over other

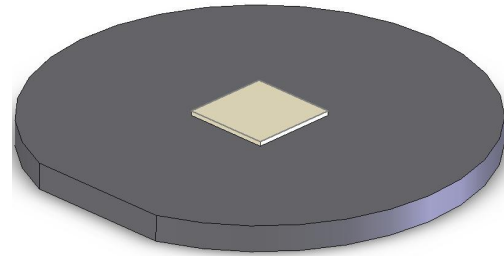
1. Hydrogen and (Helium or Boron) implantation to desired depth.



2. Planarization and plasma activation of the surfaces.



4. Wafer bonded heterostructure.



3. Bonding and layer splitting. Blistering occurs at implantation depth while a covalent bond is formed at the bonding interface.

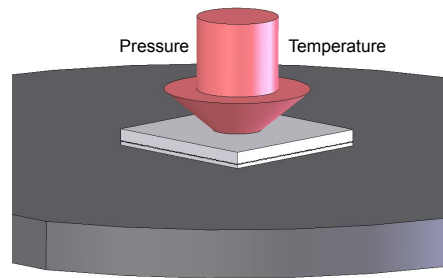


Figure 2.6. A schematic process flow of the layer transfer process.

techniques. Fabrication methods fall into two broad categories, bottom up and top down. Bottom up fabrication involves the deposition of successive layers. Using lithography and etching steps after each deposition, your structure is fabricated from the “bottom up”. This method is extremely flexible and allows the integration of a wide variety of materials. The drawback to this technique is that the films will either be amorphous or polycrystalline. On the other hand, top down processing uses various etch steps to drill into a substrate and fabricate your structure from the “top down”. Provided you start with a single crystal substrate, this method has the benefit of producing single crystal structures; however, this technique is not nearly as flexible in terms of integrating different materials and structures. Ideally, ion implantation induced layer transfer would combine the best of both worlds and produce single crystal thin films using a bottom approach.

Chapter 3

Ion-Implantation Induced Layer Transfer of Single Crystalline Barium Titanate Thin Films

3.1 Introduction

In this chapter, we examine the optimization of the ion implantation process by studying the layer transfer of barium titanate thin films onto silicon-based substrates. Hydrogen and helium ions were co-implanted to facilitate ion-implantation-induced layer transfer of films from barium titanate single crystals. From thermodynamic equilibrium calculations, we suggest that the dominant species during cavity nucleation and growth are H_2 , H^+ , H_2O , Ba^{2+} and Ba-OH , and that the addition of hydrogen to the Ba-Ti-O system can effectively suppress volatile oxide formation during layer transfer and subsequent annealing. After ion implantation, barium titanate layers contain microstructural defects and hydrogen precipitates in the lattice, but after layer transfer, the single crystal is found to be stoichiometric. Using direct wafer bonding and layer splitting, single crystal barium titanate thin films were transferred onto amorphous silicon nitride and Pt substrates. Micro-Raman spectroscopy indicated that the density of defects generated by ion implantation in barium titanate can be significantly reduced during post-transfer annealing, returning the transferred layer to its single crystal state. Characterization using piezoresponse force microscopy shows that the layer-transferred thin films are ferroelectric, with domain structures and piezoresponse characteristics similar to that of bulk crystals. ¹

3.2 Ferroelectric Materials

Ferroelectric materials have attracted increased attention as device materials in recent years because of their potential applications in microelectronics and integrated optics [105]. Furthermore, these

¹This chapter is based on work done with Dr. Young-Bae Park [87].

materials are attractive for microelectromechanical systems (MEMS) applications due to large displacement and high output force during actuation [93].

Many different methods have been studied to obtain high quality, thin film ferroelectric layers [125]. The growth of epitaxial thin films at relatively high temperatures ($> 700^{\circ}\text{C}$) has been reported using metal organic chemical vapor deposition, molecular beam epitaxy, atomic layer deposition, pulsed laser deposition, chemical solution deposition, and sol-gel processes. Integration of most of these technologies with conventional silicon-based device applications has proven difficult because of the high growth temperatures required and the need for an epitaxial template. Due to the complex set of elastic and electric boundary conditions at each grain, the grains in pressed ceramics and polycrystalline films are usually composed of multiple domains. If the spontaneous polarization within each domain is random, or distributed in such a way as to lead to zero net polarization, the pyroelectric and piezoelectric effects of individual domains will partially or significantly compensate each other. Additionally, for photonic devices, grain boundaries and domain boundaries can be sources of light scattering and absorption.

Recently, progress on integration of single crystal ferroelectrics has been made by fabrication of single crystal thin film layers. Light elements such as hydrogen and helium are implanted into a wafer at a specified projected range, and a film of equivalent thickness is exfoliated [22, 114]. Recently, successful layer transfer of semiconductors and ferroelectric materials has been reported [15, 54, 65, 74, 115, 127]. In the work reported here, layer transfer relies on direct wafer bonding and gas pressure-induced layer exfoliation. This is similar to that used to fabricate silicon-on-insulator structures, and enables much thinner films to be fabricated. We discuss hydrogen release and the resulting cavity growth mechanisms for the layer splitting of barium titanate (BaTiO_3), and the role of hydrogen during post-thermal annealing. Together with the thermodynamics and kinetics of cavity nucleation, growth, and blistering, these results provide an explanation of the layer exfoliation process. In this study, H^+ and He^+ were implanted in single crystal BaTiO_3 and subsequently bonded to silicon nitride $\text{Si}_3\text{N}_4/\text{Si}$ and Pt/Si receptor substrates, which are typical structures for ferroelectric memory and MEMS devices. Pt is typically used as a bottom electrode in ferroelectric capacitors and Si_3N_4 is typically used as an etch-stop layer in MEMS devices.

3.3 Experimental Work

Protons were implanted into single-crystal BaTiO₃ with energy between 20 and 80 keV with a dose of $5 \times 10^{16} - 1 \times 10^{17} \text{ cm}^{-2}$, followed by 30 - 115 keV He⁺ implantation with a dose of $1 \times 10^{17} \text{ cm}^{-2}$. All implantations were performed at room temperature. The donor and receptor substrates (sputtered Pt on Si and low-pressure chemical vapor deposition Si₃N₄ on Si) were cleaned with methanol, acetone, and deionized water. The donor and receptor substrates were brought in contact at room temperature. Heating during the initial bonding step causes micro-cracks to form and cavities to nucleate, coalesce, and blister in the implanted region. Isochronal annealing of the bonded donor material was performed between 300 and 500°C after initial bond formation, causing a layer whose thickness is equal to the implanted depth to be transferred to the receptor substrate.

The thermodynamic equilibrium composition at the annealing temperature (300 - 700°C) was calculated using the SOLGASMIX-PV code in Chemsage [5], minimizing the total Gibbs free energy of the system with data from the Joint-Army-Navy-Air Force (JANAF) thermochemical table [40]. Calculations were performed for both Ba-Ti-O and Ba-Ti-O-H systems with the compound conditions of 1:1:3 and 1:1:3:0.1-10, respectively, corresponding to stoichiometric single crystal BaTiO₃ with and without the addition of hydrogen.

Blistering was observed by polarized optical microscopy, scanning electron microscopy and atomic force microscopy. Atomic force microscopy was also used to characterize transferred film thickness and surface roughness. Micro-Raman spectroscopy, Rutherford backscattering spectroscopy, forward recoil elastic spectroscopy, energy dispersive x-ray spectroscopy, and transmission electron microscopy analyses were performed to assess the microstructural evaluation of the bulk crystal and transferred layer. Ferroelectric domain imaging and microscopic hysteresis loop measurements were obtained using piezoresponse force microscopy.

3.4 Analysis of the Layer Transfer Process

The key factors required to achieve covalent bonding between donor and receptor substrates are high surface flatness, low surface roughness, surface cleanliness, and chemical reactivity. Initial bonding of bulk, unimplanted BaTiO₃ crystals was successful since the donor and receptor substrates can be prepared according to these conditions. Bulk (100) BaTiO₃ has a typical lamellar domain pattern with tetragonal 90° a-axis and c-axis domains with sizes ranging from 5 to 400 nm, with a root-mean squared (RMS) roughness of 2.0 nm. Due to the alternating a-c tetragonal domain structure,

the surface of the BaTiO₃ sample is corrugated with a characteristic angle between domains given by: $\theta = 90^\circ - 2\arctan(a/c)$ where a and c refer to lattice constants of the [100] and [001] axes respectively. The peak-to-valley height of this surface corrugation was found to be in the range of 2 - 100 nm, depending on the domain size. The RMS roughness of the BaTiO₃ donor wafer slightly increased after ion implantation to 2.4 nm. Using a Monte Carlo simulation method for calculation of ion implantation and collision cascade characteristics [6], the ion projected range was determined to be ~ 430 nm [6]. The Pt coating thickness was 180 nm and the Si₃N₄ thickness was 50 nm, yielding a receptor substrate RMS roughness of 0.7 nm for Si₃N₄ coated Si substrates and 3.6 nm for Pt coated Si substrates. After room temperature bonding, no interference fringes were observed, indicating a distinct lack of surface particles or other contamination.

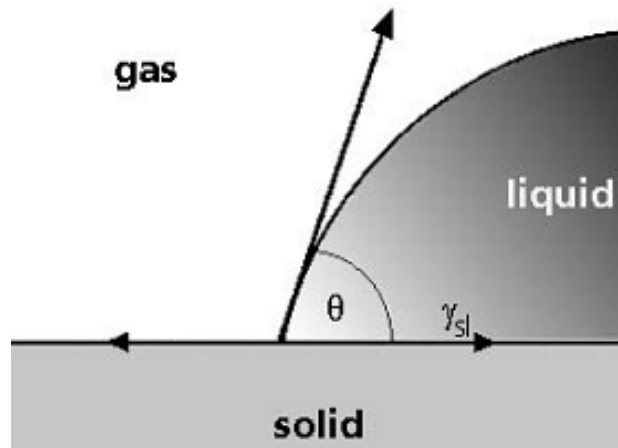


Figure 3.1. Typical solid-liquid-gas contact angle schematic.

The surface energy of the BaTiO₃ single crystals surfaces following H⁺ implantation was obtained by contact angle measurements using water and di-iodomethane droplets with a constant volume droplet of 20 dm³ using a double laser-beam goniometer. At room temperature, the surface energy is 61.1 mJ/m² and for the temperature-dependent surface energy, we used the phenomenological equation, $\gamma(T) = 6.11 \times 10^{-2} + 3.82 \times 10^{-5}T$ assuming $\gamma(T) = \gamma_0(1 + T/T_0)$, where T_0 is the critical temperature at which the solid-gas interface vanishes [46].

3.4.1 Hydrogen Behavior in Ba-Ti-O-H Phases

After ion implantation, the bulk BaTiO₃ lattice is filled with hydrogen. This hydrogen passivates the dangling bonds and defects generated by atomic displacements. In order to describe the behavior of hydrogen in solid materials, Sieverts law can be applied. Here: $c_0 = sp_e^{1/2}$ where pressure, p_e , is related to fugacity, f_e , and the hydrogen concentration, c_0 , in the solid at equilibrium [81]. The depth profile of implanted hydrogen is determined by post-implantation diffusion as well as the as-implanted projected range profile. During annealing the hydrogen concentration profile in the solid is assumed to be in local equilibrium with hydrogen gas filled cavities. Generation of a large internal gas pressure within the cavities occurs as the material achieves local equilibrium, and thus the hydrogen concentration can be related to the input fugacity of the source hydrogen and cavity inner pressure formed during annealing.

Phase equilibrium calculations for a system composed of Ba, Ti, O, and H were performed. For constant pressure and temperature conditions, the equilibrium state is defined by a global minimum in the Gibbs free energy. We searched for the global Gibbs free energy minimum by adjusting the proportions of chemical components across all of the possible species and phases as shown in Table 3.1, in which the 19 possible gaseous and 17 possible solid equilibrium and non-equilibrium species are shown for the Ba-Ti-O-H system. Phases that are thermodynamically unstable disappear in the search for the global Gibbs free energy minimum. We started the calculation with a fixed number of moles of Ba, Ti, O, and H, which were randomly distributed over the possible species. Phase equilibrium was defined by the values of the three independent variables that minimized the Gibbs free energy. This optimization problem was solved using SOLGASMIX-PV [5]. The independent variables were perturbed randomly to search for the global free energy minimum at fixed P and T conditions.

Figure 3.2 shows the phase diagrams with equilibrium solid-gas species varying with respect to annealing temperature. In the absence of hydrogen, solid BaTiO₃ along with volatile Ti and Ba oxides are predicted as shown in Figure 3.2(a). The different panels in (a) - (e) correspond to the calculation at different cavity pressures. The pressures are (a) 1.33×10^{-3} Pa without any implanted hydrogen, (b) 1.33×10^{-3} Pa after hydrogen implantation, (c) 1.33×10^3 Pa, (d) 6.7×10^6 Pa, and (e) 13.4×10^6 Pa. For the bulk BaTiO₃, we assumed that the crystal was in vacuum. On the other hand, for the system with hydrogen, we assumed that hydrogen resides at the ion projected range and forms micro-cavities during post-implantation processes. Figures 3.2(b) - (e) clearly

Table 3.1. Possible equilibrium species in the Ba-Ti-O-(H) chemistry obtained from JANAF thermochemical data and SOLGASMIX-PV code.

Gas Phase
$H_2, H^+, H_2O, HO^-, HO_2, H_2O_2, O^{2-}, O_2, O_3$
$Ba^{2+}, BaH^{3+}, BaOH^+, Ba_2, Ba(OH)_2, BaO, Ba_2O, (BaO)_2TiO, TiO_2, Ti^{4+}$
Solid Phase
$BaTiO_3, Ba_2TiO_4, BaO, BaH_2, Ba, Ba(OH)_2, BaO_2TiH_2, TiO(\alpha)$
$TiO(\beta), Ti_2O_3, TiO_2(\text{rutile}), TiO_2(\text{anatase}), Ti_3O_5, Ti_4O_7, Ti, H_2O, H_2O_2$

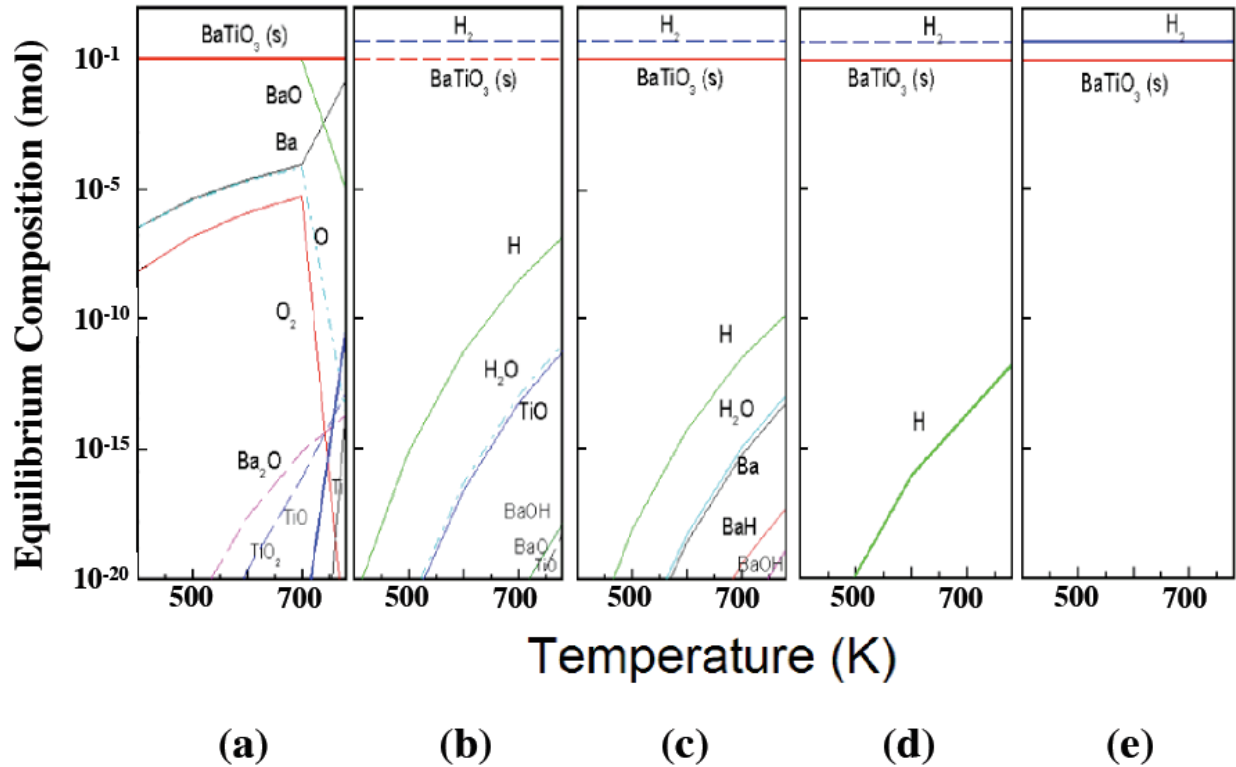


Figure 3.2. Equilibrium composition as a function of annealing temperature from 8×10^{-4} Pa - 1.33 MPa. The different panels in (a) - (e) correspond to the calculation at different cavity pressures. The pressures are (a) 1.33×10^{-3} Pa without any implanted hydrogen, (b) 1.33×10^{-3} Pa after hydrogen implantation, (c) 1.33×10^3 Pa, (d) 6.7×10^6 Pa, and (e) 13.4×10^6 Pa.

show a significant decrease, followed by disappearance of many of the volatile gas phase species, e.g. Ba^{2+} , Ba-O , Ba-OH , Ba-H , Ti^{4+} , and Ti-O with an increase of pressure. The calculations suggest that volatile oxide formation during high temperature annealing processes can cause the ratio of Ba^{2+} to Ti^{4+} to O^{2-} to become non-stoichiometric. However, in the presence of hydrogen, these oxide compounds can be effectively suppressed [Figure 3.2(b)]. The pressurized hydrogen reduces the formation of volatile oxides and acts as an agent for cavity nucleation, growth, and blistering during the layer transfer process.

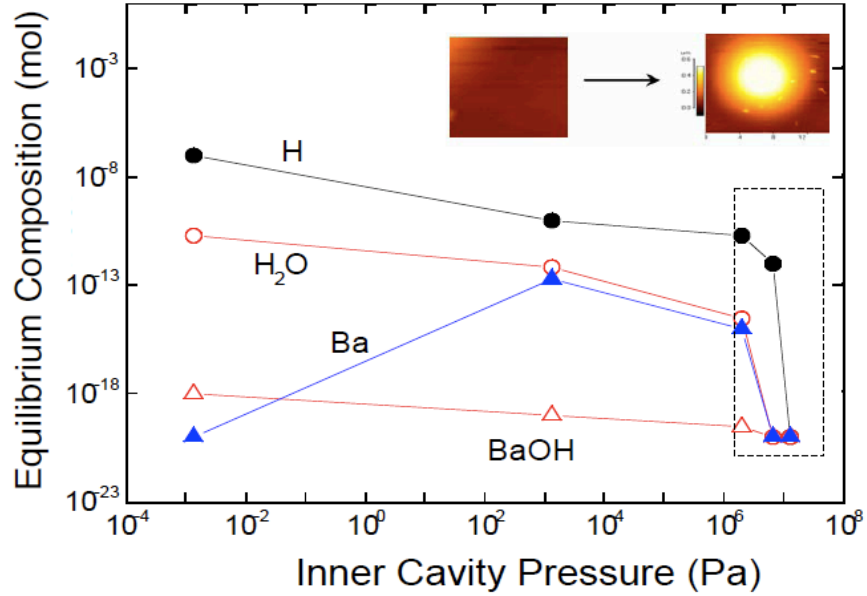


Figure 3.3. The change of pressure-dependent equilibrium composition in the Ba-Ti-O-H system at 500°C from Figure 3.2. The theoretically calculated cavity inner pressure from cavity geometry with radius and height measured by AFM ranges from 8×10^{-4} Pa to 0.2 GPa.

The change in concentration of gas species as a function of cavity inner pressure and geometry during annealing is shown in Figure 3.3. The inner pressure is calculated based on cavity dimensions measured from atomic force microscopy and assuming that cavity nucleation occurs uniformly in all directions in the plane of ion implantation. The excess pressure in the cavity relative to ambient pressure is written as:

$$\Delta p = \frac{64hEd^3}{12r^4(1-\nu^2)} \quad (3.1)$$

where E is the Young's modulus (120 GPa for BaTiO_3), d is the thickness of the layer, h is the height of the cavity, and ν is Poisson's ratio (0.3) [90]. The calculated cavity pressures were between 2 and 200 MPa. The main species in this pressure range ($> 10^{-9}$ mol) are H_2 , H^+ , H_2O , Ba^{2+} , and Ba-OH . In this range, there are no Ti-related species due to the lower free energy of formation of Ba-oxide species. In the range of pressures studied, the hydrogen gas partial pressure caused cavity nucleation followed by lateral cavity expansion. After the pressure reaches the point of cavity nucleation, the cavity begins to expand spontaneously in the rectangle area.

3.4.2 Cavity Formation and Real Hydrogen Behavior

During ion implantation, the implanted hydrogen atoms can combine with one of elements in the BaTiO_3 lattice forming X-H or X-OH complexes (where X is Ba or Ti) as shown by equilibrium calculations. During subsequent thermal annealing, implanted hydrogen diffuses in the vicinity of the implantation depth to form microcavities filled with H_2 . The high pressure inside a cavity acts as the driving force for its growth and expansion at the initial stage of annealing [115]. The minimum implanted hydrogen dose to enable blistering can be estimated to be:

$$\Phi_{min} = 8\gamma/3k_B T \quad (3.2)$$

where γ is a surface energy and k_B is Boltzmann's constant [43, 110]. Considering the surface energy of BaTiO_3 , one can estimate the minimum dose to be greater than 2×10^{15} ions/ cm^2 , which is consistent with reported values for other ferroelectric materials [96]. The ion dose used in this study ($> 1 \times 10^{16}$ cm^{-2}) was therefore high enough for cavity growth and blistering, Figure 3.4(a).

In order to investigate hydrogen diffusion during annealing, forward recoil electron scattering spectroscopy is used. This technique measures the depth at which hydrogen and deuterium are elastically scattered from an incident beam of energetic particles. In this case 2 MeV He^+ was used at the Cambridge Accelerator at Harvard University. Figure 3.5(a) shows the spectra for hydrogen in the implanted bulk BaTiO_3 after annealing at different temperatures where channel number 150 - 400 correspond to approximately 1 - 1.7 MeV for the energy of the recoiled particle. The behavior of hydrogen during the cavity growth and layer transfer process has been extensively studied in silicon [95, 121, 122]; however, no detailed reports on the hydrogen bonding configurations in the ferroelectric material systems have been reported. FT-IR studies in MIR geometries have revealed that the initial implantation damage, hydrogen passivation of internal defects and surfaces, and

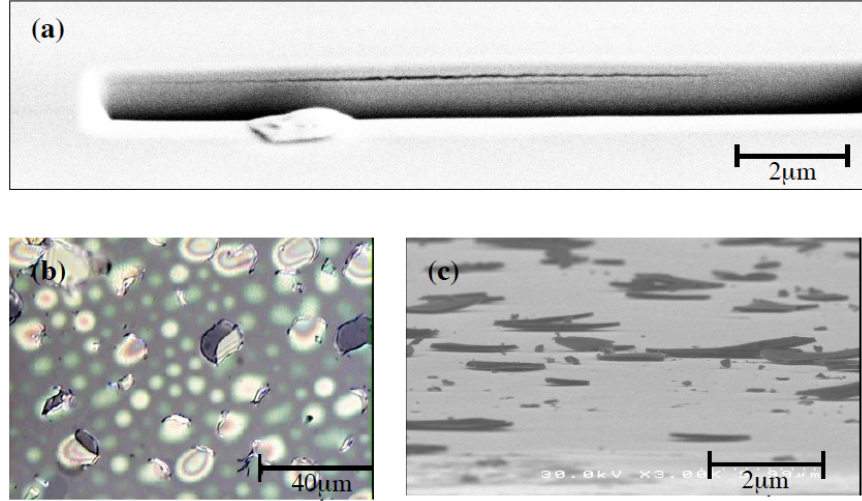


Figure 3.4. (a) FIB image of a cavity after Ga ion etching, (b) optical microscope image of cavity distribution and blistering, (c) SEM image of blisters on the sample surface. The average crater depth after the partial blistering is 450 nm for the lines and is consistent with the SRIM simulation results. The thickness is 450 - 500 nm as predicted by the SRIM simulation ($1 \times 10^{17} \text{ cm}^{-2}$, 80 keV).

the physical pressure created internally by H_2 formation are all essential elements for the layer splitting and exfoliation [12]. The desorption and out-diffusion of hydrogen with partial blistering are observed in the 300 - 500°C range. At 600°C, hydrogen concentration is comparable to surface contamination level and the overall surface of the BaTiO_3 was blistered, Figure 3.4(b) and (c).

In previous work, high concentrations of hydrogen have been shown to degrade the spontaneous polarization of ferroelectrics [15]. If hydrogen bonds to one of the elements in the lattice, polar hydroxyl $[\text{OH}^-]$ bonds can form and cause asymmetric stretching motion of the O-Ti-O bond. The change of symmetry in the Ti=O bond along the polarization axis of tetragonal unit cell would degrade the spontaneous polarization and actuating properties. However, in the Ba-Ti-O-H system, thermodynamic calculations of composition show that there are not a significant number of Ti-OH or Ti-H bonds, and considering the cavity inner pressure, there are no oxide species with high pressure hydrogen molecules. Also, Raman spectroscopy analysis shows no OH mode ($3200 \sim 3700 \text{ cm}^{-1}$, not shown here).

Forward recoil electron spectroscopy was also used to investigate the hydrogen desorption kinet-

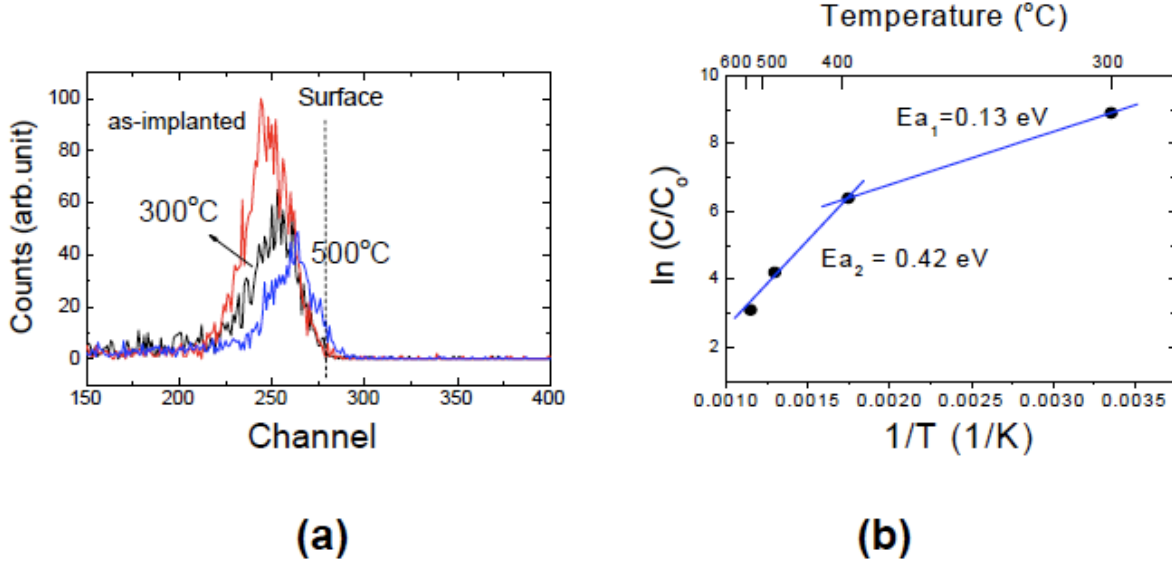


Figure 3.5. Forward recoil electron spectroscopy for (a) as-implanted BaTiO₃ (1×10^{17} cm⁻², 80 keV), annealed BaTiO₃ at 300°C and 500°C for 30 min. The He⁺ beam (2 MeV) is incident at the angle of 150° relative to the sample surface. (b) Arrhenius-type reaction of hydrogen release from FRES count integration. The FRES peak is normalized by the initial concentration (C_0) of as-implanted sample with the H⁺ dose of 1×10^{17} cm⁻² at 80 keV.

ics. By integrating the spectroscopy measurements as a function of temperature, an Arrhenius-type reaction of hydrogen release was plotted, Figure 3.5(b). By measuring the slope of this plot, the activation energy for hydrogen release was experimentally determined to be ~ 0.42 eV. This is similar to the corresponding energies reported for silicon [15]. It is believed that the hydrogen release reaction is not only thermally activated but also induced by physical reaction pathways generated from implantation damage. Above 600°C, there is no considerable amount of hydrogen detected in the bulk BaTiO₃.

Upon thermal release of hydrogen throughout the implanted layer, the hydrogen will diffuse to form small cavities. As the pressure in these cavities increases with time, cracks begin to form and beyond a critical radius, it will be energetically favorable for the cracks to continue growing until they merge with other cavities throughout the film. The final result is a fully exfoliated layer of BaTiO₃ whose thickness corresponds to the peak depth of ion implantation. This process is discussed in detail by Han et al. [46]

3.4.3 Microstructure of Ion Damaged Barium Titanate

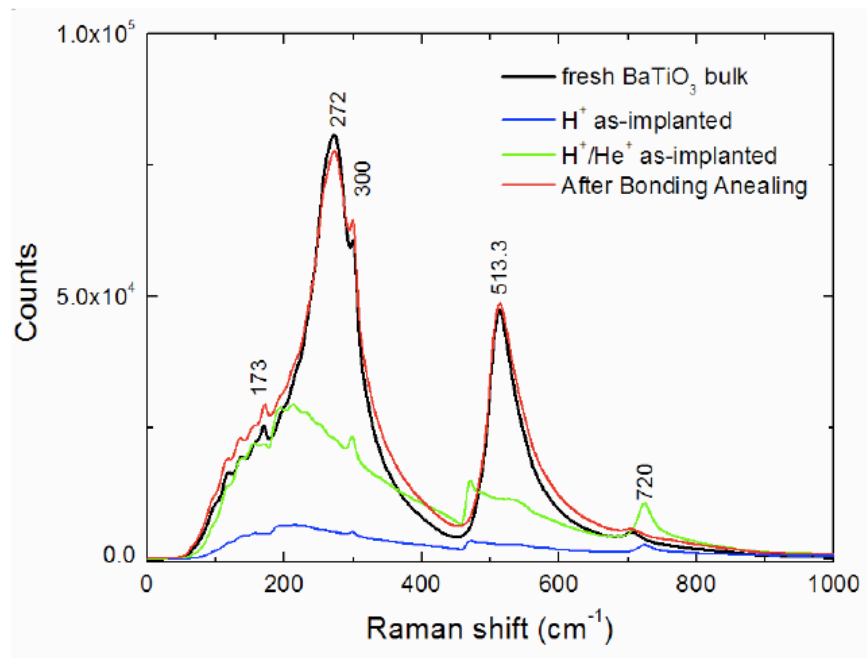


Figure 3.6. Micro-Raman spectra for the BaTiO₃ sample before processing, after the two implantation steps, and after bonding and annealing. The final spectra matches that of the sample before processing, indicating that proper post-bond annealing can return the transferred layer to its original, single crystal state.

In Figure 3.6, micro-Raman spectroscopy shows an unprocessed, bulk BaTiO₃ sample with a small shoulder peak at 305 cm⁻¹ and a broader peak at 710 cm⁻¹ [101]. These peaks are assigned to tetragonal BaTiO₃ and vanish above the Curie temperature. The two broad bands centered at 272 and 513 cm⁻¹ correspond to transverse optical phonons and their widths can be explained by large anharmonic coupling and a frequency dependent damping constant. The 272 and 513 cm⁻¹ peaks are observed in both the cubic and tetragonal phases, although they are broader in the cubic phase. After high energy ion implantation, the bulk BaTiO₃ contains a damaged layer at the implantation depth. This corresponds to the low Raman active mode in the H⁺ and H⁺/He⁺ as-implanted curves. Before the final annealing step, the broad peak at 200 - 400 cm⁻¹, along with the absence of a sharp 305 cm⁻¹ peak and a broad 705 cm⁻¹ suggests that the BaTiO₃ in this

layer is significantly damaged due to large number of local defects, as well as large residual stresses. In previous work, the authors showed that the layer splitting mechanism induced a change in the hardness and Young's modulus of the implanted BaTiO₃ donor wafer [89]. This can be explained by an increase in strain near the bubble region during the layer exfoliation process. After post-bond annealing, the micro-Raman curve is almost identical to the unprocessed, single crystal BaTiO₃. The sharp peaks at 272, 300, and 513.3 cm⁻¹ are again present, and the smaller peak at 705 cm⁻¹ has dissipated. These results verify that proper post-bond annealing can return the transferred BaTiO₃ layer to its single crystal state.

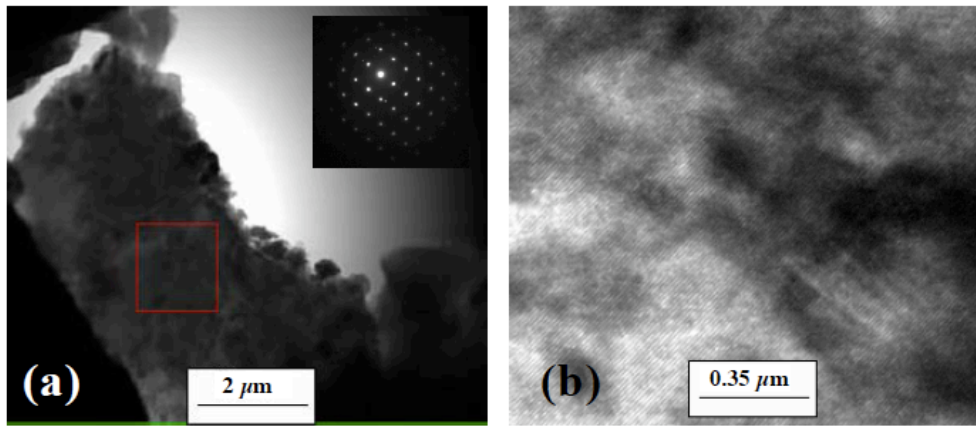


Figure 3.7. TEM images of layer transferred BaTiO₃. (a) shows a low magnification image with a selected area diffraction pattern along the (112) zone axis shown as an insert, and (b) shows a high resolution image of the film.

Figure 3.7 shows transmission electron microscope images of BaTiO₃ bonded to an amorphous carbon coated Cu grid. High resolution images, Figure 3.7(b), show that the BaTiO₃ film has a single-crystal lattice structure with a tetragonal lattice. This is confirmed by the selected area diffraction pattern shown as an inset in Figure 3.7(a). Energy dispersive x-ray spectroscopy scans confirm that the BaTiO₃ thin film has a stoichiometric Ba:Ti:O ratio of 1:1:3. These results show that the composition of the transferred BaTiO₃ film is the same as the donor wafer, and the crystallinity of this layer can be recovered after bonding and subsequent annealing.

3.4.4 Domain Characterization of the Transferred Ferroelectric Layer

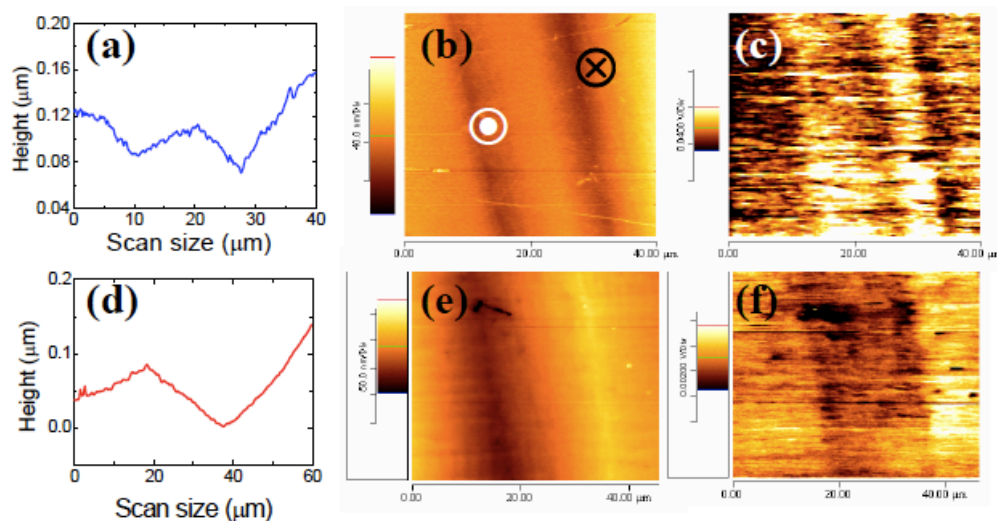


Figure 3.8. Comparison of surface morphology and polarization for bulk and transferred BaTiO₃. (a) AFM image of the transferred BaTiO₃ film, (b) PFM image of the transferred BaTiO₃ film, (c) AFM image of the bulk BaTiO₃, (d) PFM image of the bulk BaTiO₃, (e) AFM line scan of the transferred BaTiO₃ film along the domain walls, and (f) AFM line scan of the bulk BaTiO₃ film along the domain walls.

Single crystal barium titanate thin films with thicknesses between 150 and 800 nm were successfully transferred to Si₃N₄/Si and Pt/Si₃N₄/Si substrates. The 800 nm thick films on Pt/Si₃N₄/Si substrates were approximately 1 mm x 2 mm, and 400 nm thick films on Si₃N₄/Si were approximately 5 mm x 5 mm [89]. Atomic force microscopy line scans, Figure 3.8(a), of the transferred BaTiO₃ samples show a domain structure similar to that of bulk BaTiO₃, Figure 3.8(d). The c-domain (where the c-axis is oriented perpendicular to the film, Figure 2.2) and a-domain spacing in the transferred layer is approximately half of the equivalent distance in the bulk single crystal. This can be attributed to additional stresses which are imparted on the film during the layer transfer process. Piezoresponse force microscopy imaging in Figure 3.8(b) also shows c-a domain configurations similar to a bulk single crystal, Figure 3.8(e). The surface corrugation angle

($\theta = 90^\circ - 2\arctan(a/c)$) is $0.5 - 0.6^\circ$. In the piezoresponse image [Figure 3.8(c) and (f)], the bright and dark areas originate from regions where the polarization vectors point into and out of the plane, respectively. Since the domain structure is similar in both the single crystal and the transferred layer, one can conclude that layer transfer yields high-quality films with properties very similar to bulk single crystals.

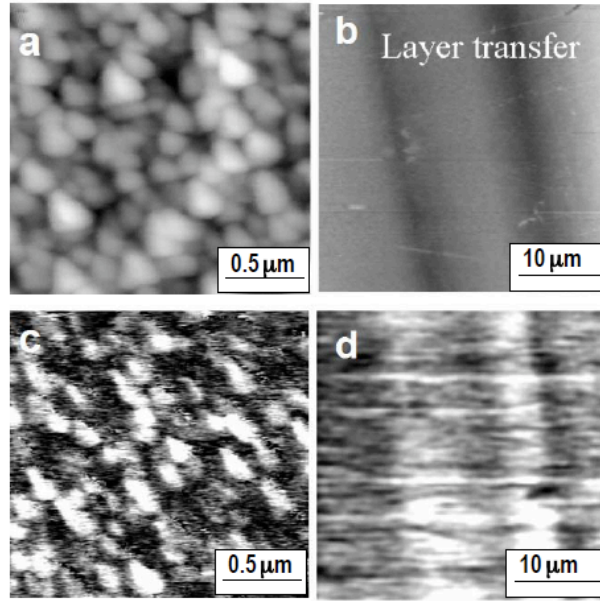


Figure 3.9. Comparison of AFM [(a) and (b)] and PFM [(c) and (d)] images for the BaTiO₃ thin films. (a) and (c) are of a PLD BaTiO₃ thin film. (b) and (d) are of a layer transferred thin film BaTiO₃. PFM measurement conditions were $V_{ac} = 1.5$ V and a tip frequency of 20 kHz. Note that the AFM/PFM images of both films show different lateral scan sizes.

For comparison, a BaTiO₃ film grown using pulsed laser deposition is shown in Figure 3.9(c) and (d). These films on Pt substrates produce crystallographically textured films which exhibit some grain misorientation. Their domain polarization characteristics and structure are influenced by domain misorientations and grain boundaries, Figure 3.9(d). Therefore, pulse laser deposited BaTiO₃ films exhibit grain scale morphology as opposed to the domain scale morphology of the transferred films.

In order to confirm the piezoelectric nature of the BaTiO₃ film, we obtained a hysteresis curve,

Figure 3.10, for a single ferroelectric domain. Here the conducting atomic force microscope tip served as the top electrode. While both BaTiO₃ films showed piezoelectric hysteresis, the transferred film showed a larger piezoresponse, larger effective piezoelectric constant (d_{33}^{eff}) of 90 pm/V, and smaller coercive field (~ 20 kV/cm) than the donor substrate. Clamping effects are taken into account using the equation:

$$d_{33}^{eff} = d_{33} - \frac{2d_{31}s_{13}}{s_{11} + s_{12}} \quad (3.3)$$

The resulting single crystal d_{33} value, $d_{33} = 129$ pm/V, is consistent with those reported elsewhere [59, 87, 102, 103].

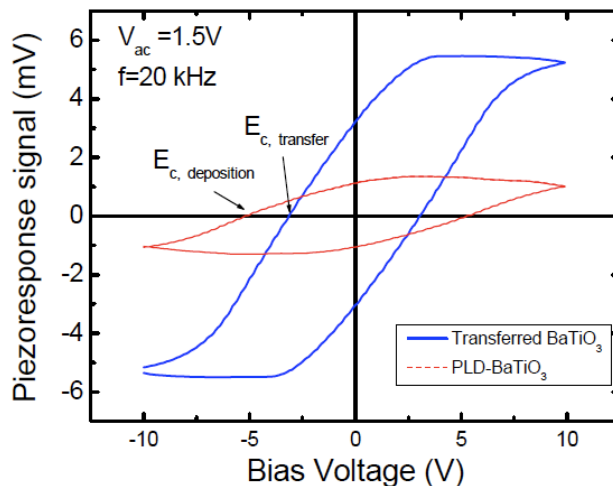


Figure 3.10. Local piezoresponse hysteresis curves comparing PLD BaTiO₃ on a Pt/Si substrate and layer transferred BaTiO₃ on Pt.

3.5 Conclusion

In this chapter we have performed single-crystal layer transfer and have reported mechanisms for cavity formation in ion-implanted, single-crystal BaTiO₃. Analysis of the equilibrium concentration of species as a function of annealing temperature was performed. From this, it was shown that released hydrogen during thermal annealing suppresses the formation of volatile oxides which might otherwise degrade the performance of the ferroelectric films. The hydrogen pressure inside the

platelets created during thermal annealing was sufficiently high to form cavities inside the implanted substrate. BaTiO₃ films, 150 - 800 nm thick, have been transferred onto Pt and Si₃N₄ layers. Micro-Raman analysis showed that lattice damage to the BaTiO₃ that occurs during the layer transfer process can be effectively removed with proper annealing. The transferred BaTiO₃ thin films show domains identical to those found in bulk crystals. Piezoresponse force microscopy shows that the film is piezoelectrically active with domain configurations similar to that of bulk crystals. The transferred films show larger piezoresponse and smaller coercive fields than those associated with BaTiO₃ films grown by traditional methods. Based on these results, ion implantation-induced layer transfer has been successfully utilized to create high-quality single-crystal ferroelectric thin films that can be bonded to substrates with significant thermal expansion mismatch.

Chapter 4

Analysis of Competing Failure Mechanisms in Layer Transferred Thin Films

4.1 Introduction

In this chapter, we develop the criterion for successful layer transfer from a thin film mechanics standpoint. To insure proper thin film exfoliation, samples of lithium niobate were implanted with hydrogen and helium based on the criterion developed in Chapter 3. The analysis of transverse cracks, often observed in thin films obtained by the layer transfer technique, is done for films in a state of tensile and compressive stress. The level of stress imposed on the film during heating due to the mismatch in thermal expansion coefficients between the substrate and thin film is shown to be the dominant factor in determining the quality of the transferred layer. In particular, it is shown that if the film is submitted to a tensile stress, the microcracks produced by ion implantation are not stable and deviate from the plane of implantation, causing the layer transfer process to fail. Conversely, if the transferred layer is in compressive stress exceeding a threshold value, then the film can buckle and delaminate, leading to transverse cracks induced by bending. As a result, we show that the imposed stress σ_m - which is determined by the temperature to which the samples are heated - must be within the range $-\sigma_c < \sigma_m < 0$ to produce an intact thin film where σ_c depends on the interfacial fracture energy and the size of defects at the interface between film and substrate. ¹

¹This chapter is based on work done with Dr. Laurent Ponson who was the lead author on this paper. The theory portion of this chapter was derived by Dr. Ponson after joint discussions and the experimental verification of this theory was done by myself [94].

4.2 Layer Transfer and Lithium Niobate

Various applications in electronics and optics require the synthesis of high quality, defect-free single crystals on a substrate of a different material. Diverse heteroepitaxial growth processes have been proposed e.g., Reference [16], but these methods impose severe restrictions on the film/substrate combinations. Recently, the layer transfer process has been proposed and shows promise as an alternative when the film/substrate pair is very different [22, 87]. However, for some systems and heating conditions, undesirable transverse cracks are also produced in the thin film during the process. This phenomenon renders the transferred thin film useless for applications in microelectronics and others fields. Therefore, understanding the origin of such cracks is crucial to avoid their formation. Identifying quantitatively the conditions and the systems that are advantageous to nucleate undesirable cracks will help to define the limitations of the layer transfer process and to design possible solutions to overcome these limitations. This motivates the present analysis and the mechanism of formation of these undesirable cracks is the central point of this study.

In Section 4.3, the geometry used during the layer transfer process as well as the state of stress in the film are described. Then, a first possible origin of thin film failure is investigated in Section 4.4: the stability of cracks nucleating from defects introduced by ion implantation is analyzed, and we show that these cracks only propagate parallel to the film/substrate interface when the transferred film is in a state of compressive stress. In Section 4.5, we show that excessive compressive stress in film can lead to cracking by buckling, delamination, and then failure of the film. For a given system with fixed film thickness, this analysis provides an acceptable range for the compressive stress and as a result, limitations on the heating temperatures used during layer transfer. In Section 4.6, these theoretical predictions are combined with experimental observations made on a lithium niobate film bonded to a silicon substrate. The two failure mechanisms previously proposed are clearly identified in an analysis of the specimen after layer transfer. The theoretical criterion for good layer transfer ($-\sigma_c < \sigma_m < 0$) is found to agree with experimental observations.

4.3 Geometry of the System and Stress State of the Film

To perform layer transfer, the material to be cut is bonded on a substrate as shown in Figure 4.1. A bonding layer, observed to improve adhesion and avoid undesirable cracking for some systems, is also shown. Its influence on the whole system is limited to the interface properties between film and substrate (fracture energy and defect size) so that this interlayer can be neglected

in the following analysis without loss of generality. Such a layered system is then submitted to an elevated temperature ΔT and microcracks can nucleate in the plane of hydrogen and helium ion implantation within the film. This is represented as a dashed plane in Figure 4.1. When these microcracks coalesce, the bulk single crystal is separated from the transferred thin film with thickness h .

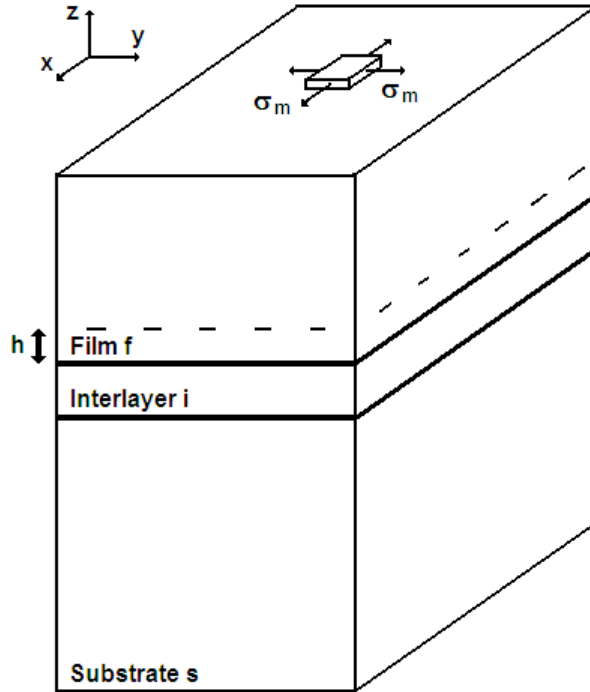


Figure 4.1. Geometry and stress field of the layered system. The dashed plane coincides with the plane of ion implantation and the thickness of the transferred layer, h , corresponds to the depth of ion implantation.

During the heating phase of the process, the film is submitted to a homogeneous biaxial stress σ_m caused by the mismatch in thermal expansion between the film and the substrate. Noting $\Delta\alpha = \alpha_s - \alpha_f$, the difference between the linear thermal expansion coefficients of the substrate and the film, one can show that irrespective of the thickness and thermal properties of the bonding layer, that the stress in the film is given by [44]:

$$\sigma_m = \frac{E}{1 - \nu} \Delta T \Delta\alpha \quad (4.1)$$

where E and ν are the Young's modulus and the Poisson's ratio of the film, respectively. We will

see that to ensure transfer of a thin film without undesirable transverse cracks, the stress imposed on the film must be within a certain range of values to be determined in Sections 4.4 - 4.7.

4.4 Stability of Microcracks in the Film

We first focus on the trajectory of microcracks that initiate from the defects induced by the presence of hydrogen and/or helium in the specimen. To result in layer transfer, these microcracks are expected to propagate in a relatively straight manner, i.e., parallel to the interface between the film and the substrate. The stability analysis of a one-dimensional (1D) crack propagating in a two-dimensional (2D) elastic medium submitted to an internal stress was performed by Cotterell and Rice [27]. To apply this result to the layer transfer process, we should make the hypothesis that the behavior of the three-dimensional (3D) system as represented in Figure 4.1 is analogous to that of a cut of the full system along a plane perpendicular to the film/substrate interface, e.g., the plane (OYZ). In other words, we should suppose that the 2D penny-shaped microcracks propagating in the plane of ion implantation of the film can be approximated by 1D crack lines. This simplification is *a priori* not obvious, and in the following, we will study the propagation of a 2D crack in a 3D elastic medium. Figure 4.2 represents a part of the crack front of a 2D penny-shaped microcrack when observed at a sufficiently small scale so that the crack front appears roughly straight. The average front is taken parallel to the z axis of the local coordinates (O_{xyz}) and propagates along the x axis. As a result, the crack propagates in a plane parallel to (x, z) , i.e., parallel to the interface between the film and the substrate. The question we address here is whether the crack will go on propagating within a plane parallel to (x, z) or will deviate from the straight trajectory because of the deflections generated by local heterogeneities in the film such as those induced by ion implantation. To proceed to such a stability analysis, we slightly perturb the crack front with respect to the straight geometry and study if those perturbations will tend to zero or will diverge while the crack is propagating. We define both out-of-plane perturbations $f(x, z)$ (along the y axis) and in-plane perturbations $g(z, t)$ (along the x axis) that are represented in Figure 4.2.

One can show that for small deflections, only the out-of-plane perturbations $f(x, z)$ are relevant to determine the local shearing $K_{II}(x, z)$ at the crack tip and, hence, the trajectory of the crack [62]. Let us note that the following analysis is independent of the shape of the small crack perturbations and remains valid whatever the choice of g and f are. To predict the crack trajectory, we apply the principle of local symmetry [27, 45, 49]: locally, at every point of the front $M(x, f(x, z), z)$, the

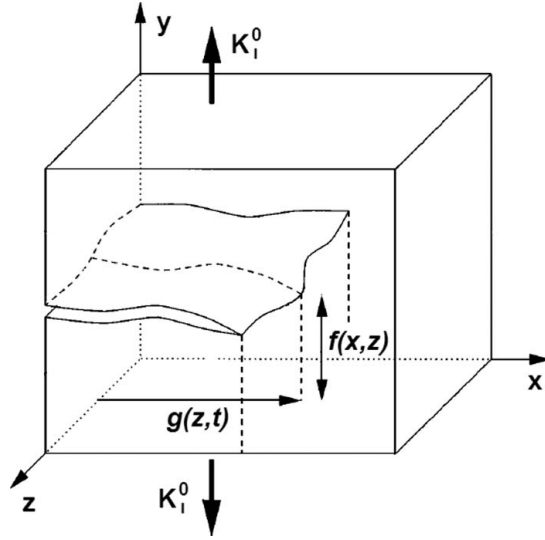


Figure 4.2. Geometry of a slightly perturbed crack propagating in the film.

crack propagates in a pure mode I opening state of stress. This condition is written as:

$$K_{II}[M(x, f, z)] = 0 \quad (4.2)$$

Movchan *et al.* [75] calculated the mode II stress intensity factor of a slightly perturbed crack propagating in an infinite 3D elastic medium for any perturbation $f(x)$.² Using their result, the local mode II stress intensity factor of cracks propagating in the ion implanted plane of the specimen can be expressed as:

$$K_{II} = \frac{K_I^0}{2} \frac{\partial f}{\partial x} \Big|_{(x,z)} - \frac{K_I^0}{2\pi} \frac{2-3\nu}{2-\nu} \int_{-\infty}^{+\infty} \frac{f(x, z') - f(x, z)}{(z' - z)^2} dz' + \Delta K_{II}^{memory} \quad (4.3)$$

where the *memory* term K_{II}^{memory} is given by:

$$\begin{aligned} \Delta K_{II}^{memory}(x, z) = & - \int_{-\infty}^x \int_{-\infty}^{+\infty} \left\{ w_x^{II}(x - x', z - z') \left(\frac{\partial(fT_{xx})}{\partial x} \Big|_{(x',z')} + \frac{\partial(fT_{xz})}{\partial z} \Big|_{(x',z')} \right) \right. \\ & \left. + w_z^{II}(x - x', z - z') \left(\frac{\partial(fT_{xz})}{\partial x} \Big|_{(x',z')} + \frac{\partial(fT_{zz})}{\partial z} \Big|_{(x',z')} \right) \right\} dx' dz' \end{aligned} \quad (4.4)$$

²Here, mode I stress is defined as tensile stress normal to the plane of the crack and mode II stress is defined as shear stress parallel to the crack plane and perpendicular to the crack front.

with

$$\begin{aligned}
w_x^{II}(x, z) &= \frac{\sqrt{-2x}H(x)}{\pi^{3/2}*(x^2+z^2)} \left(1 + \frac{2\nu}{2-\nu} \frac{1-(z/x)^2}{1+(z/x)^2} \right) \\
w_z^{II}(x, z) &= \frac{\sqrt{-2x}H(x)}{\pi^{3/2}*(x^2+z^2)} \frac{2\nu}{2-\nu} \frac{2z/x}{1+(z/x)^2}
\end{aligned} \tag{4.5}$$

where $H(x)$ is the Heaviside function. In the preceding expressions, K_I^0 represents the average mode I stress intensity factor applied to the crack by the heated gas in the microcavities, while T_{xx} , T_{zz} , and T_{xz} are the T-stress terms or constant stresses imposed on the film in the absence of cracks. This implies that $T_{xx} = \sigma_m$, $T_{zz} = \sigma_m$, and $T_{xz} = 0$. Equation 4.3 provides the different contributions to the mode II shearing at a point M of the crack front induced by the perturbations of the fracture surface. The first term in Equation 4.3 corresponds to the contribution of the local slope along the propagation direction, while the second term provides the shearing induced by perturbations of the crack front. The third term, also referred to as the memory term, gives, as indicated by its name, the mode II contribution induced by the out-of-plane deviations of the crack line between its point of initiation and current position. This term is expressed as a function of the internal stress σ_m in the film, using the full expression of Equation 4.4 and changing T_{xx} , T_{zz} , and T_{xz} by their relevant expressions. Isolating the first term proportional to the local slope of the crack surface, the expression of the crack path, as given by the principle of local symmetry of Equation 4.2, can be rewritten as:

$$\begin{aligned}
\frac{\partial f}{\partial x} \Big|_{(x,z)} &= \frac{1}{\pi} \frac{2-3\nu}{2-\nu} \int_{-\infty}^{+\infty} \frac{f(x,z')-f(x,z)}{(z'-z)^2} dz' \\
&+ \sigma_m \frac{2}{K_I^0} \int_{-\infty}^x \int_{-\infty}^{+\infty} \left(w_x^{II}(x-x', z-z') \frac{\partial f}{\partial x} \Big|_{(x',z')} + w_z^{II}(x-x', z-z') \frac{\partial f}{\partial z} \Big|_{(x',z')} \right) dx' dz'
\end{aligned} \tag{4.6}$$

This equation predicts the crack path and so the stability of the failure process: let us take a perturbation of the crack oriented along the positive y axis so that $f > 0$. If $\frac{\partial f}{\partial x} < 0$, the local perturbation $f(x, z)$, is rapidly suppressed during crack propagation, and the crack surface is on average flat. On the other hand, if $\frac{\partial f}{\partial x} > 0$, even a small perturbation will grow and will lead to a macroscopic deviation of the crack from the (x, z) plane parallel to the interface. In the latter case, crack propagation becomes unstable. This situation will clearly lead to catastrophic transverse cracks in the thin film during the layer transfer process.

Next, we assess the relevance of each term of the righthand side of Equation 4.6 that determines the stability of microcracks in the film during heating. The first term acts as a nonlocal restoring force along the crack front that tries to maintain a straight trajectory. However, this term does

not prevent the crack from deviating from the mean crack plane³ and therefore does not contribute directly to the stability of the crack. The second term is composed of a part proportional to $\frac{df}{dx}$ and another part proportional to $\frac{df}{dz}$. To assess the relative importance of each term, one can compare their two prefactors, w_x^{II} and w_z^{II} , respectively. According to Equation 4.5, w_z^{II} is smaller than w_x^{II} ⁴, and for most values of (z, x) , one gets $\frac{w_x^{II}}{w_z^{II}} \ll 1$. In other words, the stability of the crack is mainly dictated by the term proportional to $\frac{df}{dx}$, leading to the approximation:

$$\left. \frac{\partial f}{\partial x} \right|_{(x,z)} \simeq \sigma_m \frac{2}{K_I^0} \int_{-\infty}^x \int_{-\infty}^{+\infty} w_x^{II}(x-x', z-z') \left| \frac{\partial f}{\partial x} \right|_{(x',z')} dx' dz' \quad (4.7)$$

From this equation, one can assess the evolution of the local slope of the crack surface. From Equation 4.5, one notes that $w_x^{II} > 0$. Therefore, the sign of σ_m will determine the evolution of the solution of Equation 4.7. If $\sigma_m > 0$, then $\left| \frac{\partial f}{\partial x} \right|$ is expected to increase when the crack propagates, while with $\sigma_m < 0$, $\frac{\partial f}{\partial x}$ will tend to zero after a finite distance.⁵

From analysis of the stability of a crack propagating during heating, one obtains:

- (i) If the thin film is in a state of tensile stress ($\sigma_m > 0$), then the microcracks nucleated from the damage induced by ion implantation during the heating phase will deviate from the plane of implantation. One can therefore expect transverse cracks within the transferred thin film from systematic deviations of these microcracks.
- (ii) If the film is in a state of compressive stress ($\sigma_m < 0$), then the microcracks are expected to propagate along a straight trajectory within the plane of ion implantation and will result in the transfer of a crack-free single crystal thin film. This compressive stress state is obtained if the thermal expansion coefficient of the film is larger than that of the substrate [see Equation 4.1].

As a result, the condition $\sigma_m < 0$ is necessary to obtain straight crack propagation and therefore an intact thin film. Let us note that this result is not limited to multilayer systems and can be extended to other systems where the crack trajectory needs to be analyzed: a 2D crack will remain

³For example, one can consider a crack with a perfectly straight front $f(x, z) = f(x)$. In that case, this term equals zero but f can be arbitrarily large, leading to unstable crack propagation.

⁴One can show that $\frac{w_z^{II}(x,z)}{w_x^{II}(x,z)} \leq \frac{2\nu}{2-\nu}$.

⁵For example, one can derive Equation 4.7 with respect to the variable x . Considering an initial perturbation $\frac{\partial f}{\partial x} > 0$, the sign of $\frac{\partial(\frac{\partial f}{\partial x})}{\partial x}$, and therefore the stability of the crack - positive (respectively, negative) for an unstable (respectively, stable) crack - is then provided by the sign of σ_m .

confined to a plane perpendicular to the external tensile loading if the stress is in compression along all the directions of this plane, while it will deviate from the straight trajectory if the stress is tensile along the mean plane of the crack. This analysis shows that the stability criterion shown for 2D elastic solids under mode I loading [27] remains valid for 3D systems. In Section 4.5, we will investigate another possible origin of film cracking and show that there is a limit to the amount of compressive stress the film can support, and an excessively high compressive stress in the film can also lead to poor quality transferred thin films.

4.5 Buckling, Delamination, and Failure of the Film

Here, another possible mechanism for film cracking during layer transfer process is investigated. Previously, we have shown that a state of tensile stress in the crystal containing the implanted plane must be avoided to ensure proper layer transfer. Therefore, systems with negative mismatch $\Delta\alpha = \alpha_s - \alpha_f$ between thermal expansion coefficients of the substrate and the film will be advantageously chosen. As an indirect consequence, the thin film freshly obtained may undergo a high compressive stress $\sigma_m < 0$, as given by Equation 4.1.

It is well known that thin films under compression can buckle and delaminate [44, 52]. We will see that these processes can have catastrophic consequences because it can lead to film failure by bending. The conditions leading to buckling, delamination, and failure of the film produced by layer transfer and subjected to a compressive stress σ_m are investigated in detail in Sections 4.5.2, 4.5.3, and 4.5.4, respectively. The film is supposed to be perfectly brittle so that the equations of elasticity for thin plates can be used. In addition, in first approximation, the fracture energy G_c of the film/substrate interface is assumed to be constant and independent of the phase angle $\phi = \arctan\left(\frac{K_{II}}{K_I}\right)$ of the stress acting on the interface [44].

4.5.1 Delamination of a Film with a Semi-Infinite Defect

Under compressive stress, a film bonded to a substrate can delaminate in order to release its internal stress. For an infinite film bonded to an infinite rigid substrate with a straight delamination front separating the film into two semi-infinite bonded and debonded parts, the elastic energy released during the propagation over a unit area is given by [44]:

$$G_{del} = \sigma_m^2 \frac{h}{2} \frac{1 - \nu^2}{E} \quad (4.8)$$

where h , E , and ν are the thickness, the Young's modulus, and the Poisson's ratio of the film, respectively. Let us note that we do not consider cases where the substrate modulus is appreciably smaller than that of the film. This situation has been considered elsewhere [126]. Noting G_c the interfacial fracture energy between the film and the substrate [or the bonding layer if it has been added to the system (Figure 4.1)], one can use the Griffith criteria $G_{del} = G_c$ providing the onset of crack propagation to get an expression of the critical stress σ_{del} for delamination,

$$\sigma_{del} = \sqrt{\frac{2EG_c}{h(1-\nu^2)}} \quad (4.9)$$

It must be emphasized that the initial condition taken here with a semi-infinite debonded zone favors interfacial crack propagation. In more realistic systems with defects or debonded zones of finite size at the interface between film and substrate (or bonding layer), such a level of compressive stress might not induce delamination. In addition, another mechanism must be taken into account to describe the delamination of films: buckling, frequently observed in thin film under compression, leads to modifications of the expression of the energy release rate G as given in Equation 4.8. In the following section, we focus on this process and the conditions for film buckling. The out of plane displacements of the film are then taken into consideration in order to predict propagation of the delamination crack. In all the following, we limit our analysis to a 2D geometry of the specimen [e.g. plane (O_{xy}) in Figure 4.1]. We consider defects of length $2a$ at the interface between film and substrate and determine if these debonded zones can grow and lead to catastrophic consequences for layer transfer.

4.5.2 Buckling of the Film

We consider the situation represented in Figure 4.3(a) where an initial defect or debonded zone of size $2a$ is present at the interface between the film and the substrate. Under a sufficiently high compressive stress, the film can buckle as shown in Figure 4.3(b), and a stability analysis of the film provides expression for the critical stress [44].

Consider now that the film is submitted to a given compressive stress σ_m . One can use this expression to show that buckling will occur if the delamination zone is larger than a critical size a_b , where:

$$a_b = \frac{\pi h}{2} \sqrt{\frac{E}{3(1-\nu^2)|\sigma_m|}} \quad (4.10)$$

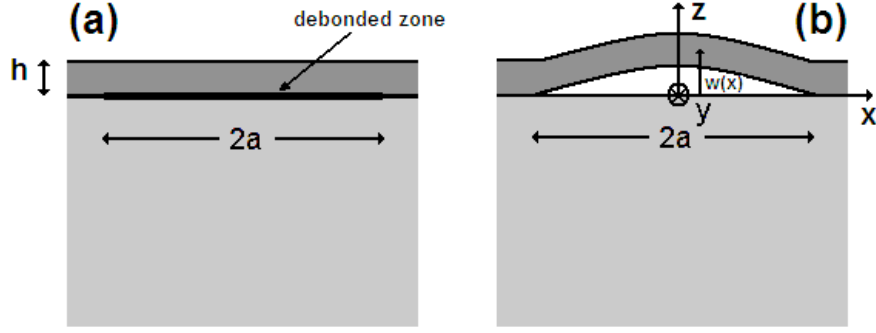


Figure 4.3. Two-dimensional profile of a debonded part of a film (a) without and (b) with buckling.

This process is energetically favorable because, in essence, it increases the effective length of the film.

4.5.3 Propagation of the Delamination Front Induced by Film Buckling

As mentioned previously, buckling of the film affects the energy release rate of the interfacial crack so that the buckling pattern must be taken into consideration when predicting the onset of delamination. In particular, the stress concentration at the edge of a debonded zone changes drastically with the size of the buckling zone. This effect is represented in Figure 4.4 where the variations in the energy release rate G are represented as a function of the half-length a of the debonded zone. For sufficiently large buckling zones, G might reach G_c and the interfacial crack can propagate. To assess the critical size a_p that allows a buckling pattern to propagate, one can derive the value of the energy release rate for a buckled zone of length $2a$ [44],

$$G(a) = \frac{\sigma_m^2(1-\nu^2)h}{2E} \left(1 - \frac{a_b^2}{a^2}\right) \left(1 + 3\frac{a_b^2}{a^2}\right) \quad (4.11)$$

that is represented in Figure 4.3(b). It is interesting to note that at the onset of film buckling ($a = a_b$), there is no driving force for delamination ($G = 0$). However, if the compressive stress in the film is increased, the value of $a_b(\sigma_m)$ will decrease leading finally to a net increase in the delamination driving force. As a result, propagation is possible at a certain stress level when the condition $G(a) = G_c$ is satisfied. Solving the previous equation with respect to a , one obtains the critical length a_p above which the buckling zone will propagate,

$$a_p = \frac{\pi h}{2} \sqrt{\frac{E}{1-\nu^2}} \frac{1}{\sqrt{|\sigma_m|}} \frac{1}{\sqrt{1 + \sqrt{4 - \frac{6EG_c}{h(1-\nu^2)\sigma_m^2}}}} \quad (4.12)$$

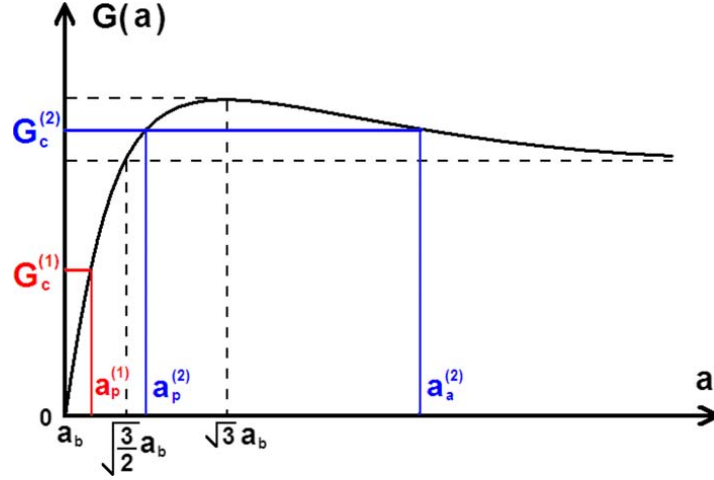


Figure 4.4. Variations in the energy release rate of an interfacial crack at the edge of a buckled zone of length $2a$ [Figure 4.3(b)]. $2a_b$ corresponds to the minimum length for a debonded zone in a film of the same thickness under the same compressive stress to buckle.

a_p being a decreasing function of $|\sigma_m|$, it is also clear in this representation that a sufficiently large compressive stress will induce delamination. Note that Equation 4.12 is only valid for $|\sigma_m| > \frac{\sqrt{3}}{2}\sigma_{del}$ where σ_{del} has been introduced in Equation 4.9. For smaller values of compressive stress $|\sigma_m|$ in the film, the buckling zone remains stable regardless of the initial size of the debonded zone.

However, the previous analysis is limited to crack initiation and to predict the full evolution of the system beyond initiation, it is important to separate two cases, as illustrated in Figure 4.4:

- (1) If the critical length a_p for interfacial crack propagation is smaller than $\sqrt{\frac{3}{2}}a_b$, where a_b is the critical length for buckling [Equation 4.10], the equation $G_c = G(a)$ has only one solution a_p given by Equation 4.12, corresponding to the size of the smallest defect leading to crack initiation. The condition $G_c \geq G(a)$ for crack propagation begin satisfied whenever $a > a_p$, this situation corresponds to crack propagation without arrest.
- (2) If the length a_p is larger than $\sqrt{\frac{3}{2}}a_b$, the equilibrium equation for debonding is satisfied for two crack lengths, a_p and a_a . The elastic energy released is larger than the fracture energy only for crack extensions between these two length scales so that initiation and crack arrest

occur successively for $a = a_p$ [Equation 4.12] and a_a , with:

$$a_a = \frac{\pi h}{2} \sqrt{\frac{E}{1-\nu^2}} \frac{1}{\sqrt{|\sigma_m|}} \frac{1}{\sqrt{1 + \sqrt{4 - 3 \left(\frac{\sigma_{del}}{\sigma_m}\right)^2}}} \quad (4.13)$$

The conditions for both situations can be rewritten in terms of stress, and unstable crack propagation corresponds to $|\sigma_m| \geq \sigma_{del}$, while crack arrest will be observed if $\sigma_{del} > |\sigma_m| \geq \frac{\sqrt{3}}{2} \sigma_{del}$. The value of the defect length corresponding to $a_p = a_a$ is noted a_{del} , where:

$$a_{del} = \frac{\pi h^4}{2} \sqrt{\frac{2hE}{3G_c(1-\nu^2)}} \quad (4.14)$$

In both cases, the propagation of these interfacial cracks may adversely affect the quality of the transferred thin film. In particular, for sufficiently large buckled patterns, i.e., large enough interfacial crack extension, a transverse crack induced by the bending generated in the film can fracture the crystal layer. It is worth noting that this process may not occur for an interfacial failure with a small extension. The conditions to obtain such transverse cracks are now discussed in detail.

4.5.4 Failure of the Thin Film Induced by Bending

When buckling occurs, the delaminated zone undergoes bending. If the original debonded zone is sufficiently small, bending increases while the size of the buckling zone increases. For a sufficiently large buckling zone, the film is not strong enough to support the tensile stress induced by bending in the film and a crack initiating from the upper surface of the film in $x = 0$ will propagate parallel to the y axis toward lower surface [Figure 4.3(b)]. In this geometry, crack propagation is expected to be without arrest, and propagation will occur throughout the crystal layer.

To predict the onset of crack initiation, we use a criterion based on the value of the curvature of the film (akin to critical strain), as e.g. in Ref. 15: failure occurs when the curvature $\frac{d^2w}{dx^2}$ at some point of the film exceeds the critical value $\frac{1}{R_c}$, where R_c is a constant depending not only on the intrinsic strength of the material but also on the state of surface of the freshly cut crystal. As seen in Figure 4.3(b), a possible transverse crack will initiate around $x = 0$ where the local curvature of the film is maximum. The deflection $w(x)$ of the film is then expressed in terms of the delaminated zone size $2a$ and the compressive stress σ_m (e.g., Ref. 4), providing an expression for

the maximum curvature $\left. \frac{d^2 w}{dx^2} \right|_{x=0}$ of the film. From this expression and the curvature based failure criterion introduced previously, one can show that transverse failure occurs for buckled thin film larger than a_f , with:

$$a_f = \pi \sqrt[4]{3(1-\nu^2)} \sqrt{hR_c} \sqrt{\frac{|\sigma_m|}{\sigma_l}} \sqrt{1 - \sqrt{1 - \left(\frac{\sigma_l}{\sigma_m}\right)^2}} \quad (4.15)$$

where

$$\sigma_l = \frac{E}{2\sqrt{3(1-\nu^2)}} \frac{h}{R_c} \quad (4.16)$$

Note that the film failure is impossible if $|\sigma_m| < \sigma_l$, regardless of the size of the debonded zone. For $|\sigma_m| = \sigma_l$, we introduce the size $a_l = a_f(\sigma_l)$ of the smallest debonded zone for which failure will occur

$$a_l = \pi \sqrt[4]{3(1-\nu^2)} \sqrt{hR_c} \quad (4.17)$$

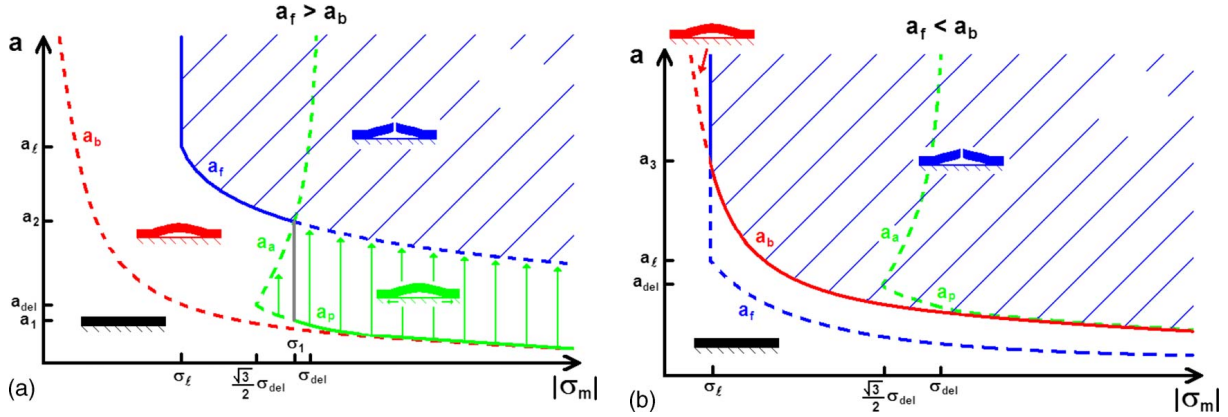


Figure 4.5. Diagrams representing the state of the system and its evolution during the layer transfer process in two different cases; (a) film with high resistance to failure/small thickness ($a_f > a_b$); (b) film with low resistance/large thickness ($a_f < a_b$). Buckling, delamination, and film failure correspond to the domains above the dotted red line $a_b(|\sigma_m|)$, to the vertical green arrows, and the hatched blue domain, respectively. Film cracking is avoided if the system remains in a state located below the solid line in this representation.

4.5.5 Comparisons of the Various Length Scales of the Problem and Criterion for Film Failure

In the preceding paragraphs, the criteria for film buckling, extension of the debonded zone, and transverse failure of the film were expressed in terms of debonded zone size. In these three cases, it was possible to define a critical size above which the process is expected to occur. For the specific case of propagation of the delamination front, our analysis showed that above a critical length, the process will stop. These critical debonded sizes were shown to depend on the applied stress in the film, and their dependence on σ_m was explicitly given in Equations 4.10, 4.12, and 4.15.

To be able to predict in a simple way film failure during layer transfer, these three criteria are represented on a same graph in Figure 4.5 where the compressive stress $|\sigma_m|$ in the film is given along the abscissa and the half-length a of the debonded zone is given along the ordinate. In this representation, the state of the system at a given time corresponds to the point $(|\sigma_m|, a)$. For each process studied, i.e., buckling, delamination, and film failure, the space $(|\sigma_m|, a)$ can be divided into two distinct regions, separated by the curves $a_b(|\sigma_m|)$, $\{a_p(|\sigma_m|), a_a(|\sigma_m|)\}$, and $a_f(|\sigma_m|)$. If the system, characterized by its coordinates $(|\sigma_m|, a)$ is in the region defined for a given process, then this process will occur, while if the system corresponds to a point lower than the critical curve defined for the phenomenon, one does not expect this process to occur. Therefore, this relatively simple representation can be used to follow the temporal evolution of the layered specimen.

Such diagrams are represented in Figure 4.5 where the critical defect length $a_b(|\sigma_m|)$ for buckling, $a_p(|\sigma_m|)$ and $a_a(|\sigma_m|)$ for propagation and arrest of the delamination front, and $a_f(|\sigma_m|)$ for film failure are plotted. The relative position of the curves defining the domain for buckling and delamination is robust and independent of the specific value of the parameters of the problem. In particular, the critical length for buckling a_b is always smaller than the critical length for interfacial crack propagation a_p , and in the limit of large compressive stress, $a_b \simeq a_p$. However, the position of the domain corresponding to film failure with respect to these curves may change with the value of the parameters. For illustrative purposes, two cases have been considered: on Figure 4.5(a), the critical length for failure a_f is larger than those at buckling a_b and delamination a_p . This corresponds to thick films and/or a highly resistant films. The other system, corresponding to Figure 4.5(b), is for thin films and/or films with little resistance to cracking and/or films with a large critical radius of curvature R_c at failure.

In both diagrams, the hatched zone corresponds to states of the system where the film is

broken. Propagation of the interfacial crack, and thus the extent of the debonded zone, is indicated by vertical arrows.

We first consider the case of a highly resistant film with a small thickness Figure 4.5(a). Whatever the initial size a_{ini} of the largest defects at the bonding interface, one can follow the evolution of the system during the layer transfer process. For example, let us take an initial defect with size a_{del} . During layer transfer, the temperature is increased and as a result, the stress $|\sigma_m|$ in the film also increases according to Equation 4.1. At the start of the process, the system evolution is represented by a horizontal line because the debonded zone remains unchanged. When the system reached the line $a_b(|\sigma_m|)$ demarcating the flat film and the film buckling, this zone starts to buckle but a still remains constant, so the specimen evolution can still be represented by a horizontal line. When the system reaches the line $a_p(|\sigma_m|)$, demarcating the stable buckled film and the propagation of the interfacial crack, there is delamination of the film and a increases. Therefore, a vertical line now describes the evolution of the film geometry. Two cases are then possible: (i) if the initial defect was sufficiently small ($a < a_1$), the extension of the buckled domain leads to film failure. In this case, the trajectory of the system in this representation reaches the border of the hatched zone. Here, the critical debonded zone size before the appearance of transverse cracks is provided by $a_p(|\sigma_m| \geq \sigma_1)$ (represented as a solid line); (ii) the crack stops before film failure, leading to a debonded zone of size a_a which is smaller than the critical length for failure a_f . The system will fail only if the temperature is increased again, resulting in a quasistatic propagation of the delamination crack with half-length a_a . Transverse cracks will eventually initiate if the compressive stress is sufficiently high so that $a_a(|\sigma_m|)$ reaches the critical size for failure a_f . In this case, the critical compressive stress σ_1 for film cracking is given by $a_a(\sigma_1) = a_f(\sigma_1) = a_2$. Defining $a_1 = a_p(\sigma_1)$, one arrives at the following variations in the maximum admissible compressive stress σ_c with the initial defect size:

- (i) For $a_{ini} < a_1$, one gets $\sigma_c = a_p^{-1}(a_{ini})$, where $a_p(\sigma)$ is provided by Equation 4.12;
- (ii) For $a_1 < a_{ini} < a_2$, one gets $\sigma_c = \sigma_1$;
- (iii) For $a_2 < a_{ini} < a_l$, one gets $\sigma_c = a_f^{-1}(a_{ini})$, where $a_f(\sigma)$ is provided by Equation 4.15;
- (iv) For $a_l < a_{ini}$, one gets $\sigma_c = \sigma_l$ given in Equation 4.16.

Let us now focus on the case of films with large thicknesses and/or low resistance to failure. From the analysis of the corresponding diagram presented in Figure 4.5(b), two cases can be isolated:

(i) for initial defects smaller than $a_3 = a_b(\sigma_l)$, the film remains intact as long as the critical stress for buckling is not reached. At this threshold, the debonded zone starts to buckle and a transverse crack appears at the same time. This means that the critical stress σ_c for film failure is provided by the expression for the buckling stress of a debonded zone of size a_{ini} that can be derived from Equation 4.10; (ii) for larger initial defects $a_{ini} > a_3$, the film first buckles and then breaks when the compressive stress reaches the critical stress for failure σ_c . This leads us to conclude that:

(i) for $a_{ini} < a_3$, one gets $\sigma_c = \frac{\pi^2}{12} \frac{E}{1-\nu^2} \left(\frac{h}{a_{ini}} \right)^2$;

(ii) for $a_3 < a_{ini}$, one gets $\sigma_c = \sigma_l$ given in Equation 4.16.

It is interesting to note that in the limit of very small defects $a \ll a_{del}$, both kinds of systems, represented by two rather different diagrams lead to the same expression for the critical compressive stress for film cracking. Using the approximation $a_b \simeq a_p$ valid for large compressive stress, one gets in both cases $\sigma_c \simeq \frac{\pi^2}{12} \frac{E}{1-\nu^2} \left(\frac{h}{a_{ini}} \right)^2$. The same remark is also valid in the limit of large defects for which $\sigma_c = \sigma_l = \frac{E}{2\sqrt{3(1-\nu^2)}} \frac{h}{R_c}$.

This analysis provides an upper limit σ_c to the compressive stress that can be imposed on the film. Conversely using Equation 4.1, the maximum layer transfer temperature to which the system can be exposed to avoid failure can be also predicted. With the result obtained in Section 4.4 from the stability analysis of microcracks leading to film splitting, one gets a range of admissible stress $-\sigma_c < \sigma_m < 0$ for the system during the layer transfer process, each limit corresponding to distinct failure modes. The theoretical predictions are compared with experimental observations in Section 4.6.

4.6 Discussion and Comparison with Experimental Results

To determine to what extent the previous analysis applies to experimental situations, two kinds of experiments for which transverse cracks in the film were observed have been analyzed. Each one corresponds to one failure mechanism analyzed in the previous sections. The first experiment is devoted to the study of the stability of microcracks in the film and analyzes the effect of the tensile/compressive state of stress on their trajectory. The second experiment has been designed to study the effect of large compressive stresses on the film.

4.6.1 Effect of the Compressive/Tensile State of the Stress on the Stability of Cracks

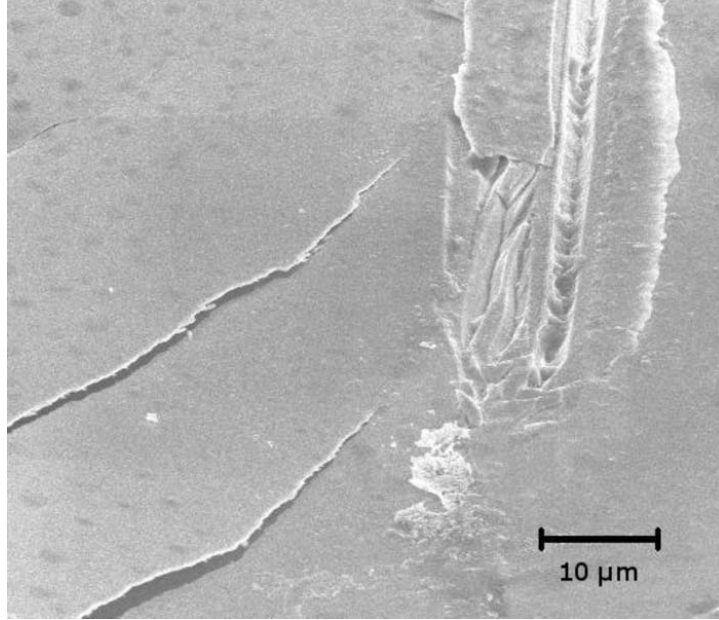


Figure 4.6. SEM image of the top surface of an ion implanted LiNbO_3 sample after heating without being bonded to a substrate. Transverse cracks can be seen coming from the implanted region in the LiNbO_3 , through the thin film, and emerging on the top surface of the sample.

For the first experiment, a sample of lithium niobate (LiNbO_3) was implanted with hydrogen and helium to a depth of $h = 400$ nm below the top surface. The specimen was heated and no bonding was involved. In this case, a coherent thin film of LiNbO_3 is not separated from the rest of the material; rather, the cracks that initiated at the plane of implantation immediately deviate from a horizontal trajectory and finally emerge at the top surface of the sample Figure 4.6.

To explain these results, we assess the effect of the absence of substrate on the stress state in the LiNbO_3 specimen: the stress σ_m remains equal to zero even during the heating phase. Therefore, the cracks initiating from the implanted plane are unstable and as discussed in Section 4.4, they are expected to deviate from a horizontal trajectory. This observation is in agreement with the condition $\sigma_m < 0$ that was proposed in Section 4.4 to ensure successful layer transfer.

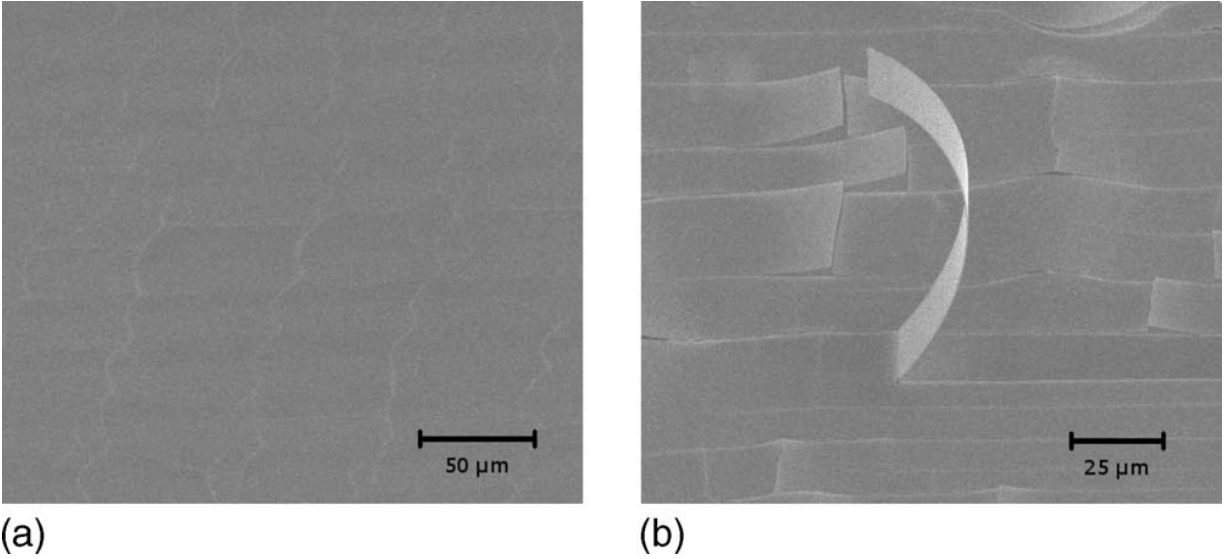


Figure 4.7. SEM image of the free surface of the transferred thin film. (a) One can see a network of parallel fractures with telephone-cord-like cracks which are characteristic of buckling instabilities; (b) one can observe the network of secondary cracks perpendicular to the wavy cracks, also produced by buckling and failure of the film.

4.6.2 Effect of a High Compressive Stress on the Film

The second experiment was performed on a system whose geometry corresponds to that represented in Figure 4.1. The crystal to be transferred is again ion implanted LiNbO₃ with $h = 400$ nm. The LiNbO₃ and silicon (Si) substrate were bonded together with minimal pressure and a silver bonding layer which will be discussed in Chapter 5 [32]. The substrate, the bonding layer, and the LiNbO₃ specimen have square bases with sides of 1 cm. The thickness of the substrate and the bonding layer are 1 mm and 800 nm, respectively. The system is then heated up to 750 K so that $\Delta K \simeq 450$ K, leading to a compressive stress in the film from the mismatch in thermal expansion coefficients, α_{LiNbO_3} being larger than α_{Si} . In this case, layer transfer of the LiNbO₃ specimen is obtained. This demonstrates that the compressive stress induced by the bonding of LiNbO₃ onto a substrate with a smaller thermal expansion coefficient has enabled crack propagation along the plane of implantation. This agrees with the predictions of Section 4.4. SEM images of the transferred LiNbO₃ thin film indicate the presence of transverse cracks that have cut the film in various pieces Figure 4.7. One can see that these transverse cracks are all oriented in the same direction. This might correspond to the direction normal to the one of maximum thermal expansion within the

LiNbO_3 ⁶. Also, these cracks follow a wavy trajectory, also referred to as “telephone-cord-like” patterns, characteristic of thin film buckling [28, 91]. This is strong evidence in support of the predictions of Section 4.5: at first, the thin film buckles from a highly compressive stress, resulting in a network of buckling zones with a characteristic wavy geometry. Then, failure occurs by bending of the film where debonding has occurred. This leads to transverse cracking in the film with the same wavy structure as the buckling.

An additional observation suggests that the transverse cracks observed in the film do not come from the deviation of microcracks which initiate at the plane of ion implantation, but result from buckling, delamination, and then failure of the film. The study of the other part of the sample (LiNbO_3) that has been separated from the rest of the layered structure does not reveal any cracks on the freshly created surface. In other words, the interface between film and substrate plays a crucial role in the initiation of these undesirable cracks, while ion implantation leads to a controlled splitting of the film when bonded to a substrate with a smaller thermal expansion coefficient. This observation also suggests that a controlled splitting of the LiNbO_3 single crystal is not enough to obtain a defect-free thin film, and the formation of transverse cracks by processes after layer transfer is also possible, as shown in Section 4.5.

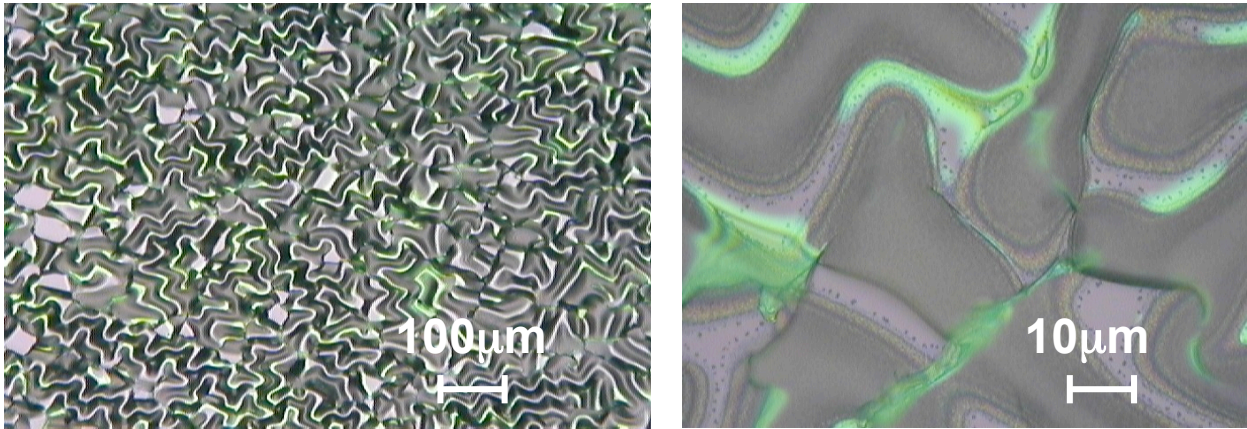


Figure 4.8. The left and right panels represent optical microscopy images of layer transferred LiNbO_3 under excessive compressive stress.

Another striking example of a film under excessive compressive stress is shown in Figure 4.8.

⁶The thermal expansion coefficients of the LiNbO_3 crystal are different along the various crystalline directions.

During the layer transfer process, this sample was in a state of compressive stress that enabled buckling of the film; however, the state of stress was not high enough to drive the buckled regions to the point of failure. This corresponds to the region of 4.5(a) between the red and a_b and a_f curves.

We now quantitatively compare the observations made in this experiment with the theoretical predictions made in Section 4.5. In order to estimate the compressive stress at failure in the LiNbO₃ film, Youngs modulus, and Poissons ratio of LiNbO₃ are taken to be $E = 150$ GPa and $\nu = 0.32$, close to the values measured for similar materials [51, 64]. The thermal expansion coefficients of Si and LiNbO₃ are $\alpha_{Si} = 2.6 \times 10^{-6} \text{ K}^{-1}$ and $\alpha_{LiNbO_3} = 8.2 \times 10^{-6} \text{ K}^{-1}$ [58], respectively, leading to $\Delta\alpha = -5.6 \times 10^{-6} \text{ K}^{-1}$. The critical radius of curvature for film failure under bending is estimated to be $R_c \simeq 1$ cm. Even though this value is a rather rough estimate, it is important to note that the shape of the curve a_f is rather insensitive to the value of R_c in the range of interest $|\sigma_m| > 0.1$ GPa⁷. Ceramic materials that are bonded to silver layers exhibit fracture energies on the order of $G_c \simeq 1 - 2 \text{ J m}^{-2}$. In the following, we have kept the fracture energy as a free parameter and chosen the value that enables the best agreement between experimental observations and theoretical predictions. The value so obtained is then compared with the expected values for ceramic-silver fracture energy.

Using the previous numerical values and Equation 4.1, it is possible to estimate the compressive stress $\sigma_{failure} \simeq 0.57$ GPa in the film at $T \simeq 750$ K for which undesired cracks appear. For the LiNbO₃/Ag/Si system studied here, one can also calculate the failure diagram to determine the state of the system with respect to $|\sigma_m|$ and a Figure 4.9. To reproduce correctly the experimental observations, one chooses $G_c \simeq 0.5 \text{ J m}^{-2}$ that is smaller but comparable to the expected values $G_c \simeq 1 - 2 \text{ J m}^{-2}$. The resulting diagram is analogous to Figure 4.5(a), which is plotted for the general case. The value of the compressive stress at $T \simeq 750$ K is also represented on this diagram as a vertical dashed line. It is now possible to identify the different processes that have led to the failure of the film. Using the representation of the system state shown in Figure 4.9, the initiation of the transverse cracks in the film is given by the intersection of the vertical dashed line giving the level of stress at film failure with the curve $a_f(|\sigma_m|)$. This line represents the boundary between intact and broken films. This provides a reasonable estimate $a \simeq 8 \mu\text{m}$ of the size for the defects at the interface between the silver bonding layer and the LiNbO₃ film that will ultimately lead to

⁷From the expression of a_f given in Equation 4.15, one can see that this length becomes independent of σ_m for large values of the stress in the film.

undesirable cracks in the film.

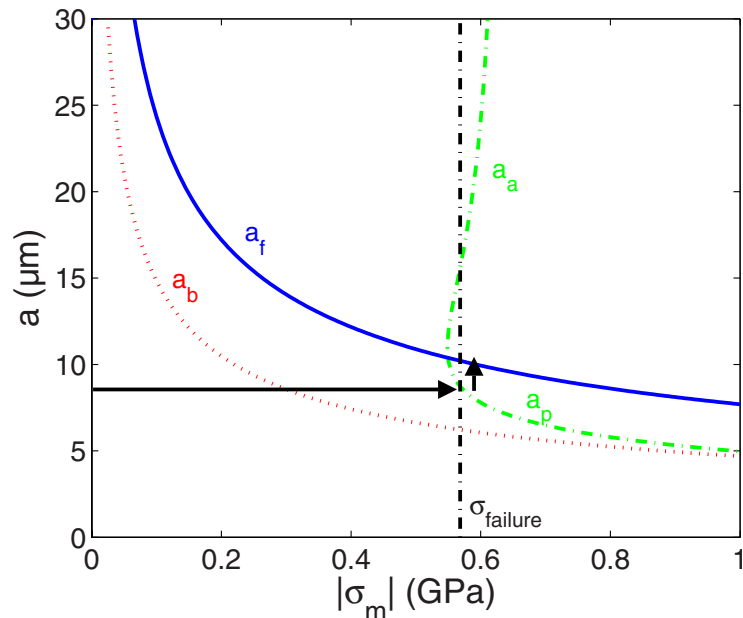


Figure 4.9. Diagram representing the evolution of the LiNbO₃/Ag/Si system during the later transfer process. The vertical line is the experimental compressive stress $\sigma_{failure} \simeq 0.57$ GPa in the film at failure, while the red dotted, green dashed, and blue solid curves correspond to the theoretically predicted critical values of the delaminated zone size for film bending, interfacial crack propagation/arrest, and film failure, respectively. The predicted evolution of the experimental system during layer transfer is represented by the black arrows.

From this diagram, one can also follow the temporal evolution of the film failure during the heating phase. The evolution of the system during the initial phase is described by the horizontal arrow represented in Figure 4.9. The defects at the interface between Ag and LiNbO₃ of size $a \simeq 8 \mu m$ will start to buckle for $\sigma_m \simeq 0.3$ GPa (corresponding to a temperature of $\simeq 540$ K). This value is given by the intersection of the horizontal arrow with the curve a_b . When the compressive stress in the film is sufficiently high, close to $\sigma_{failure}$, the interfacial cracks start to propagate. A network of debonded zones with a telephone-cord-like geometry then develops. This process will ultimately lead to the telephone-cord-like cracks observed postmortem on the thin film surface [Figure 4.7(a)] when the debonded zones start to extend in the transverse direction⁸. The evolution of the system

⁸This expansion of the debonded zone in two stages might be explained by a slight anisotropy of the thermal expansion coefficient of the LiNbO₃ single crystal. In the first stage, the compressive stress, larger along one of the crystallographic orientations of the LiNbO₃, produces an extension of the initial defects - converted into circular

in this last regime is described by the vertical arrow represented in Figure 4.9. Finally, failure of the film, which corresponds to the intersection of the vertical arrow with the curve a_f , is obtained for debonded zones with lateral dimensions on the order of $a \simeq 10 \mu m$. This is fully compatible with the postmortem observations made on the film surface after layer transfer.

4.7 Conclusion

In this chapter the origin of the undesirable cracking during layer transfer has been investigated. From our theoretical analysis based on fracture mechanics, it appears that the state of stress in the film, a direct consequence of the mismatch between the thermal expansion coefficients of the film and the substrate, drives the failure process. In addition, two phenomena identified in experimental tests are studied in detail and shown to induce catastrophic failure of thin films obtained by layer transfer: (i) the microcracks that propagate in the implanted plane parallel to the film/substrate interface and split the specimen can deviate from their horizontal trajectory and cut the film. The analysis of their stability in 3D shows that these microcracks will follow a straight crack path if the film is submitted to a compressive stress $\sigma_m < 0$; (ii) if the compressive stresses within the layer transferred thin film are above a critical value, the bonding and layer transfer process will fail. When the specimen is already cut but still heated, defects at the film-substrate interface can induce film buckling and delamination, ultimately resulting in film failure from bending. This process has been analyzed in detail, and the critical stresses (critical temperatures) at which each stage occurs have been expressed in term of defect size, film thickness and fracture properties of the film. Therefore, it is possible to predict the maximum compressive stress σ_c that can be sustained by the system. Taking into consideration both of these failure processes, one can define a range of acceptable stresses $-\sigma_c < \sigma_m < 0$ within the film.

From these results, it is now possible to identify the systems for which the layer transfer process will be successful. In particular, the the acceptable film stresses can be calculated in terms of the materials, bonding layers, and sample thicknesses being used. The substrate must be chosen so that its thermal expansion coefficient is smaller than that of the film. But this condition is not sufficient and above a critical temperature, which corresponds to a compressive stress σ_c , the transferred film will be cracked. This temperature must be lower than that necessary to make the debonded zones - into telephone-cord-like patterns that does not accompany an increase in the maximum curvature of the buckled zones. This is the case in the second stage characterized by a lateral expansion of these zones that produce film failure

microcracks propagate in the implanted plane of the film. To overcome this difficulty and increase the admissible stress in the film, the quality of the interface between film and substrate must be improved, decreasing both the defect size and increasing the interfacial fracture energy. One way to achieve a successfully transferred layer is by increasing the film thickness. A second alternative is to use a deformable plastic interlayer (e.g., Au, Ag, and Cu) which can increase bond strength and the chance of a successful bond. This is the focus of Chapter 5.

Chapter 5

Silver Diffusion Bonding and Layer Transfer of Lithium Niobate to Silicon

5.1 Introduction

In this chapter, we discuss a method of metallic bonding between two deposited silver layers. A diffusion bonding method has been developed that enables layer transfer of single crystal lithium niobate thin films onto silicon substrates. A silver film was deposited onto both the silicon and lithium niobate surfaces prior to bonding, and upon heating, a diffusion bond was formed. Transmission electron microscopy confirms the interface evolution via diffusion bonding which combines interfacial diffusion, power law creep and growth of (111) silver grains to replace the as-bonded interface by a single polycrystalline silver film. The layer transferred film, which was discussed in Chapters 3 and 5, had a composition that was the same as bulk lithium niobate. ¹

5.2 Wafer Bonding Limitations

Throughout the past two decades, wafer bonding has become an important electronics fabrication method [13, 114]. The ability to directly bond two materials, with varying lattice constants and crystal orientations, has facilitated the development of a wide range of research, from microelectromechanical systems to silicon-based photonics. Recently, wafer bonding processes have been combined with thin-film layer transfer induced by ion implantation. The combination of these two methods enables thin film single crystal layer transfer of a wide variety of semiconductors [14, 23, 48] and ferroelectrics [65, 87, 88]. By combining the flexibility of bottom-up processing with the near-ideal optical and electronic properties of single crystal films, these two techniques have become the standard method for producing silicon-on-insulator [23, 48]. In addition, wafer bonding and layer

¹This chapter is based on work done with Dr. Melissa Archer and Dr. Jennifer Dionne [32].

transfer has enabled ultra-high efficiency, multi-junction solar cells to be fabricated by bonding lattice-mismatched semiconductors.

A major challenge with current layer transfer processes concerns the thermal mismatch and preparation of the two bonding surfaces. Direct bonding, with no adhesion layer, is always challenging, and depending on the materials, can prove to be nearly impossible. Previous work with lithium niobate and silicon showed difficulty in bonding due to the fact that the coefficient of thermal expansion mismatch between the two samples was too great. One technique that was examined to address this problem was using laser-induced forward transfer techniques [88]. This technique minimized thermal expansion mismatch between the two bonding layers by inducing layer transfer using a carbon dioxide laser rather than traditional thermal cycling. In addition to thermal considerations, extensive work is required to ensure surface planarity, smoothness, and cleanliness of the two surfaces [9, 123, 129]; however, such processes are expensive and inefficient. Further, many of the methods used to produce bondable surfaces can ruin the implantation process and prevent a layer from being transferred. This problem could be circumvented with a reliable method for bonding two roughened or otherwise non-ideal surfaces.

The use of a metallic bond has been extensively developed for use in the 3D integrated circuit industry using copper and gold interconnects. Extensive research on copper bonding has been reported in dozens of publications by the group of Professor Reif at MIT as well as a wide range of other research departments [25, 26]. Besides gold and copper, another metal in the same category of materials is silver. Throughout this thesis and the literature, silver is used extensively in plasmonics research for its exceptional loss characteristics in regards to waveguides, resonators, and modulators [21, 35, 36, 109]. The development of a silver-silver diffusion bond which would allow single crystal active layers to be bonded to virtually any type of substrate significantly increases the flexibility of designing novel plasmonic structures. This design could also be extended towards the design of multi-layered MIM or other waveguiding structures which, without a robust and flexible metal bonding layer, might otherwise not be possible.

The rest of this chapter will focus on developing this new type of silver-silver bond which is used to improve the lithium niobate to silicon bond that was discussed in Chapter 4. Further, this type of bond is not limited to the two materials discussed here; rather, this technique allows single crystal thin films of a wide variety of materials to be transferred onto virtually any type of substrate. Finally, the experimental measurements done here indicate that the bonding mechanism which enables the silver-silver diffusion bond is similar to that seen in gold and copper.

5.3 Experimental Work

Polished, x-cut lithium niobate single crystal samples were obtained from MTI Corporation. Following the work done in Chapter 3, these samples were co-implanted with hydrogen to 6×10^{16} ions/cm² at 80 keV, followed by a 115 keV helium implantation with a dose of 5×10^{16} ions/cm². All implantations were done at room temperature. The lithium niobate and silicon (100) substrates were then sequentially sonicated in methanol, acetone, isopropanol, and deionized water. Silver was concurrently evaporated on both the implanted lithium niobate and silicon substrates (without removal of the silicon native oxide layer) to a thickness of 400 nm at $2.5 \text{ \AA}/s$. The roughness of the deposited silver was measured using atomic force microscopy, and the contamination of the silver surfaces before bonding was measured using X-ray photoelectron spectroscopy. The silvered surfaces were then bonded together at $500^\circ C$ for four hours in a nitrogen environment. The high temperature anneal caused the silver layers to bond together. Simultaneously, the anneal induced crack formation within the lithium niobate layer, following the formalism developed in Chapter 4, at the peak implantation depth. As a result, a layer of lithium niobate, whose thickness corresponds to the peak depth of ion implantation and whose area corresponded to the entire 1 cm^2 sample, was transferred to the silicon handle substrate.

Using a focused ion beam, transmission electron microscopy samples were extracted from both the bonded lithium niobate/silver/silicon sample and a silicon (100) substrate with 400 nm of silver evaporated on it under the same conditions as the bonded sample. Before milling, a $1 \text{ }\mu m$ thick platinum layer was locally deposited on the sample to prevent ion-induced lattice damage. The bonded structure was milled into on both sides of the TEM lamella and a U-shaped pattern was cut into the silicon to ease in the removal process, Figure 5.1(a). Using the focused ion beam, micro-tweezers were milled into a disposable tip within the FIB and the width of the micro-tweezers was milled such that they were the same size as the thicker portion of the lamella. The tweezers were then slid onto the thick portion of the lamella, Figure 5.1(b). After the lamella was secured with tweezers, the remaining portions of the U-cut were removed with the FIB and the lamella was able to be removed with the tweezers, Figure 5.1(c). After extraction, the thinner portion of the lamella was thinned from the size with deposited platinum to the point where the thin region of the lamella was 50 nm thick. This was done using gallium ions with an accelerating voltage of 30 keV. The samples were then characterized using a transmission electron microscope, which was operated at 300 keV.

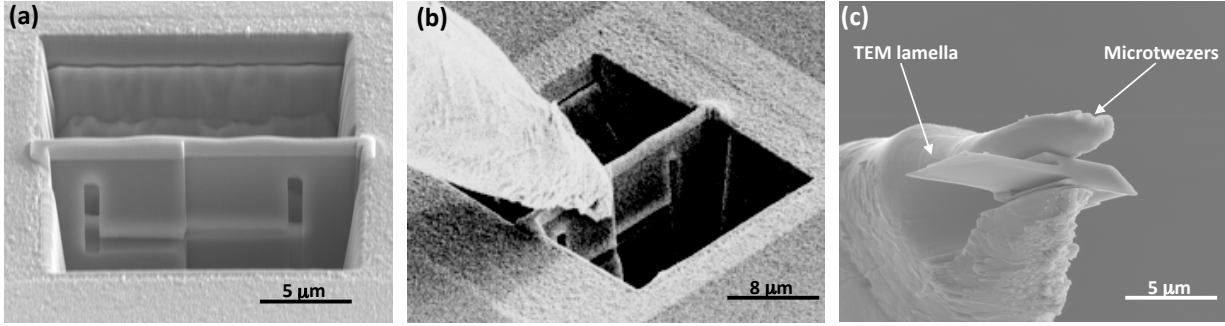


Figure 5.1. Removal of a sample for TEM using the FIB. (a) shows the initial milled structure before it's removed from the substrate. The lamella is then held using the micro-tweezers (b) and the rest of the lamella is released from the substrate. Finally, the FIB thins down the thinner portion of the lamella to 50 nm in preparation for TEM.

5.4 Analysis of Silver Diffusion Bonding

Figure 5.2(a) shows the lithium niobate sample with the silicon substrate at the bottom, the silver layer as the dark central region, the lithium niobate above it, and the 1 μm thick platinum layer in the top right section of the image. The silver layer, which appears as a dark band through the middle of the sample, appears to be continuous from one interface to the other and shows no sign of the original interface between the two silver layers. The lithium niobate layer is shown in detail in Figure 5.2(b). From this image, strain contrast from the bonding process can be seen at the interface between the transferred layer and the silver layer (bottom left). This can be attributed to the mismatch in the coefficients of thermal expansion between the silicon, silver, and x-cut lithium niobate layers (2.6×10^{-6} , 19.1×10^{-6} , and $8.2 \times 10^{-6} \text{ K}^{-1}$ respectively [58]). Through the center of the transferred film, a defect free single crystal region exists. This is seen in the selected area diffraction pattern shown as an inset, in which the crystal orientation corresponds with the x-cut orientation of the original lithium niobate sample. Above the single crystal region, a region of lattice damage remains as a result of the ion implantation and platinum deposition processes. To address this issue, we refer back to Chapter 3 which showed that a secondary annealing step, after the bonding step, can significantly remove any residual lattice damage from the layer transfer process and return the transferred layer to its original, single crystal state [87].

X-ray photoelectron spectroscopy confirmed the existence of a thin oxide layer on the surface of the deposited silver films before bonding and atomic force microscopy determined that the root-mean-squared roughness of that surface was $\sim 7.0 \text{ nm}$. Unlike gold which will start to form a

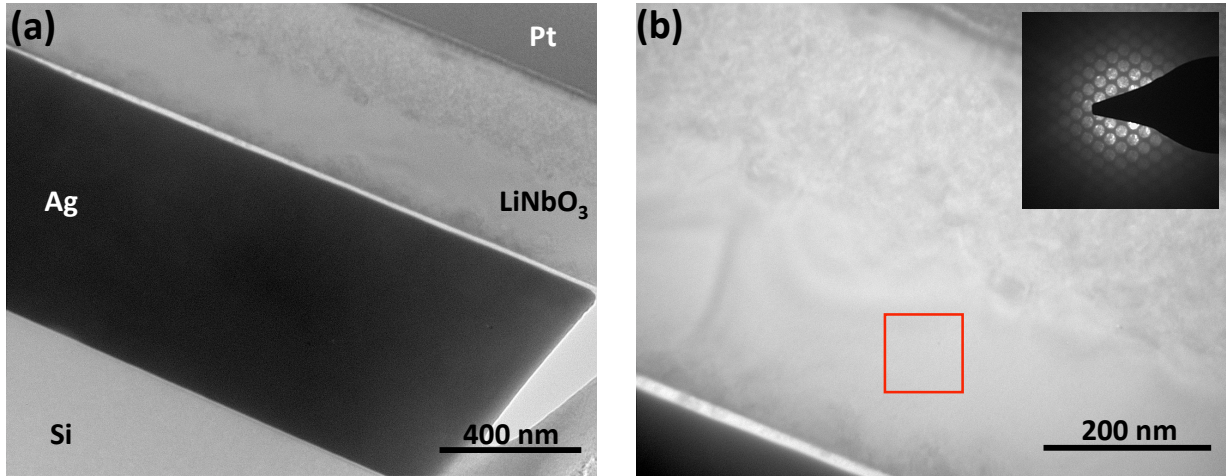


Figure 5.2. Transmission electron image of the extracted lamella, (a). From bottom to top the layers are: silicon, the bonded silver layer, lithium niobate, and the protective platinum layer. At higher magnification, the lithium niobate layer, (b), shows a strained interface, followed by a single crystalline region, and finally an amorphous damage region left over from the ion implantation. The diffraction pattern (inset) was taken in the region enclosed by the red box.

diffusion bond under pressure at room temperature, the silver oxide layer was sufficient to prevent bonding from occurring at room temperature. The samples were initially brought together at room temperature, such that the two silver films only contacted at the asperities of each silver surface. Upon heating to 500°C , the silver oxide layer became thermodynamically unstable [76, 77], and diffusion bonding took place. This process, which has been previously investigated for other materials systems by Derby and Wallach [29, 30, 47], consisted of an initial, rapid process of plastic deformation of the asperities of both silver films. Such deformation results in formation of a series of elliptical voids at the fractionally bonded interface. These voids are clearly visible in both scanning electron microscope and transmission electron microscope images, as shown in Figures 5.3(a) and (b) respectively.

After the initial stage of plastic deformation, the interfacial voids are removed during the remainder of the bonding process. Voids are removed through a combination of surface diffusion at the void/silver interface, bulk diffusion and grain growth, and power law creep [29, 30, 47]. All three mechanisms contribute to the removal of the bonding interface simultaneously, and the degree to which each mechanism contributes is determined by the bonding material, time, temperature, pressure, and initial surface conditions.

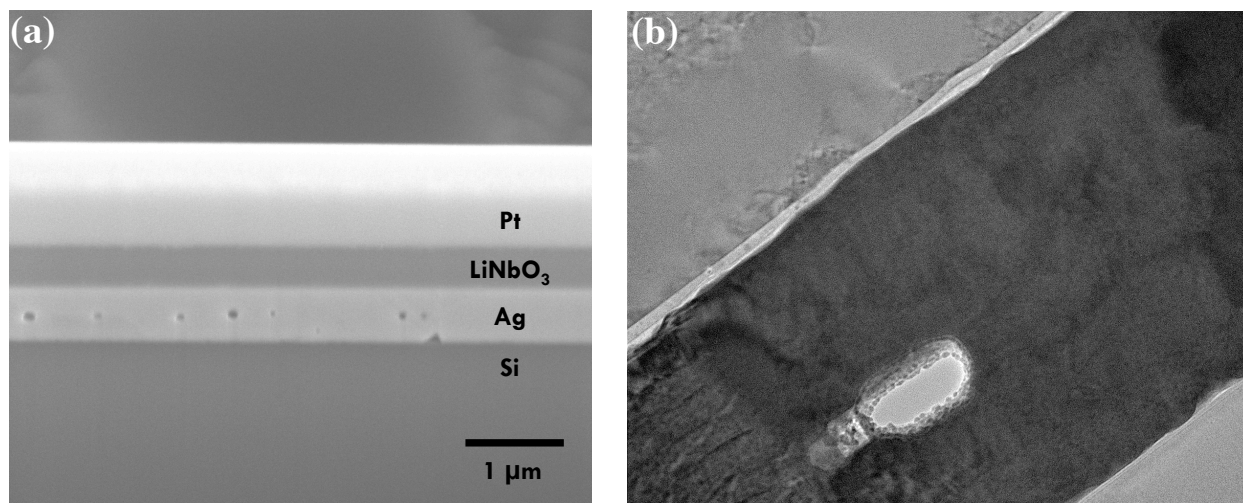


Figure 5.3. Scanning electron microscope image of the lithium niobate bonded to silicon with a silver bonding layer, (a). Ellipsoidal voids can be seen half way through the partially bonded silver layer. A transmission electron microscope image of one of the voids, (b), shows an intermediate stage between initial contact of the two silver layers and complete bonding, Figure 5.4(d).

During the bonding process, significant grain growth occurs through the bonding interface, as well as in the plane of the silver film. As opposed to imaging silver films with the SEM, when using the FIB to image silver, there is significant channeling of Ga^+ ions at the silver grain boundaries. As a result, imaging these surfaces with the focused ion beam produces a very clear image of the individual grains within a silver film. These images, before and after annealing, show that the average as-deposited grain size was 53 nm, whereas after the annealing the average grain size was 400 nm, as shown in Figures 5.4(a) and (b) respectively. X-ray diffraction analysis of identical samples of the silver films before and after the annealing process show that the grain growth observed is a result of preferential growth of silver (111) grains during the annealing process, Figure 5.5. Transmission electron microscope images of the silver layer before and after bonding are shown in Figures 5.4(c) and (d). The sample prior to bonding in Figure 5.4(c) exhibits multiple grains whose diameters are small enough that they do not extend throughout the thickness of the film. In contrast, grains extend across the original silver-silver interface after bonding, as shown in Figure 5.4(d). Three grains within the silver film extending from the silicon interface to the lithium niobate interface are shown. Note that the in-plane grain size in Figure 5.4(d) is also significantly larger than in 3(c). As in Figure 5.2(b), the interface between the two un-bonded silver layers is completely removed after bonding. Also, within each grain the film is single crystalline from the

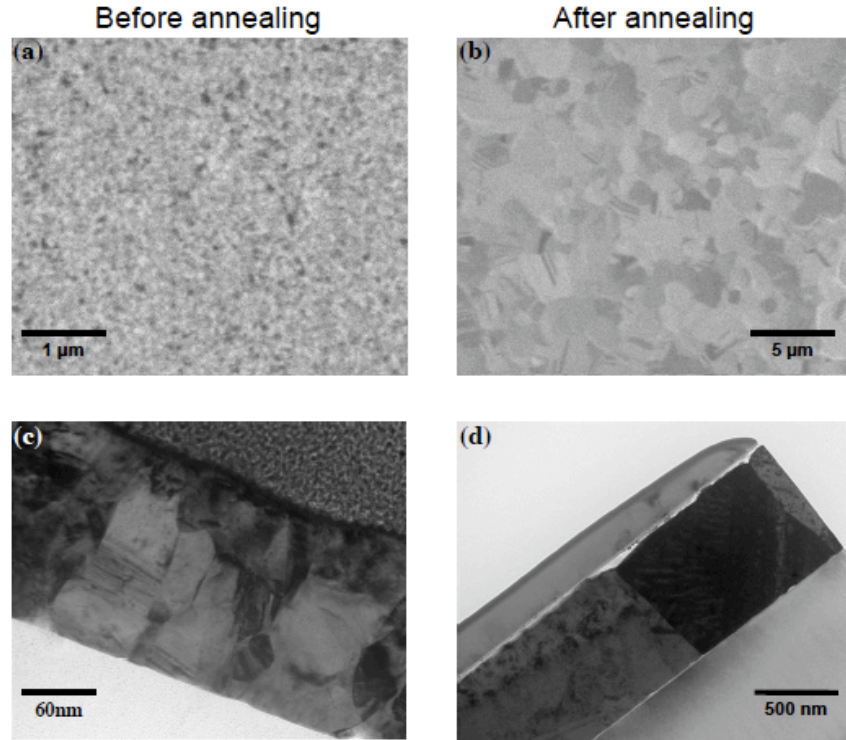


Figure 5.4. Focused ion beam images of the deposited silver films before and after annealing, (a) and (b) respectively. The average grain sizes were 53 nm in (a) and 400 nm in (b). Transmission electron microscope images of the silver layer before and after bonding, (c) and (d) respectively, show that grain growth during the annealing process has completely removed the interface between the original silver bonding layers.

silicon interface to the lithium niobate interface.

After the initial bonding process is complete, if further high temperature processing steps are required, the diffusion bonding process would continue based on the new time, temperature, and pressure conditions. Assuming the initial heating cycle produces a void-free bond, bonding would occur through a combination of bulk diffusion and grain growth, along with power law creep. This would further increase the size of the grains that extend from the silicon/silver interface to the lithium niobate/silver interface.

Finally, we note that the use of this method could generate deep level traps within the silicon substrate [50]. With a diffusivity on the order of 10^{15} cm²/s in silicon [78], certain device applications that are dependent on minority carrier lifetimes could be affected. For those devices where silver concentration within the silicon is a concern, a thin diffusion barrier could be deposited

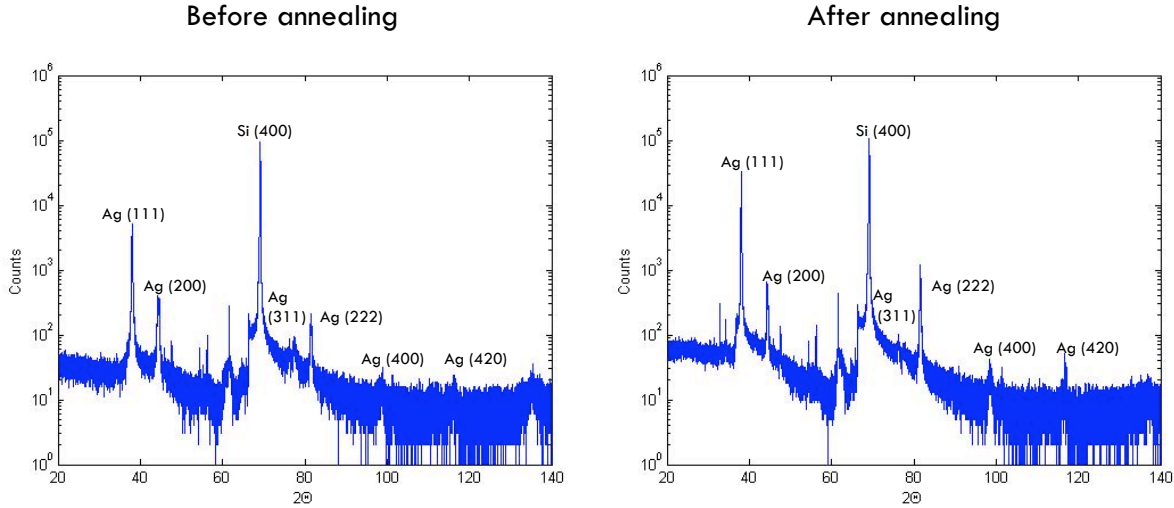


Figure 5.5. X-ray diffraction measurements of silver films before and after the annealing process associated with layer transfer. The growth of Ag (111) grains is one of the main mechanism is the formation of the silver bond.

between the silver and silicon [19]. Provided the processing temperature of such a device is kept below $500 - 600^{\circ}C$, these layers could be used to prevent adverse silver diffusion.

5.5 Conclusion

In this chapter we developed a new method of metallic bonding using two deposited silver layers. In combination with ion implantation-induced layer transfer, this technique has been demonstrated as a method for layer transfer of single crystal lithium niobate onto silicon substrates. This process, which can also be done with gold and copper, allows a wide variety of single crystal active layers to be bonded to virtually any type of substrate, and this technique increases the flexibility of designing novel plasmonic structures. We've shown that bonding between the two deposited silver layers occurred as a result of diffusion bonding which is similar to the processes that have been examined with gold and copper. Scanning electron microscopy and transmission electron microscopy images show that this process completely removed the bonding interface, and within individual grains, the silver was single crystalline from the lithium niobate/silver interface to the silicon/silver interface.

The combination of proper ion implantation (Chapter 3), with a proper choice of coefficient of thermal expansion matched materials (Chapter 4), and an improved bond strength using silver-silver diffusion bonding (Chapter 5), allows us to fabricate MIM waveguides with silver as the

cladding layers and lithium niobate as the active material. The results of this work are discussed in the following chapter.

Chapter 6

Tunable Color Filters Based on Metal-Insulator-Metal Resonators

6.1 Introduction

In this chapter, we discuss the culmination of Chapters 3, 4, and 5. We report a method for filtering white light into individual colors using metal-insulator-metal resonators.¹ The resonators are designed to support photonic modes at visible frequencies, and dispersion relations are developed for realistic experimental configurations. Experimental results indicate that passive Au/Si₃N₄/Ag resonators exhibit color filtering across the entire visible spectrum. Devices were fabricated using silver bonding and layer transferred lithium niobate as discussed in Chapter 5. Full field electromagnetic simulations were performed on active resonators for which the resonator length was varied from 1 - 3 μm and the output slit depth was systematically varied throughout the thickness of the dielectric layer. These resonators are shown to filter colors based on interference between the optical modes within the dielectric layer. By careful design of the output coupling, the resonator can selectively couple to intensity maxima of different photonic modes and, as a result, preferentially select any of the primary colors. We also illustrate how refractive index modulation in metal-insulator-metal resonators can yield actively tunable color filters. Simulations using lithium niobate as the dielectric layer and the top and bottom Ag layers as electrodes, indicate that the output color can be tuned over the visible spectrum with an applied field.

6.2 Color Filtering and Plasmonics

Color filtering is currently one of many areas where passive photonic [86] and plasmonic [17, 63, 117] devices are being explored for spectral imaging applications. The resonator geometry allows the output slit to be designed so as to preferentially couple out any of the supported optical modes.

¹This chapter is based on work done with Merrielle Spain.

In addition, because these resonators are on the order of 1 - 5 μm in length, they provide a unique opportunity to design color filters whose resolution and areal density are significantly higher than those currently available. In prototype designs for active plasmonic devices, electro-optic materials such as lithium niobate are being explored. Because lithium niobate has a large electro-optic coefficient, it is used extensively in surface acoustic wave devices and optical modulators [10, 42].

6.3 Metal-Insulator-Metal Color Filtering

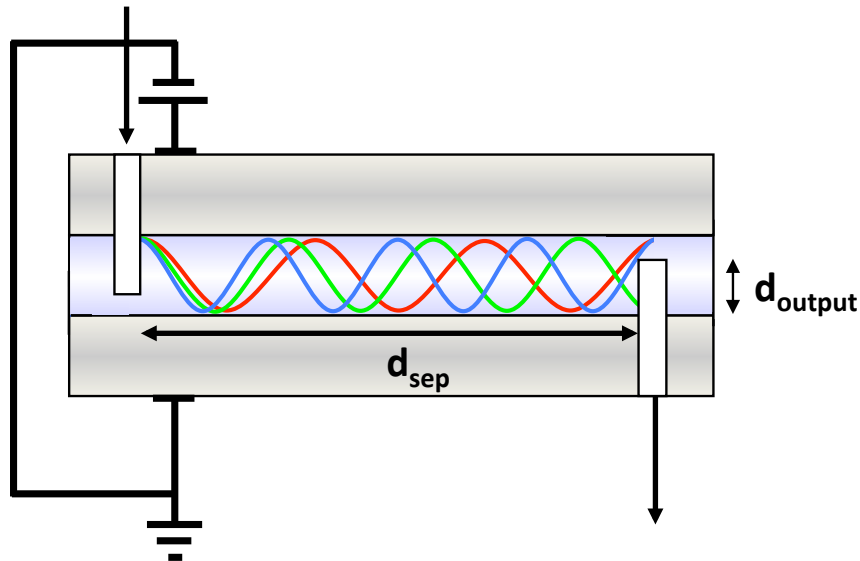


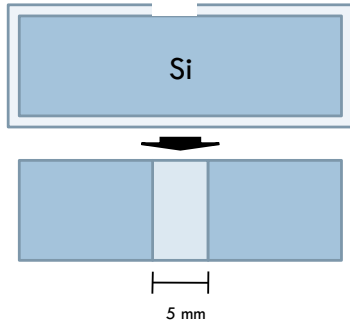
Figure 6.1. A schematic diagram of the MIM geometry used with input and output slits placed on the top and bottom of the waveguide. Depicted within the dielectric layer are the red, green, and blue longitudinal modes of the MIM waveguide.

A schematic diagram of the MIM resonator geometry used is shown in Figure 6.1. This structure has input and output slits milled into the top and bottom cladding layers respectively. The separation between the input and output slits is labeled “ d_{sep} ”, and the depth to which the output slit is etched into the lithium niobate is labeled “ d_{output} ”. For all simulations and experiments, plane wave white light illumination, in the wavelength range $\lambda = 400 - 700$ nm, is sent through the input slit, traverses the length of the optical cavity, and is detected after exiting the output slit.

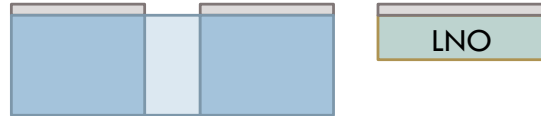
Free standing membranes of single crystal lithium niobate were fabricated using silver bonding and ion implantation induced layer transfer. By transferring a layer of lithium niobate onto a

silicon wafer with a cavity etched completely through the thickness of the wafer, membranes of this material were produced. In addition, strain and buckling normally induced during the layer transfer process, Chapter 4, will not affect these membrane layers because of the fact that there is no substrate to constrain the film. A diagram of this is shown in Figure 6.2.

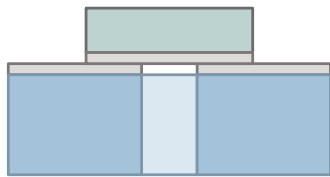
1. Si wafer waxed and etched through with acid solution



2. Silver evaporated onto LNO wafer and etched Si substrate



3. Wafers pressed against each other and bonded at high temperature



4. Ion implanted LNO splits to form thin film membrane over the hole

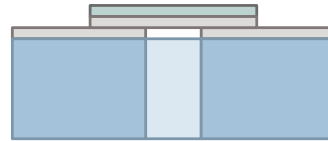


Figure 6.2. A schematic diagram of the lithium niobate membrane fabrication.

Optical microscopy images of a transferred lithium niobate membrane show an intact, layer transferred film, Figure 6.3(a). Small defects can be seen scattered across the surface of the membrane; however, these defects, as well as the roughness of the top surface of the transferred layer in general, can be removed through the use of chemical-mechanical polishing steps after the layer transfer process is complete. Once the membrane is formed and polished, a top layer of silver is deposited to produce the desired MIM membrane. To mill sub-wavelength input and output slit into the membrane, the FIB is used. These slits were milled through the silver layer and to varying depths within the lithium niobate layer. In addition to changing the depth to which the output slits were milled (d_{output}), the separation between the input and output slits (d_{sep}) was also varied. An example of this is shown in Figure 6.3(b).

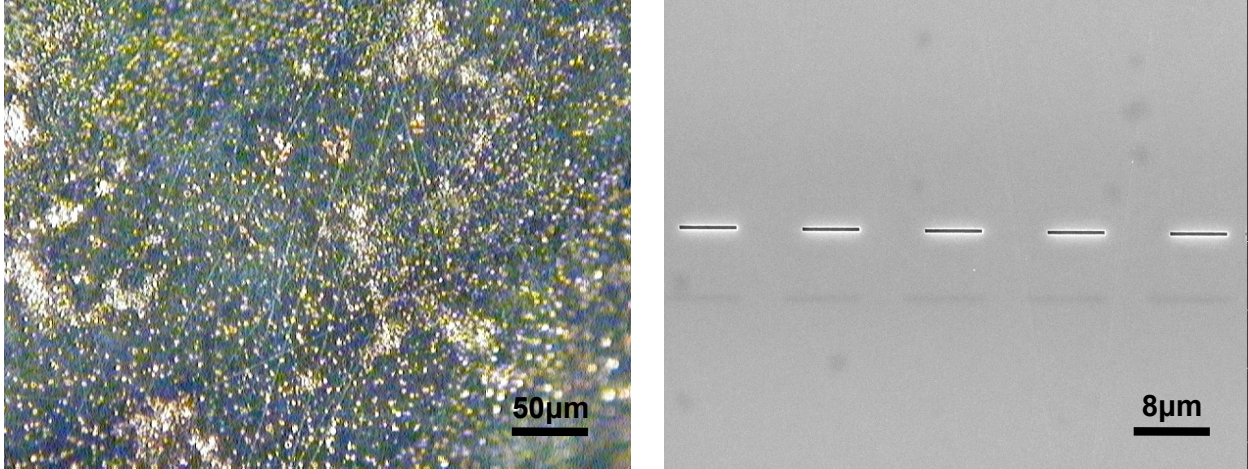


Figure 6.3. Layer transferred lithium niobate membranes using silver bonding, (a). A membrane of LiNbO_3 that has gone through FIB and is ready for measurements, (b).

6.3.1 Determining the Experimentally Observed Color

To calculate the color that a viewer would observe at the device output, the spectral sensitivity of the color sensitive cones within the human eye must be taken into account. To do this, the CIE (1964) color matching functions were used to correlate the chromatic response of the eye of a viewer over the visible range of the MIM output spectrum [2]. The red, green, and blue spectral sensitivity curves of the human eye are shown from 400 - 700 nm in Figure 6.4. The transmitted optical power spectrum through the output slit of each device was recorded. For finite-difference time domain simulations of these structures, the output power was normalized to the source power at each wavelength. The resulting color output was calculated by taking the inner product of each of the R, G, and B, color matching functions with the optical intensity from a specific device over the entire visible spectrum [8]. Then, color scales were developed that illustrated the output color seen by a viewer.

6.4 Results from Passive Silicon Nitride Color Filtering

Initial testing of these color filters was done with passive devices. Experimental measurements of these structures showed color filtering across the red, green, and blue regions of the visible spectrum. The devices shown in Figure 6.5(a) consist of a 500 nm silicon nitride freestanding membrane coated on top with 400 nm of gold and with 400nm of silver on the bottom side of

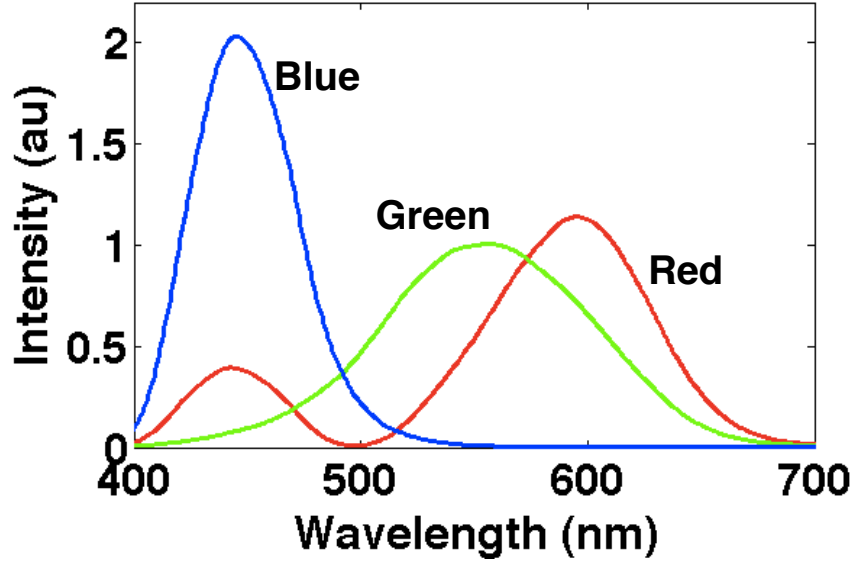


Figure 6.4. The 1964 CIE red, green, and blue color matching functions used in determining the output color from each MIM device.

the silicon nitride membrane. Input and output slits were defined by 20 keV Ga^+ focused beam in a focused ion beam lithography etching system. The devices were illuminated with a halogen white light source and colors were recorded by color imaging in an optical microscope with a 50x objective using a digital camera. In Figure 6.5(a) each device exhibits a different color at its output slit, and the colors shift across the entire visible spectrum as a function of the spacing between the input and output slits. Here the resonator length $d_{sep} = 2.5, 3.5,$ and $4 \mu\text{m}$ for devices 1 - 3 respectively, with a slit width of 400 nm. For all devices shown in Figure 6.5(a), the slit depths were $d_{input} = d_{output} = 250$ nm. The corresponding output spectra from these devices are shown in Figure 6.5(b). For each curve in Figure 6.5(b), the color used to plot the spectrum corresponds to the RGB value calculated using the method described in the previous section with each output spectrum shown in Figure 6.5(b). The fact that the calculated color from the device output spectrum is the same as the experimentally observed color confirms that the output spectrum were correctly converted into an equivalent observable color. The dispersion diagram for this structure is shown in Figure 6.6. These dispersion diagrams were calculated using a Nelder-Mead minimization of numerical solutions to Maxwell's equations [36]. Regions of the dispersion diagram that have a high photonic or plasmonic modal intensity appear darker (red and grey/black) and regions with little or no modal intensity appear lighter (green and blue). Figure

6.6 shows the existence of the plasmonic and three photonic modes across the visible spectrum.

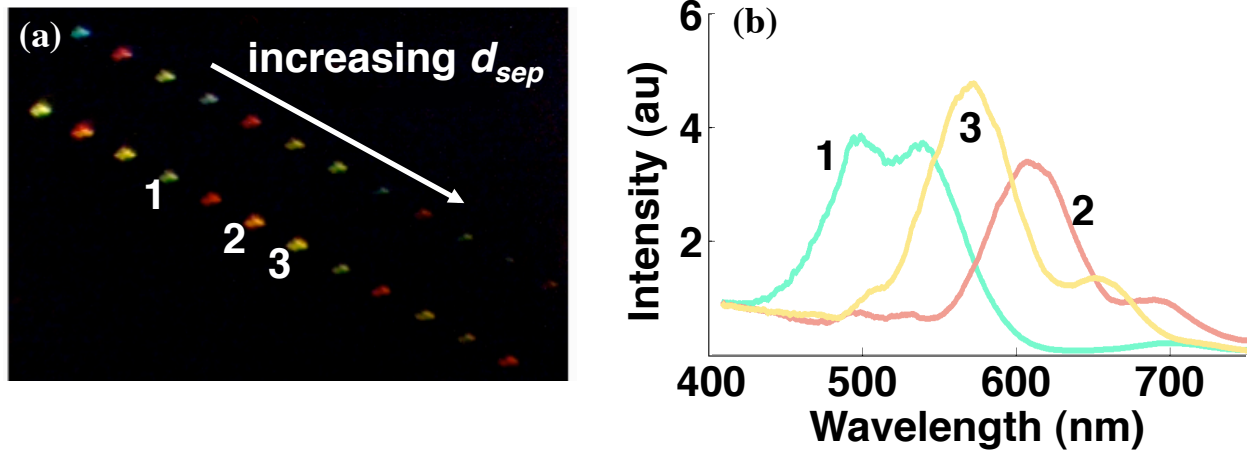


Figure 6.5. The 1964 CIE red, green, and blue color matching functions used in determining the output color from each MIM device.

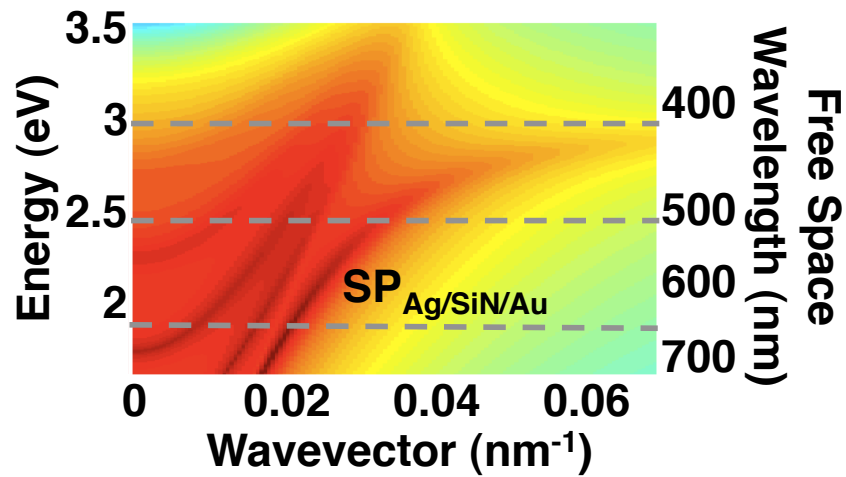


Figure 6.6. The dispersion diagram for these structures is plotted in (c), and shows one plasmonic and three photonic modes within the visible spectrum.

6.5 Modeling Active Color Filters

To study active color filtering, samples were measured experimentally with a halogen white light source and colors were recorded by color imaging in an optical microscope with a 50x objective using a digital camera. To model these devices, simulations were done using Lumerical, finite-difference time-domain software. The structures used in the simulations had 400 nm of silver on the top and bottom of the waveguide with 300 nm of lithium niobate as the dielectric layer. The devices were simulated under broadband transverse magnetic illumination from $\lambda = 400 - 700$ nm. All simulations were done with and without an applied electric field.

X-cut lithium niobate single crystal samples were obtained from the MTI Corporation. Using spectroscopic ellipsometry, the complex index of refraction of the lithium niobate was measured, and this data was used for all simulations. The top and bottom silver layers of the MIM waveguide were modeled using the materials parameters within the Lumerical materials database. The experimental lithium niobate data was fit from 400 - 700 nm as a Cauchy layer given by:

$$n(\lambda) = n_0 + C_0 \frac{n_1}{\lambda^2} + C_1 \frac{n_2}{\lambda^4} \quad (6.1)$$

$$k(\lambda) = k_0 + C_0 \frac{k_1}{\lambda^2} + C_1 \frac{k_2}{\lambda^4} \quad (6.2)$$

where $n_0 = 2.093$, $n_1 = 305.9$, $n_2 = 52.9$, $k_0 = 0.02$, $k_1 = 24.541$, $k_2 = 23.276$, $C_0 = 10^2$, $C_1 = 10^7$, and λ is given in nm. The reported coercive field for this material is ~ 4 kV/mm [3], and under an applied electric field greater than this, the lithium niobate was modeled as having a refractive index increase of ~ 0.12 across the visible spectrum, and the imaginary part of the index was kept the same as in the zero field case. This change in refractive index is consistent with domain switching in ferroelectric lithium niobate crystals [11]. The broadband indices of refraction that were used in these simulations are listed in Appendix D.

6.5.1 Varying the Output Coupling Separation

For all simulations involving lithium niobate, $d_{input} = 150$ nm. Simulations show that by holding d_{input} and d_{output} constant while varying d_{sep} , the intensity of the most efficiently out-coupled color oscillates as the output slit couples to either a maximum or minimum in the selected color's electric

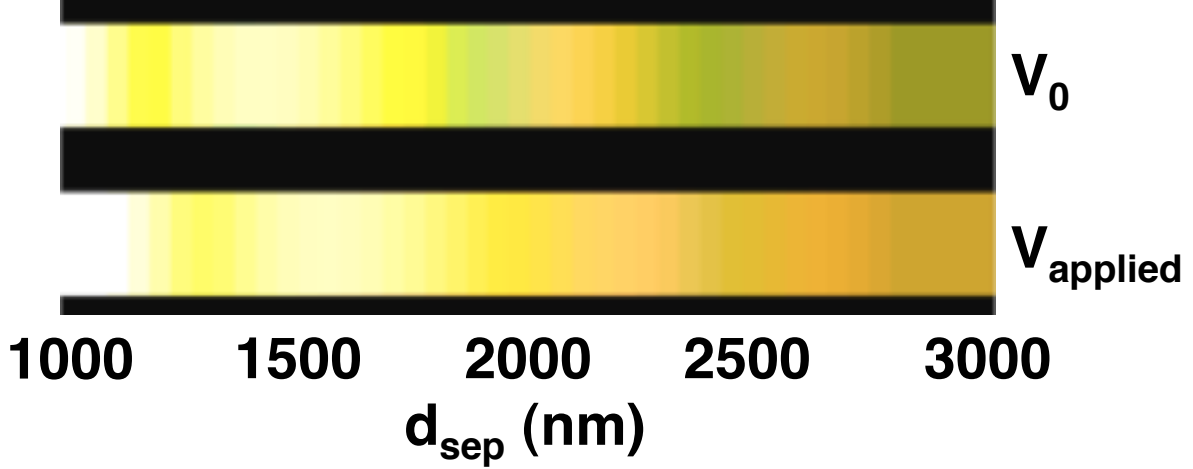


Figure 6.7. Output colors from MIM waveguides with $d_{input} = 150$ nm into the top half of the lithium niobate layer and $d_{output} = 260$ nm into the lithium niobate layer from the bottom of the structure. The output colors are plotted as a function of the spacing between the input and output slits. The bottom stripe of color is for devices under an applied field and the top stripe of color is for devices under no applied field.

field. Figure 6.7 shows the colors from devices with $d_{output} = 260$ nm and d_{sep} is varied from 1 - 3 μm in 50 nm steps. The top color stripe corresponds to devices under no applied electric field and the bottom color stripe corresponds to devices under an applied field. With no applied field, oscillations between the green and red modes can be seen. It can also be seen that when d_{sep} is such that the red mode is at a minimum, the green mode is most efficiently coupled through the output slit. Conversely, when the intensity of the red mode is a maximum, it is most efficiently coupled through the output slit and dominates the device transmission. By applying an electric field, the red mode dominates the device transmission and the resulting colors appear red-shifted.

Figure 6.8 shows the normalized power transmission through the devices from Figure 6.7. The top pane corresponds to transmission under no applied electric field and the bottom pane corresponds to transmission under an applied field. The transmission at three representative wavelengths of 450, 531.5, and 649.2 nm were selected from the entire visible spectrum and were plotted in blue, green, and red respectively. As was mentioned above, when d_{sep} is such that the red mode is at a minimum, the green mode is most efficiently coupled through the output slit. The lower transmission plot shows that with an applied field, the transmission of the green mode is suppressed with

respect to that of the red and blue modes. As a result, the dominant green oscillations that are seen in the top color stripe of Figure 6.7 are no longer present in the bottom color stripe.

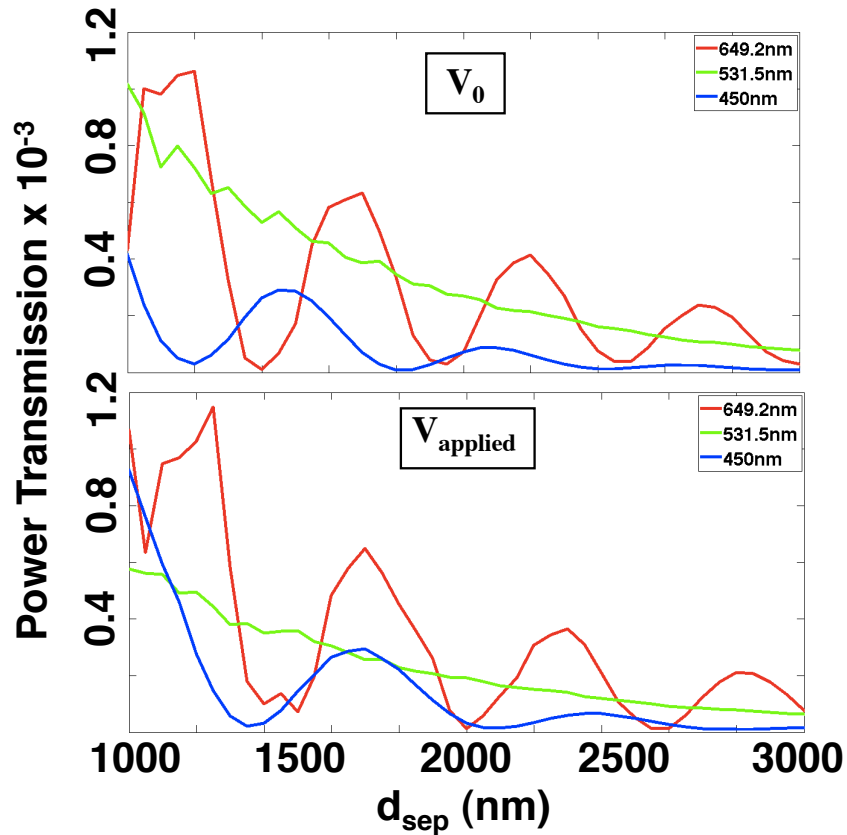


Figure 6.8. Power transmission through MIM waveguides with $d_{input} = 150$ nm into the top half of the lithium niobate layer and $d_{output} = 260$ nm into the lithium niobate layer from the bottom of the structure. The bottom plot is for devices under an applied field and the top is for devices under no applied field.

The source of the oscillations seen in Figure 6.8 is different for each of the three wavelengths sampled. For these MIM waveguides, the 200 nm wide output slit acts as a convolution function when it “samples” the optical modes by coupling them out of the device. The oscillations at 650 nm are from the slit coupling to maxima and minima of the mode as d_{sep} is varied from 1 - 3 μm . For the intensity at 530 nm, the “convolution length” of the slit is on the order of half the wavelength of the mode being sampled. As a result, there are small oscillations in the output intensity as d_{sep}

is varied; however, any major oscillations are damped out as a result of the slit width. Hence, the main shape of the green curve is simply determined by the decay of the mode as d_{sep} is increased. The oscillations of the blue curve result from beating between two modes propagating at 450 nm. Since this beating period is much larger than the actual period of either of the two modes involved, the oscillations can again be resolved by the 200 nm output slit.

Figure 6.8 also shows that for a given resonator, the transmitted power at a given wavelength is on the order of 0.05%; however, this metric is best suited for devices that transmit a single or narrow band of wavelengths. In the case of these MIM color filters, the resonators pass a broadband spectrum. When this intensity spectrum is integrated with the RGB color matching functions over the entire visible spectrum, the total amount of transmitted power is significantly increased. Ongoing work is focused on optimizing the design of the input and output slits to increase the total amount of transmitted power; however, initial results indicate that the total broadband transmitted power can be increased by at least an order of magnitude. This is discussed in Section 6.7.

6.5.2 Varying the Output Coupling Depth

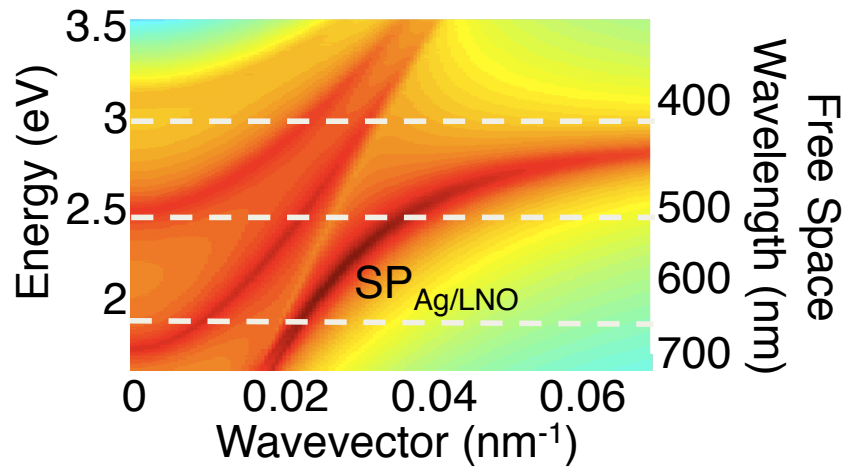


Figure 6.9. The dispersion diagram for the MIM structure with 300 nm of lithium niobate between two, 400 nm layers of silver.

Modeling the dispersion of the MIM waveguides shows the existence of the plasmonic and three photonic modes, as illustrated in Figure 6.9, which is a plot of the frequency dependence of the real

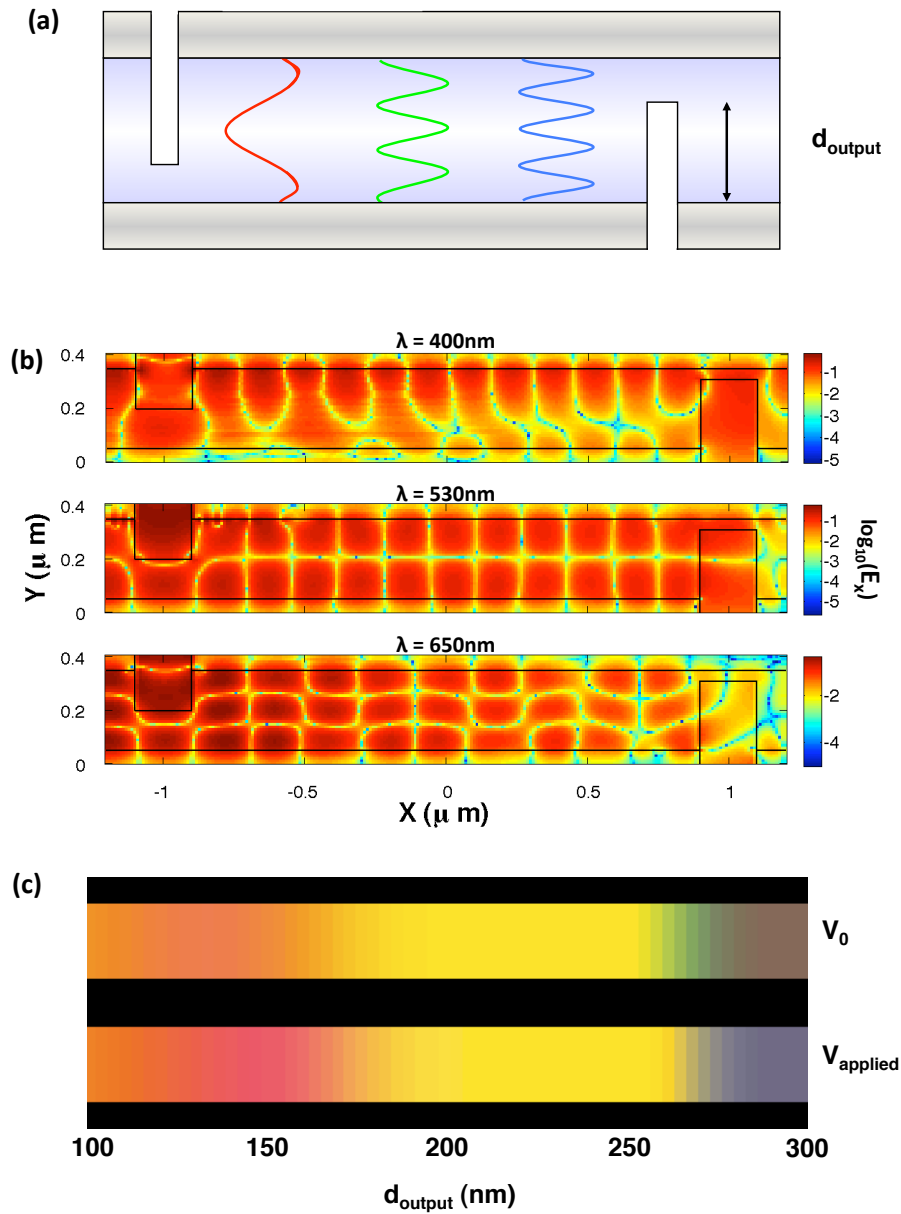


Figure 6.10. Mode profiles for the red, green, and blue photonic modes (a). Full field electromagnetic simulations of the entire waveguide at $\lambda = 400$, 530 , and 650 nm are shown in (b). The resulting output colors from a MIM waveguide with an input-output slit spacing of 2000 nm are shown in (c). The top stripe of color is for devices under no applied field and the bottom stripe is for devices under an applied field.

part of the wavevector. For a lithium niobate layer 300 nm thick, the dispersion calculations show that the structure’s three photonic modes lie in the regions 1.9, 2.5, and 3 eV, which correspond to the red, green, and blue regions of the visible spectrum respectively. Figure 6.10(a) shows the red, green and blue photonic mode profiles moving through the MIM waveguide. Not shown here is the mode profile of either the symmetric or anti-symmetric plasmon modes. Full field electromagnetic simulations of these structures show the electric field distribution throughout the entire waveguide, Figure 6.10(b). The three field profiles shown here are plotted at $\lambda = 400, 530,$ and 650 nm. These plots correspond to the three modes shown in Figure 6.10(a) and 6.9.

The MIM waveguides modeled in Figure 6.10(c) had a constant $d_{sep} = 2000$ nm for all devices, with and without an applied electric field. For these simulations, d_{output} was increased from 100 - 300 nm into the lithium niobate, in 2 nm increments from one colored panel to another in Figure 6.10(c). By simply varying the depth of the output slit into the lithium niobate layer, one can preferentially couple to the different photonic modes and output any of the primary colors. In Figure 6.10(c), the top color stripe corresponds to no applied electric field and the bottom color stripe corresponds to devices under an applied field. For these specific devices, the output slit most efficiently couples to the red mode with and without an applied electric field for slit depths below ~ 150 nm. With no applied electric field, the output slit most efficiently couples to the green mode between 250 nm and 275 nm, and with an applied field, the output slit most efficiently couples to the blue mode above ~ 285 nm.

6.6 Losses

As we saw in Figure 6.8, losses within MIM waveguides are substantial. These losses can be broken down into two categories: cavity losses and slit losses. For a lithium niobate MIM waveguide with $d_{sep} = 1 \mu m$, calculations show that there is 7.53 dB of loss at the input slit, 5.85 dB of loss through the lithium niobate, and 5.68 dB of loss through the output slit. Hence, while these devices enable extremely high modal confinement, the losses are currently such that their use as long range waveguides is challenging.

For MIM waveguides where the dielectric thickness is below cutoff for all of the photonic-like modes, the only modes supported are the symmetric and anti-symmetric plasmon modes [71]. In this case, a significant amount of the electric field of these “bound” modes resides in the metal. As a result, there is usually a tradeoff between confinement and loss. In a MIM structure, these losses

are a result of both ohmic losses within the metal as well as field interference from phase shifts induced by the metal between the two metal-dielectric interfaces within the waveguide [37]. As the thickness of the dielectric layer is increased beyond the photonic cutoff thickness, an increasing amount of the light resides within the photonic-like modes whose losses are dominated by the intrinsic losses of the dielectric.

The other source of loss within these waveguides is slit losses. From a single slit, coupling into and out of these devices introduces $\sim 5 - 7$ dB of loss. For shorter devices, these losses dominate the overall transmittance. As a result, recent work has focused on improving the amount of light that can be sent through individual slits while still coupling efficiently to the various photonic and plasmonic modes that are supported.

6.7 Increasing Slit Transmission

To increase the amount of light transmitted through these color filters, the design of the input and output slits was studied in a variety of geometries. Initial studies focused on both trapezoid shaped input/output slits as well as a trapezoid/rectangle hybrid design in which the portion of the slit milled into the metal cladding layer of the waveguide was trapezoid in shape and upon reaching the lithium niobate, the slit was milled as a rectangle (with vertical sidewalls).

For both trapezoidal and hybrid designs, all input/output slit separations were $2 \mu m$, and all slits were milled half way into the lithium niobate. Also, the width of both the bottom and top of the slits was varied while any given dimension was the same for both the input and output slits. Figure 6.11(a) shows the trapezoidal input and output slit designs. Figure 6.11(b) shows the total integrated power transmitted through the waveguide, normalized to the source, for (a) as a function of slit dimensions. The x-axis represents the width of the trapezoid where it is terminated within the lithium niobate, and the colors of the lines (shown in the legend) represent the width of the trapezoid where it is terminated at the silver/air interface. The green dots represent trapezoids where the top and bottom dimensions are the same, i.e. the slits are rectangles. For comparison, the red “*” represents the standard, 200 nm wide slits that were used throughout this Chapter.

Figure 6.12(a) shows the hybrid input and output slit designs. Figure 6.12(b) shows the total integrated power transmitted through the waveguide, normalized to the source, for (a) as a function of slit dimensions. The x-axis represents the width of the rectangular portion of the slit that is milled into the lithium niobate and the colors of the lines (shown in the legend) represent the width

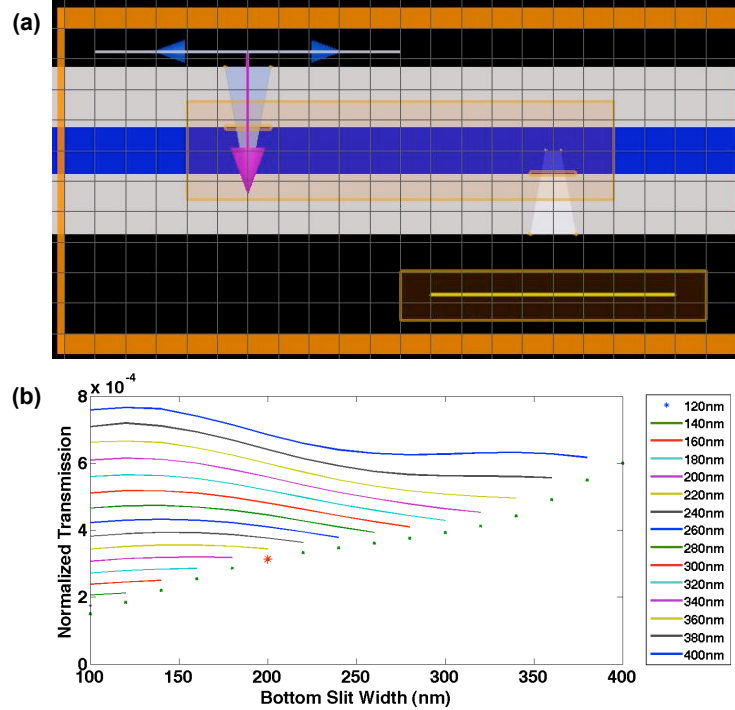


Figure 6.11. Schematic of the trapezoid slit design and FDTD simulations, (a). Transmission through the device as a function of bottom slit dimension (x-axis) and top slit dimension (legend).

of the trapezoid where it is terminated at the silver/air interface. As was the case in Figure 6.11(b), the green dots represent rectangular slits with the specified dimensions and the red “*” represents the standard, 200 nm wide slits that were used throughout this Chapter.

Even in these initial studies which vary the shape and dimensions of the input and output slits, Figures 6.11 and 6.12 both show that the amount of transmitted light through these devices can be significantly (sometimes at least an order of magnitude) increased by a simple optimization. It should be noted that this simple, first-order study of slit geometries does not optimize the slits to provide the most distinct colors or most efficiently couple into all the different optical modes that the cavity supports. For simplicity, all the dimensions of the input and output slits were exactly the same in all simulations; however, future work will focus on varying these parameters independently to better optimize the devices for a given application.

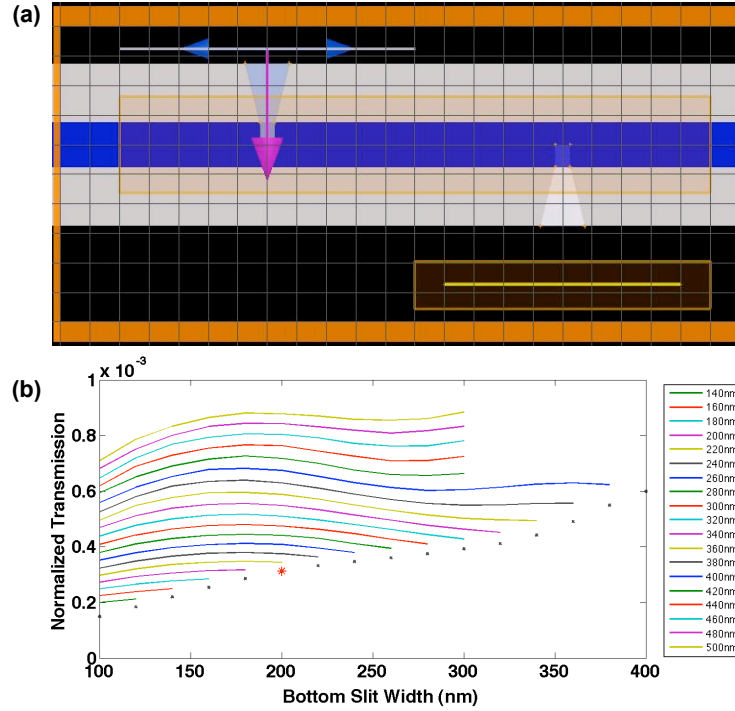


Figure 6.12. Schematic of the trapezoid/rectangle hybrid slit design and FDTD simulations, (a). Transmission through the device as a function of bottom slit dimension (x-axis) and top slit dimension (legend).

6.8 High Density Color Filtering Design

To further increase the total amount of light transmitted through the waveguides, the design scheme presented here could be easily integrated into a high density array of metal-insulator-metal resonator color filters. By fabricating two output slits equally spaced on either side of an input slit, one could double the total amount of transmitted light. By close packing three of these structures together with three input slits, each rotated by $\pm 120^\circ$ with respect to the other two, a hexagonal “MIM pixel” could be produced. A cross-section of such a device is shown in Figure 6.13(a). The top pane represents the output slits of the device and the bottom pane shows the input slits. The largest dimension of such a pixel would be $\sim 3 - 5 \mu\text{m}$. At present, this is 1 – 2 orders of magnitude smaller than the best high-definition color filters currently available [67]. Thus, these devices provide $\sim 0.05\%$ transmittance through an individual device is two to three orders of magnitude lower than traditional LCD color filters, the density of these devices in a two-dimensional array is two to three orders of magnitude higher than traditional LCD color filters. If instead of high resolution, a higher transmission is required, the hexagonal pixels could be tiled together to form

“superpixels”, Figure 6.13(b). These structures could be designed such that the largest dimension is still smaller than the $\sim 80 \mu\text{m}$ resolution limit of the human eye at 35 cm [18]. To maintain a uniform density of all three colors, the slit spacing can be kept constant over all devices and the different colors of each “superpixel” can be selected by simply varying the depth of that pixels’ output slits. For a given $5 \mu\text{m}$ slit at a given wavelength within the superpixel structure, these devices provide between 0.02% and 0.1% transmission. A three-dimensional schematic of such a structure is shown in Figure 6.13(c).

6.9 Conclusion

In this chapter we have shown that metal-insulator-metal waveguides utilizing lithium niobate offer a unique opportunity for tunable light filters. By varying the spacing between the input and output slits, the intensity of a selected color oscillates as a function of the separation. Also, by varying the output slit depth within the device, one can preferentially couple to each of the photonic modes within the waveguide. The electro-optic effect of lithium niobate allows the selected output color to be shifted across the red, green, and blue regions of the visible spectrum. Furthermore, these structures could produce color pixels that are orders of magnitude smaller than current technologies and could provide an opportunity for devices with a significantly higher resolution than those currently available.

In this part of the thesis we have shown that, with proper design, single crystal thin film layers of ferroelectrics can be produced using ion implantation induced layer transfer. Silver bonding can improve the adhesion between the transferred film and the substrate to which it will be bonded. These methods can be used to fabricate single crystal MIM waveguides which can be used in tunable color filtering. In the following part of the thesis, we will explore using doped silicon and transparent conducting oxides as the active layer of the MIM waveguide.

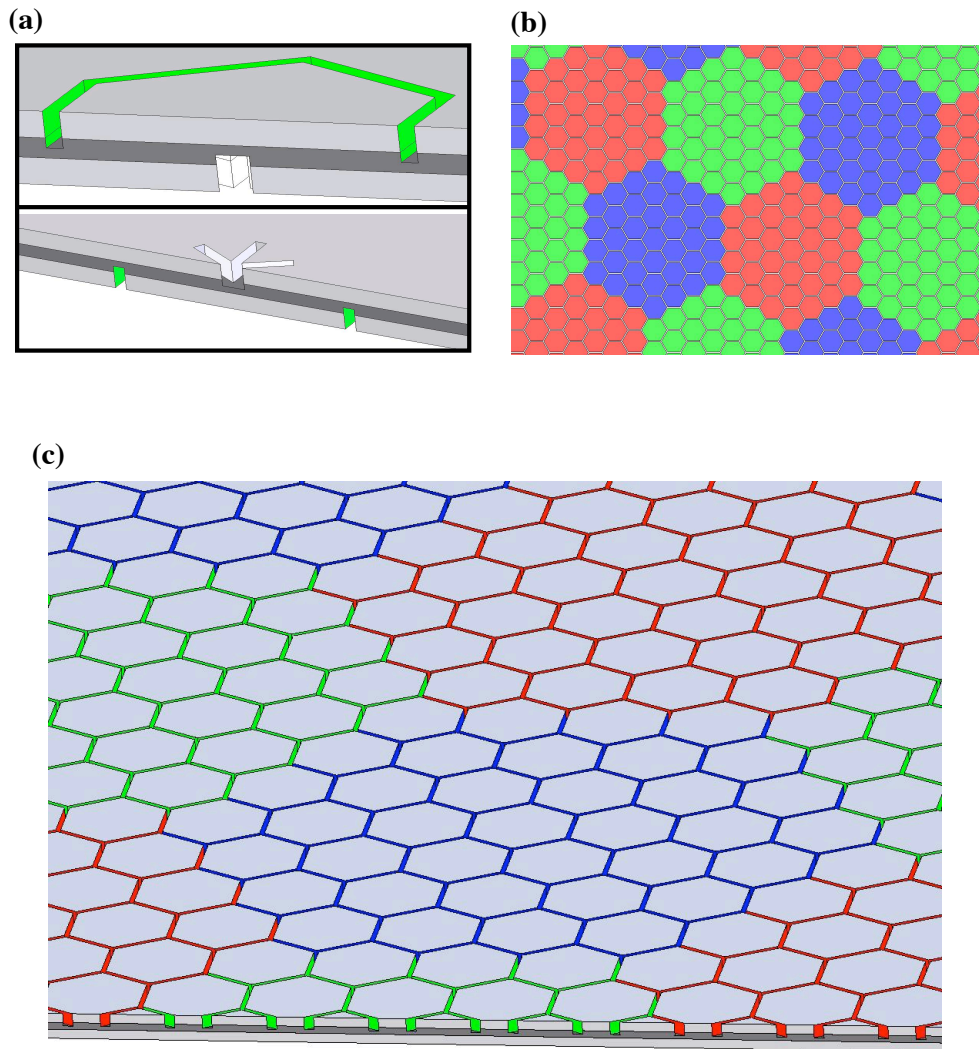


Figure 6.13. Cutaway view of a six-sided MIM color filter (a). The top panel shows half of the hexagonal output structure while the bottom panel shows half of the three-slit input configuration for a given hexagon. (b) shows a tiling layout for a red-green-blue “superpixel” design where the largest dimension of each red-green-blue combination is smaller than the resolution limit of the human eye. A three-dimensional rendering of such a device is shown in (c).

Part II

Semiconductor Slot Waveguides

Chapter 7

The plasMOStor: A Metal/Oxide/Si Field Effect Plasmonic Modulator

7.1 Introduction

In this part of the thesis, we discuss using doped silicon layers and transparent conducting oxides as the active layers in MIM waveguides. With these devices, modulation of the optical signal is based on changing the carrier density distribution within the active region. An added benefit of using silicon as the active region is that this material forms the basis for much of the semiconductor industry. Besides being one of the most extensively studied material in existence, silicon already forms the basis for complementary metal-oxide- semiconductor (CMOS) processes. Using silicon also allows plasmonic devices to be easily integrated into current fabrication processes when the focus is on designing chip-based all-optical and optoelectronic computational networks. Designing plasmonic-based circuits will require ultracompact Si-compatible modulators, ideally comprising dimensions, materials, and functionality similar to electronic complementary metal-oxide-semiconductor (CMOS) components. Here we demonstrate such a modulator, based on field-effect modulation of plasmon waveguide modes in a MOS geometry. Near-infrared transmission between an optical source and drain is controlled by a gate voltage that drives the MOS into accumulation. Using the gate oxide as an optical channel, electro-optic modulation is achieved in device volumes of half of a cubic wavelength with femtojoule switching energies and the potential for gigahertz modulation frequencies. ¹

7.2 CMOS and the Emergence of Plasmonics

The integrated circuits ubiquitous in modern technology were critically enabled by the invention of the metal-oxide-semiconductor field effect transistor (MOSFET) - a three-terminal device that

¹This chapter is based on work done with Dr. Luke Sweatlock and Dr. Jennifer Dionne [34].

modulates current flow between a source and drain via an applied electric field. Since the first successful demonstration of MOSFETs in the 1960s, silicon devices and circuits have continuously scaled according to Moore’s law, which predicts that the density of electronic circuits within a chip of a given size will double every 18 - 24 months. This has been done by increasing both the integration density and bandwidth of complementary metal-oxide-semiconductor (CMOS) networks. At present, microprocessors contain over 800 million transistors clocked at 3 GHz, with transistor gate lengths as small as 35 nm [20, 53]. Unfortunately, as gate lengths approach the single-nanometer scale, following Moore’s Law becomes increasingly difficult. MOS scaling is accompanied by increased circuit delay and higher electronic power dissipation - a substantial hurdle to Moore’s law often referred to as the interconnect bottleneck.

To circumvent the electrical and thermal parasitics associated with MOS scaling, new interconnect technologies are being considered. Particular attention has been given to optical technologies, which could achieve high integration densities without significant electrical limitations [73, 113, 119]. On-chip optical components would offer a substantially higher bandwidth, a lower latency, and a reduced power dissipation compared with electronic components [73, 83, 119]. Unfortunately, the size of these optical components is diffraction limited as discussed in Chapter 1.

Here, we present an experimental demonstration of a field effect Si modulator based on multimode interferometry in a plasmonic waveguide. Like the Si-based modulators implemented by Lipson and colleagues [124], this device utilizes high optical mode confinement to enhance electro-optical nonlinearities in Si. Moreover, like the Si optical modulator of Liu and colleagues [68], this device exploits the fast modulation of accumulation conditions in a metal-oxide-semiconductor (MOS) capacitor. In contrast with these and related structures [69], our plasmonic modulator can achieve modulation of nearly 10 dB in device volumes of half a cubic wavelength. In particular, our device illustrates that conventional scaled MOSFETs can operate as optical modulators, by transforming the channel oxide into a plasmon slot waveguide.

7.3 Design and Fabrication of the plasMOSter

To fabricate the plasmistor, we start with a silicon-on-insulator (SOI) wafer having a doped device layer (n-type) with carrier concentrations of $9 \times 10^{16} \text{ cm}^{-3}$ and an initial thickness of $1.5 \mu\text{m}$, Figure 7.1(a). The wafer is initially covered in a chemically resistant Logitech chemical mechanical polishing wax. The entire sample is covered with the exception of an etch window that is left

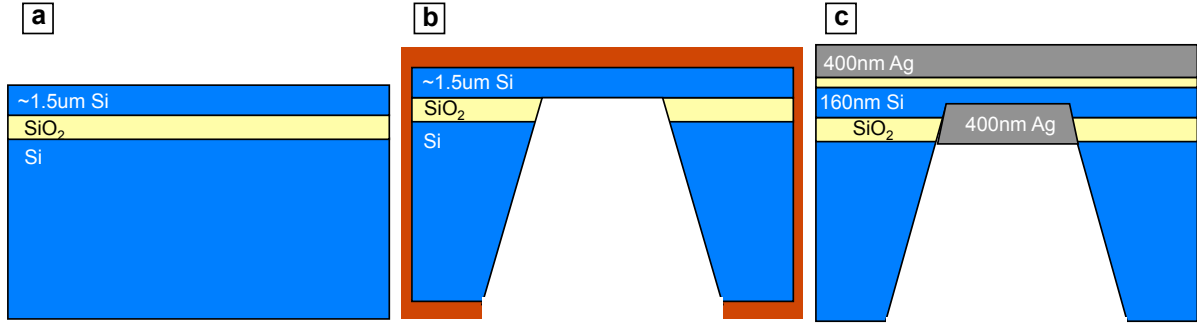


Figure 7.1. Etching and oxidation steps involved in the plasmistor fabrication.

exposed on the bottom, handle substrate, Figure 7.1(b). A mixture of 5:1 nitric to hydrofluoric acid is constantly stirred while the waxed sample is placed in the etch bath. After ~ 60 minutes, a region within the etch window will reach the buried oxide layer of the SOI wafer and the etch window will change color from black to white. The sample is then removed from the etch and placed in buffered oxide etch (BOE) until the buried oxide layer is removed (~ 2 nm/sec), Figure 7.1(b). The wax layer is then removed by soaking in acetone over night.

At this point, the silicon device layer exists as a free-standing, single crystal silicon membrane. The thickness of this membrane was determined using spectroscopic ellipsometry which is discussed in detail in Appendix C. To thin the membrane, wet oxidation was performed and the oxidation time was calculated using Reference [24]. The membranes were thinned to the desired thickness, and then a 10nm oxide layer was grown on the top surface. After oxidation, 400 nm of silver was evaporated on the top and bottom surfaces of the membrane. A schematic of the final structure is shown in Figure 7.1(c).

It should be noted that, while we do not currently believe that strain within the membranes significantly contributes to the overall performance of the device, both Raman and x-ray diffraction measurements of the membranes at varying thicknesses indicated that the membranes were in a state of tensile stress. For the critical thickness used in these studies, both measurement techniques indicated that the silicon was under ~ 500 MPa of tensile stress. This effect was considered when determining the effective electron mass for the Drude model. This is shown in Figure 7.2. The pannel on the left shows Raman peak shifting as a function of silicon membrane thickness. The pannel on the right shows rocking curve x-ray diffraction measurements of thick and thin SOI and silicon membranes. The peak splitting shown in the thinned membrane pannel indicates that the

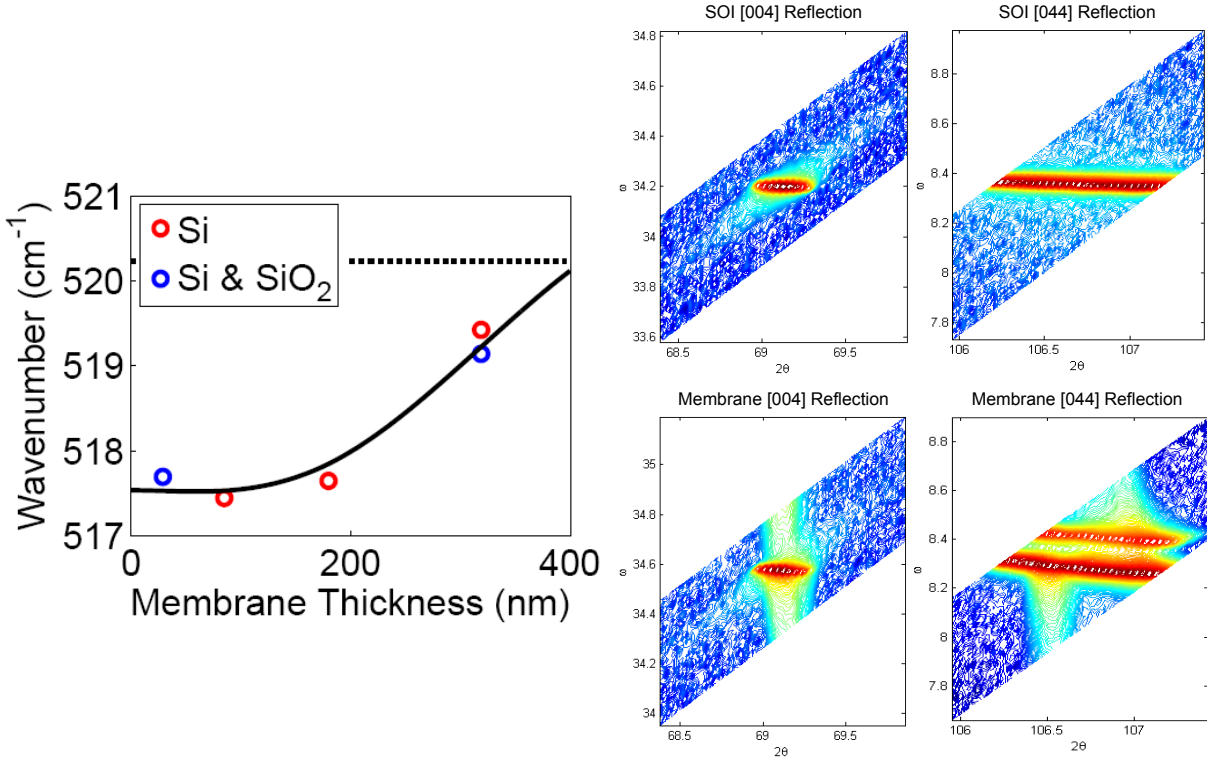


Figure 7.2. Raman peak shifting as a function of silicon membrane thickness (left panel). Rocking curve x-ray diffraction measurements of thick and thin SOI and silicon membranes (right panel).

tensile stress in the thinned membranes has distorted the lattice to the point that two separate lattice constants are present in the out-of-plane direction and the in-plane direction.

Sub-wavelength input and output slits were milled into the top and bottom of the membrane, respectively, Figure 7.3. Light was coupled into and out of the plasmistor via subwavelength slits etched into the top and bottom cladding layers (Figure 7.3(b)). This double-sided coupling configuration provides for a dark-field imaging configuration with minimal background signal, though end-fire excitation could also be used. Note that in this geometry, the slits function as the optical source (input) and drain (output) of the plasmistor. As seen in Figure 7.3(b), the input slits are defined to a length of approximately $4 \mu\text{m}$, which determines the lateral extent of waveguided modes [35]. To map transmission as a function of device length, the input-output slit separation was varied from approximately $1 - 8 \mu\text{m}$ in 50 nm increments. An overview of the entire device is shown in Figure 7.4. Here each of the dark spots on the membrane represent a different device. All the devices were spaced such that there was no cross-talk between them.

At $\lambda = 1550\text{nm}$, in the absence of an applied electric field, dispersion calculations for the

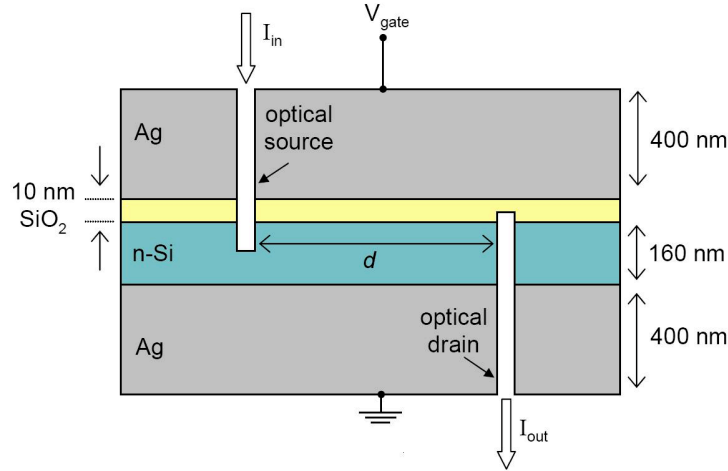


Figure 7.3. Cross-sectional schematic of the Si field effect plasmonic modulator.

plasmistor show the existence of two optical modes: a photonic mode lying to the left of the Si and SiO₂ light lines, and a plasmonic mode lying to the right of the Si light line. Both modes will be generated at the plasmistor source and can interfere either constructively or destructively at the drain, depending on the source-drain separation, Figure 7.5(a). The nearly-flat dispersion of the photonic mode around $\lambda = 1.55 \mu\text{m}$ suggests that this mode will be extremely sensitive to changes in the Si complex index. For example, modifying the Si index through free-carrier absorption will push this mode into cutoff, such that the dispersion curve intercepts the energy axis just above $\lambda = 1.55 \mu\text{m}$. The remaining plasmonic mode will then propagate through the plasmistor without interference from the photonic mode. Dispersion calculations confirm that upon application of an electric field, the plasmonic mode remains mostly unchanged, while the photonic mode is pushed into cutoff, Figure 7.5(b). As a comparison, looking at 7.5(a) and (b) for devices operated at $\lambda = 685 \text{ nm}$, the dispersion diagrams show negligible changes between the on state and the off state.

Modal properties were calculated via a numerical solution of Maxwell's equations and assume uniform coupling across the waveguide stack. For reference, the dispersion diagram also includes the light lines in Si and SiO₂, corresponding to light propagation through bulk media with refractive index $n = n_{\text{Si}}$ or n_{SiO_2} .

Looking explicitly at the mode profiles, Figure 7.6 shows that in the absence of an applied field at the gate, the plasmistor is fully depleted and light can be guided from the source to the drain through both the Si and SiO₂ layers. As seen in Figure 7.6(b), the photonic mode (red) is characterized by an electric field localized predominately in the Si core and a mode index of $n = 0.375$. In contrast, the plasmonic mode (blue) exhibits maximal field intensities within the SiO₂

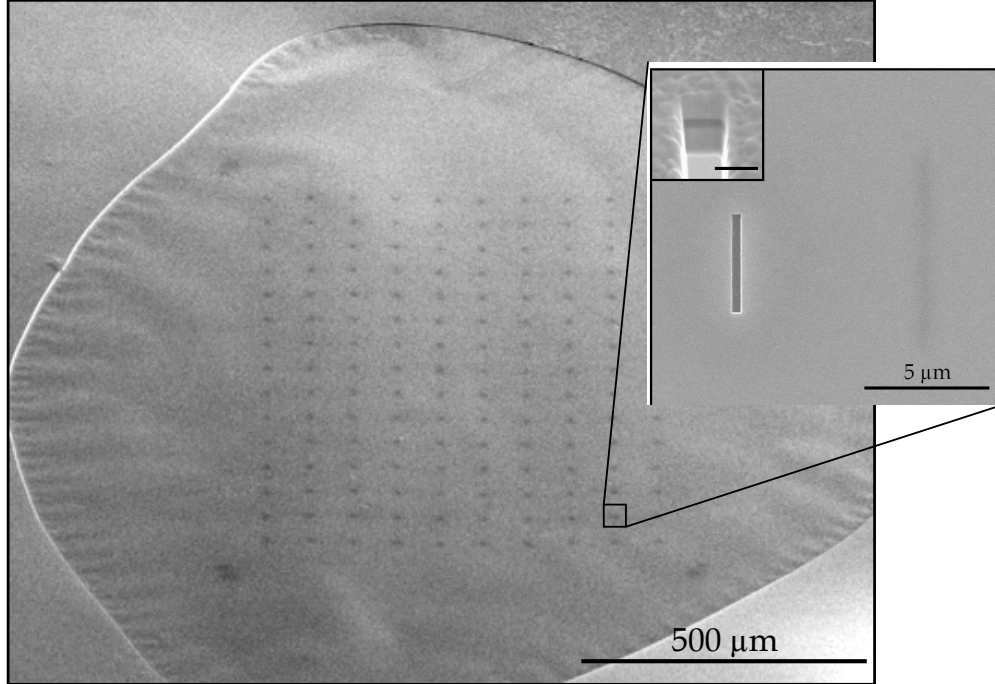


Figure 7.4. An overview of an entire plasmistor membrane. In the large inset, the input slit is visible on top of the membrane. Using high energy imaging in the SEM, we can see through the membrane and also image the output slit. The small inset shows a cross-sectional cut through the 4-layer plasmistor waveguide (scale bar is 500 nm).

channel and a mode index of $n = 3.641$. While the high plasmonic mode index arises from mode overlap with the Ag and Si layers, propagation losses remain relatively low. At $\lambda = 1.55 \mu\text{m}$, losses of the plasmonic and photonic modes are $0.207 \text{ dB}/\mu\text{m}$ and $2.37 \text{ dB}/\mu\text{m}$, respectively. For both modes, fields in the metal cladding decay within approximately 20 nm of the Ag-Si and Ag-SiO₂ interfaces.

For devices that were fabricated using n-type silicon, the changes just described are induced by applying a positive bias to the gate. For drive voltages above the flat-band voltage, electrons in the n-type Si form an accumulation layer characterized by a peak carrier concentration at the Si/SiO₂ interface and a spatial extent given by the Debye length. Figure 7.6 tabulates the theoretical change of mode index and propagation length with the onset of accumulation. To represent the spatially-varying charge distribution predicted by Poisson's equation, the accumulation layer is modeled as five discrete Drude layers with an average plasma frequency of $7.94 \times 10^{14} \text{ Hz}$ and a Debye decay length of 14 nm. The parameters used for the five-layer stack are listed in Table 7.1.

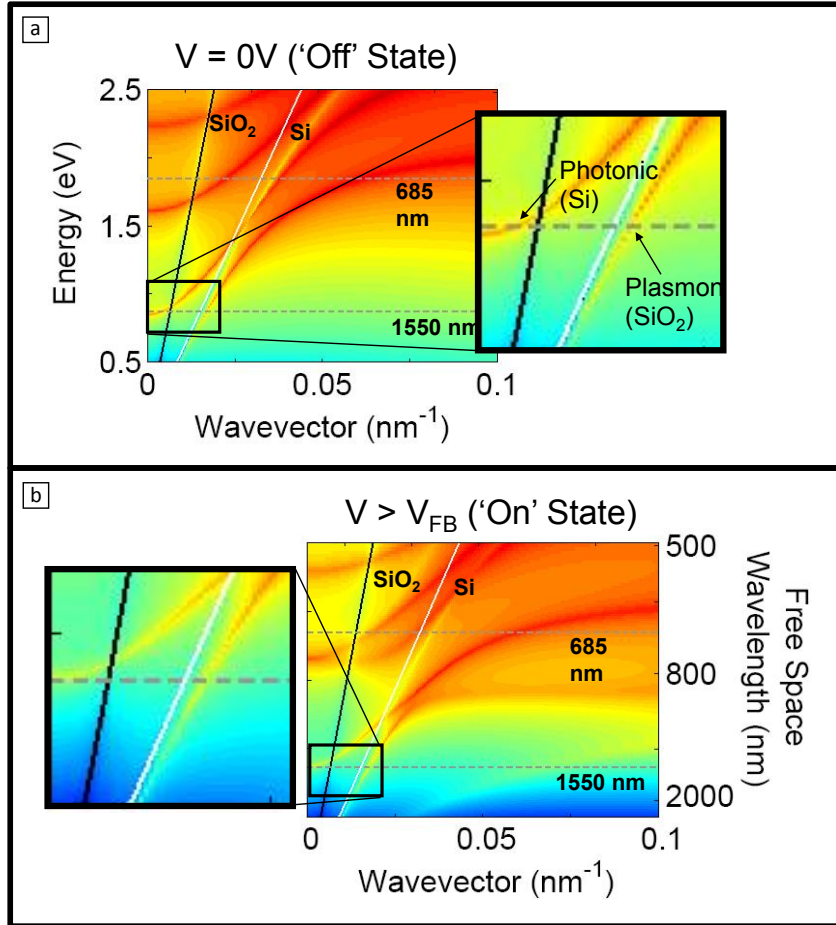


Figure 7.5. Plasmostor dispersion relation with and without and applied electric field. With no applied electric field, both the plasmonic and photonic modes contribute to device behavior. With an applied field, the photonic mode is pushed into cutoff and all that remains is the plasmonic mode.

Note that both the Drude model and the Debye approximation were used for simplicity. As expected, the effective index and losses of the plasmonic mode exhibit very little change between the voltage-off (depletion) and voltage-on (accumulation) states. In particular, the plasmonic mode index varies from the off state by $\Delta n = 0.008$, and losses are only slightly increased to $0.228 \text{ dB}/\mu\text{m}$. However, the photonic mode is pushed into cutoff, as indicated by the near-zero mode index and the fact that the losses increase by an order of magnitude (i.e., the photonic mode becomes evanescent and can no longer propagate power through the device). Therefore, in the accumulation state, the plasmostor will guide near-infrared light almost exclusively through the SiO_2 channel [61], solely via the plasmonic mode.

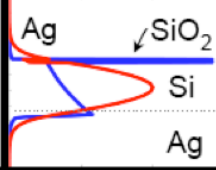
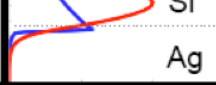
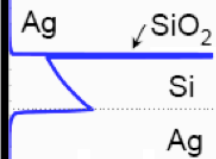
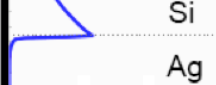
$\lambda=1.55\mu\text{m}$	$ E $ mode profile	Mode Index	Loss (dB/ μm)
Off state ($V=0$) <i>depletion</i>		3.641	0.207
		0.375	2.37
On state ($V>0.7\text{V}$) <i>accumulation</i>		3.649	0.228
		0.033	28.14

Figure 7.6. Tabulated mode properties of the plasmistor with and without an applied electric field.

Table 7.1. 5-layer stack used in plasMOSStor modeling.

Thickness (nm)	Carrier Concentration (cm^{-3})	Conductivity (S/cm^3)
5	7×10^{19}	2.17×10^6
12	3×10^{19}	9.30×10^5
33	8×10^{18}	2.48×10^5
50	5×10^{17}	1.55×10^4
73	1×10^{16}	3.098×10^2

7.4 Switching Behavior

Modulation of the electric field distribution and out-coupled power is illustrated in the finite difference time domain simulations of Figure 7.7 and 7.8. In these simulations, the plasmistor is illuminated through the optical source with a gaussian beam of wavelength $\lambda = 1.55 \mu\text{m}$ or $\lambda = 685 \text{ nm}$, and the source-drain separation is set to $d = 2 \mu\text{m}$. As seen in the left column of Figure 7.7, in the absence of an applied field, plasmistor transmission at $\lambda = 1.55 \mu\text{m}$ is distributed throughout the Si core with sparse regions of high electric field in the oxide slot. However, with the onset of accumulation, the field transmitted within the Si core is notably decreased. As seen in the right column of Figure 7.7, plasmistor fields are localized predominately within the 10 nm-thick oxide layer,

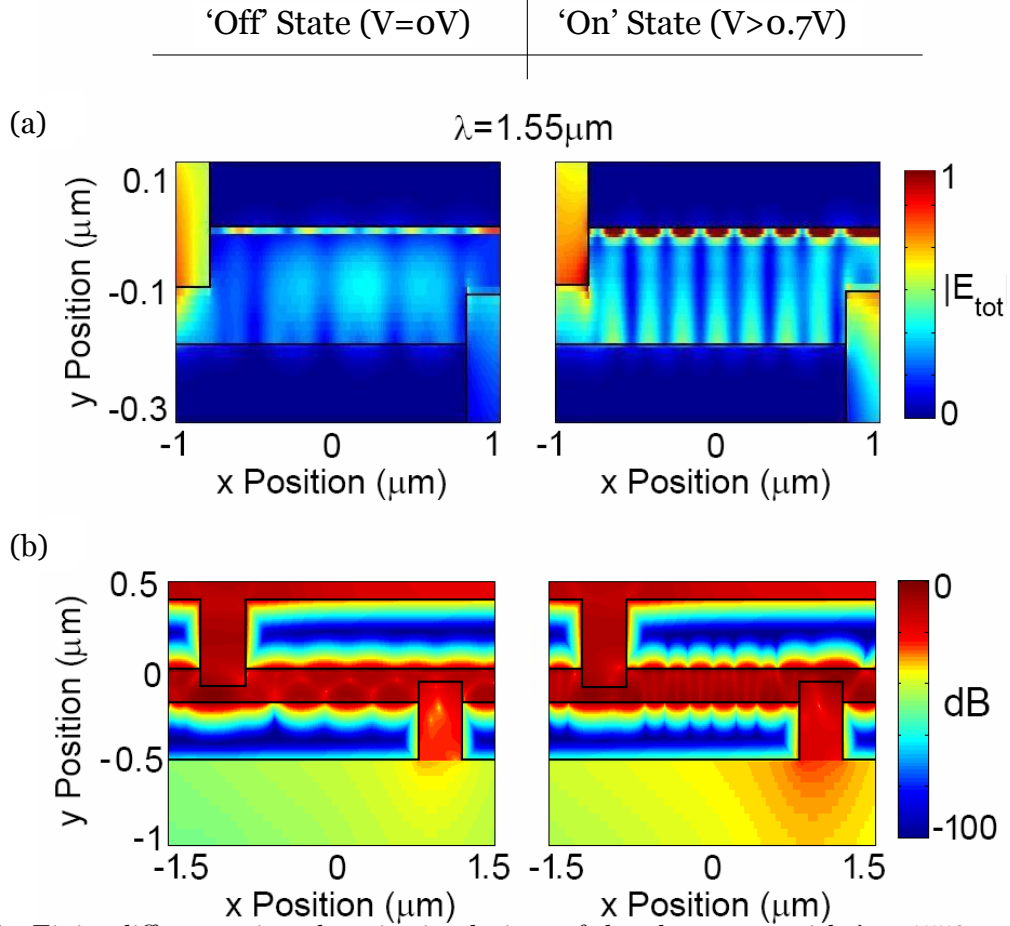


Figure 7.7. Finite difference time domain simulations of the plasmistor with $\lambda = 1550 \text{ nm}$, showing the total electric field and the transmitted power for a $2\text{-}\mu\text{m}$ -long optical source-drain separation.

which acts as a channel between the optical source and optical drain. Within the slot, pronounced maxima and minima within the resonator can be observed with a wavelength of approximately 225 nm .

By choosing the source-drain separation to correspond to a condition of destructive interference between the photonic and plasmonic modes, plasmistor transmission can be substantially increased by inducing accumulation. Figure 7.7(b) plots the total power transmitted through the plasmistor at $\lambda = 1.55 \mu\text{m}$, with $d = 2 \mu\text{m}$. Comparing intensities at the optical drain between the voltage-off and voltage-on states, simulated modulation ratios exceeding $+10 \text{ dB}$ can be observed.

For comparison, at $\lambda = 685 \text{ nm}$, the unbiased plasmistor exhibits three modes with effective indices of $n = 5.36, 3.40,$ and 2.28 . An applied field shifts these indices to $n = 5.35, 3.34,$ and 2.15 . Such multimode behavior is readily visualized in the simulated images of Figures 7.8(a)

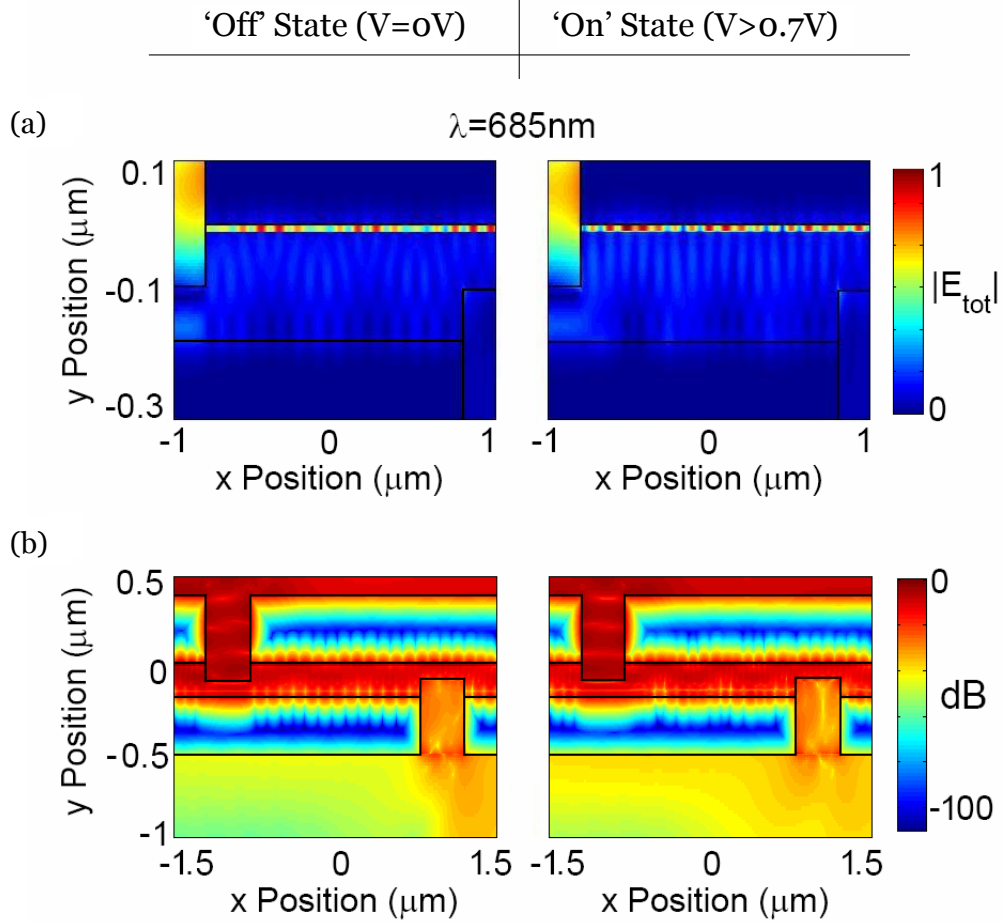


Figure 7.8. Finite difference time domain simulations of the plasmistor with $\lambda = 685 \text{ nm}$, showing the total electric field and the transmitted power for a $2\text{-}\mu\text{m}$ -long optical source-drain separation.

and (b). However, because Si is more absorbing in the visible, the propagation lengths of these modes do not exceed $3 \mu\text{m}$. The accumulation layer induces higher losses in the structure, and modulation between the voltage-on and voltage-off states results almost exclusively from absorption of all modes. The higher absorption and multi-mode behavior at visible wavelengths suggest that when the plasmistor is designed using silicon with the thicknesses reported, the device is ideally suited for near-infrared operation.

Experimental capacitance-voltage (CV) curves were used to characterize the electrical response of our fabricated plasmistor. Figure 7.9(a) shows a high-frequency CV curve obtained with a driving frequency of 100 kHz , measured over an area of approximately $100 \mu\text{m} \times 100 \mu\text{m}$. As the figure reveals, the plasmistor is in a state of inversion for negative biases, depletion for biases between 0 and 0.7 V , and accumulation for biases greater than 0.7 V . The flat-band voltage, where the Si

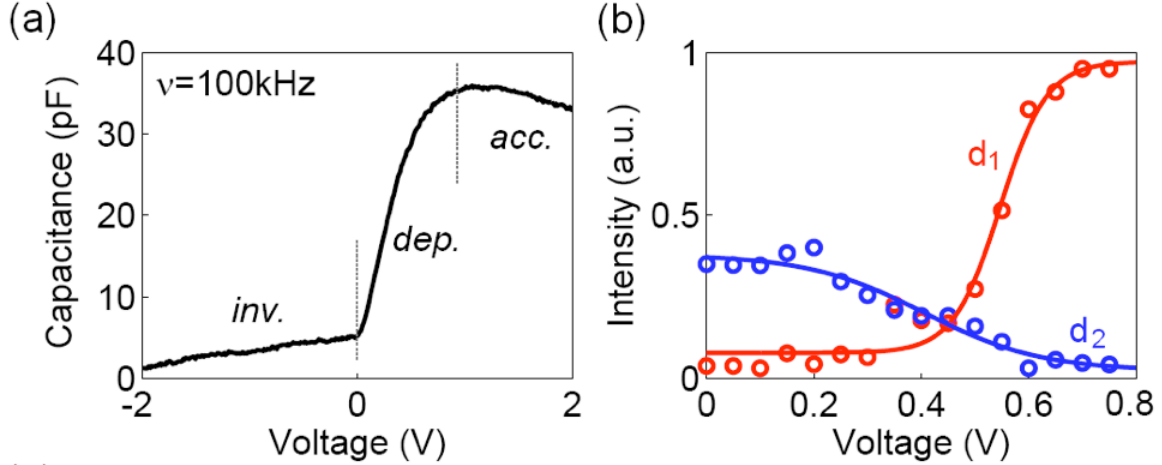


Figure 7.9. (a) High-frequency (100 kHz) capacitance-voltage curve of the modulator over a $\sim 100 \times 100 \mu\text{m}^2$ area. (b) Optical drain intensity as a function of gate bias for two source-drain separations ($d_1 = 2.2 \mu\text{m}$ and $d_2 = 7.0 \mu\text{m}$) at $\lambda = 1.55 \mu\text{m}$.

layer is charge neutral, occurs around 0.5 V. From the total observed accumulation capacitance (35 pF) of this sample region A_{meas} , we infer the capacitance of a typical plasmistor with areal dimensions $A_{plasmistor} = 4 \mu\text{m}^2$ as $C_{plasmistor} = C_{meas}(A_{plasmistor}/A_{meas}) = 14 \text{ fF}$.

To characterize the optical response, the out-coupled intensity from the plasmistor was monitored as a function of gate bias. An infrared laser source ($\lambda = 1.55 \mu\text{m}$) was focused onto a single device and transmission through the optical drain was imaged using a 50x microscope objective coupled to a Ge detector. Depending on the source-drain separation - and hence the interference condition of the photonic and plasmonic modes in the depleted state - transmitted intensity could increase or decrease with applied bias. As seen in Figure 7.9(b), a modulator of length $d_1 = 2.2 \mu\text{m}$ exhibits a pronounced intensity increase with increasing positive bias for $\lambda = 1.55 \mu\text{m}$. Consistent with the capacitance-voltage curves, modulation saturates around 0.7 V, corresponding to the onset of accumulation. In contrast, a modulator of length $d_2 = 7.0 \mu\text{m}$ exhibits a 30% decrease in transmitted intensity for $\lambda = 1.55 \mu\text{m}$.

This measurement was then repeated for every device shown in Figure 7.4. Full experimental optical characterization was achieved by varying the source-drain separation and the illumination wavelength, both with and without an applied bias. Figure 7.10 shows plasmistor transmission as a function of resonator length for source wavelengths of 685 nm and 1.55 μm , respectively. As

seen in the top pane of Figure 7.10, at a wavelength of 685 nm, negligible modulation is observed for TM-polarized light between the voltage on and off states of the modulator. For shorter cavity lengths, transmission predominately decreases with applied bias. Cavities longer than $2.5 \mu\text{m}$ are dominated by extinction, consistent with mode propagation lengths derived from calculations.

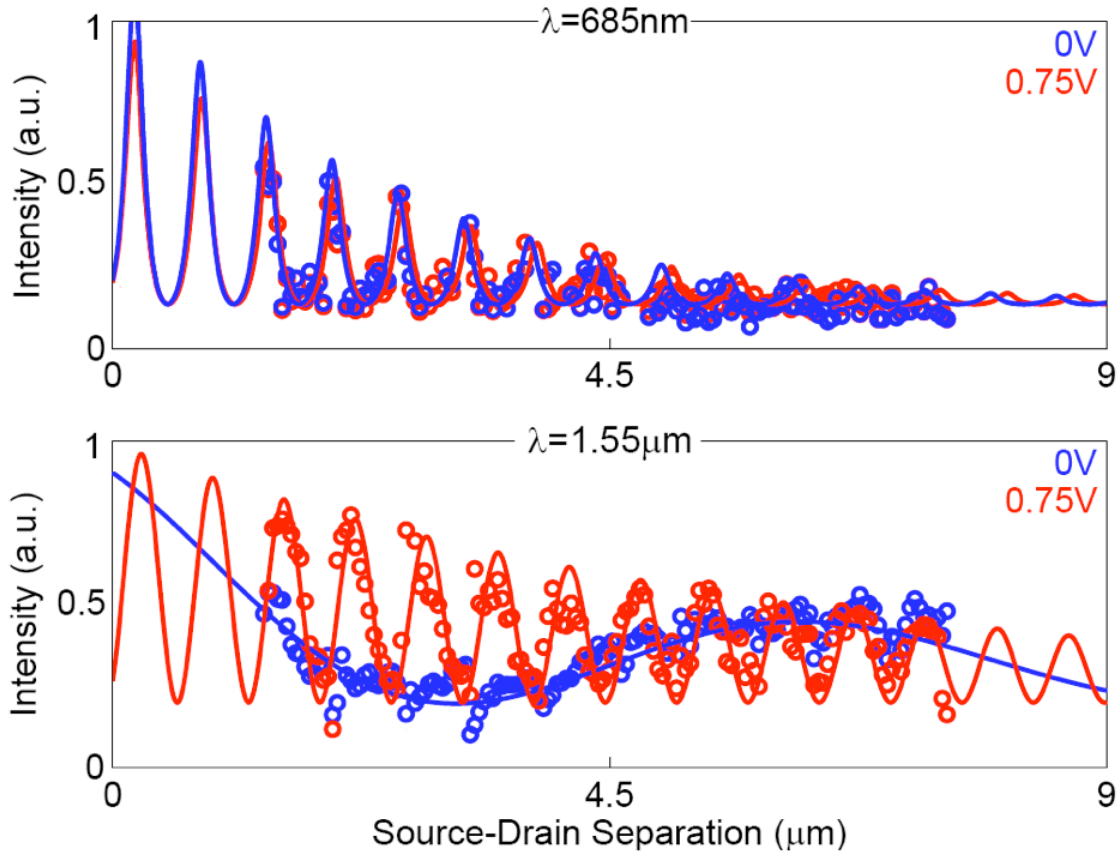


Figure 7.10. Optical drain intensity as a function of source-drain separation for the voltage-off state (blue, $V = 0$) and the voltage-on states (red, $V = 0.75 \text{ V}$) at $\lambda = 685 \text{ nm}$ and $\lambda = 1.55 \mu\text{m}$.

In contrast, the plasmistor exhibits pronounced modulation for near-infrared sources. As seen in the bottom pane of Figure 7.10, with no applied bias, plasmistor transmission at $\lambda = 1.55 \mu\text{m}$ is characterized by an output signal comprised of both high and low frequency components. As illustrated by the dispersion diagram of Figure 7.5, these components correspond to the plasmonic and photonic waveguide modes, respectively. An applied bias of 0.75 V forces the photonic mode

into cut-off, leaving only a single, high-frequency mode in the waveguide. Experimentally, the observed propagation length of this mode is in fair agreement the plasmonic mode losses predicted from calculations. The observed mode index is about half the calculated plasmon index, likely due to aliasing effects arising from the chosen optical source-drain separation step-size. Still, source-drain separations of approximately $2 \mu\text{m}$ exhibit amplitude modulation ratios as high as $+11.2 \pm 0.6$ dB. Such observations are consistent with the simulations of Figure 7.7. To our knowledge, this plasmistor yields one of the highest reported near-infrared Si modulation depths in the smallest reported volume, with device volumes as small as one half of a cubic wavelength.

Plasmistor modulation depths remain high for wavelengths spanning from $1.48 \mu\text{m}$ to $1.58 \mu\text{m}$ (the range of our infrared source), where changes in the complex refractive index of Si induce cut-off of the photonic mode. For these wavelengths, significant modulation is preferentially observed in shorter resonator lengths ($d < 3 \mu\text{m}$), which in the depleted state produce destructive interference between the photonic and plasmonic modes. Previous Si modulators based on MOS capacitors, in contrast, require device dimensions on the order of millimeters [68]. Interestingly, the internal waveguide propagation losses of the plasmistor are not significantly higher than 1 dB (for a source-drain separation of $d = 2.2 \mu\text{m}$, the plasmonic mode has a propagation loss of 0.5 dB). Thus, despite the higher losses generally associated with plasmonic components, the plasmistor exhibits propagation losses that are comparable with traditional Si- or dielectric-based modulators [68, 69, 124].

We note that the prototype plasmistor reported here incurs additional losses from mode insertion and extraction through the “source” and “drain” slits employed in our device. Using full field electromagnetic simulations, we calculate an insertion loss of -12.8 ± 0.1 dB and an extraction loss of -3 ± 1 dB. Combined with the waveguide propagation losses, then, this prototype plasmistor exhibits a total on-chip loss of approximately -17 dB, in rough accord with the total experimentally-determined loss of approximately -20 dB. However, we do not consider these high coupling losses intrinsic to device operation, since slit coupling is not fundamental to plasmistor modulation. In fact, our simulations indicate that by modifying the coupling geometry to simple, non-optimized end-fire excitation from a Si-waveguide, an increased coupling efficiency of 36% (coupling losses of 4.4 dB) can be achieved. Moreover, as reported by Veronis and Fan [118], optimization techniques have been proposed to achieve $> 90\%$ incoupling efficiencies into plasmonic waveguides, corresponding to coupling losses as low as 0.3 dB. Thus, future plasmistors with a device length of approximately 2 microns and more optimal incoupling could achieve overall “on” state losses as

low as 1.1 dB.

7.5 Time Response Analysis

The frequency response of the plasmistor was characterized by applying a 4 V, 100 kHz pulse train to the modulator with a rise-time of 10 ns. Plasmistor switching was determined to be at least as fast as 10 ns, which was limited by the frequency response of our pulse generator. We note, however, that modulation speeds of a plasmistor are likely to be fundamentally limited by the speed of formation of the MOS accumulation layer, as is true in a conventional small-geometry MOSFET; accordingly, plasmistor operation should be compatible with GHz modulation frequencies. This device could potentially respond even faster than traditional MOSFETs because of the fact that this device is based on forming an accumulation layer with majority carriers within the device, rather than minority carriers which are often manipulated using MOSFETs.

To explore the potential for GHz modulation in more detail, we conducted circuit simulations of our plasmistor driven into accumulation by optical means. For example, a photodiode connected to the plasmistor gate could provide sufficient power to modulate the channel properties [80]. Provided the photodiode could produce gate voltages exceeding 0.7 V, this coupled plasmistor-photodiode system could form the basis for all-optical MOS-based modulation. Figure 7.11 proposes such a scheme for all-optical modulation. As seen, a Ge p-i-n photodiode is connected to the plasmistor in parallel with a dielectric (a resistor). Here, the plasmistor is modelled using the experimentally-inferred capacitance (14 fF) of a typical $4 \mu\text{m}^2$ device. Similarly, the photodiode is modelled using circuit parameters from state-of-the-art small photodiodes [57] exhibiting quantum efficiencies of 10% under 6 mW optical illumination. Using a photodiode with an active area of $75 \mu\text{m}^2$ and an ~ 40 GHz bandwidth [57], circuit simulation indicates coupled plasmistor-photodiode bandwidths of 3 GHz (Fig. 5a). Scaling the photodiode active area to $4 \mu\text{m}^2$ (and thereby increasing the photodiode bandwidth [57]), coupled plasmistor-photodiode bandwidths increase to 15 GHz. Further improvements could be achieved by varying the oxide thickness or the plasmistor gate length. Moreover, by tuning the magnitude of the optical carrier (λ_1) and signal (λ_2) sources, this coupled photodiode-plasmistor system could exhibit signal gain at the plasmistor drain [80]. This three-terminal, integrated optical device requires no electronic conditioning and can be fabricated from SOI waveguide technology, using, for instance, local oxidation of silicon (LOCOS) processing. Such processing would facilitate CMOS compatibility while minimizing optical insertion losses.

7.6 Conclusion

In this chapter we have shown that the plasmistor offers a unique opportunity for compact, Si-based field effect optical modulation using scaled electronic MOSFET technology. The empirically determined switching voltage (0.7 V) and capacitance (14 fF) yield a required switching energy of $E = CV^2 = 6.8$ fJ for a typical $4 \mu m^2$ plasmistor device, commensurate with existing CMOS and optical logic gates [69]. To our knowledge, the plasmistor achieves the first electrical amplitude modulation of light in a plasmon waveguide. Furthermore, by modulating optical signals with a photodiode coupled to the gate, the plasmistor promises potential for opto-electronic and perhaps even all-optical Si-based modulation.

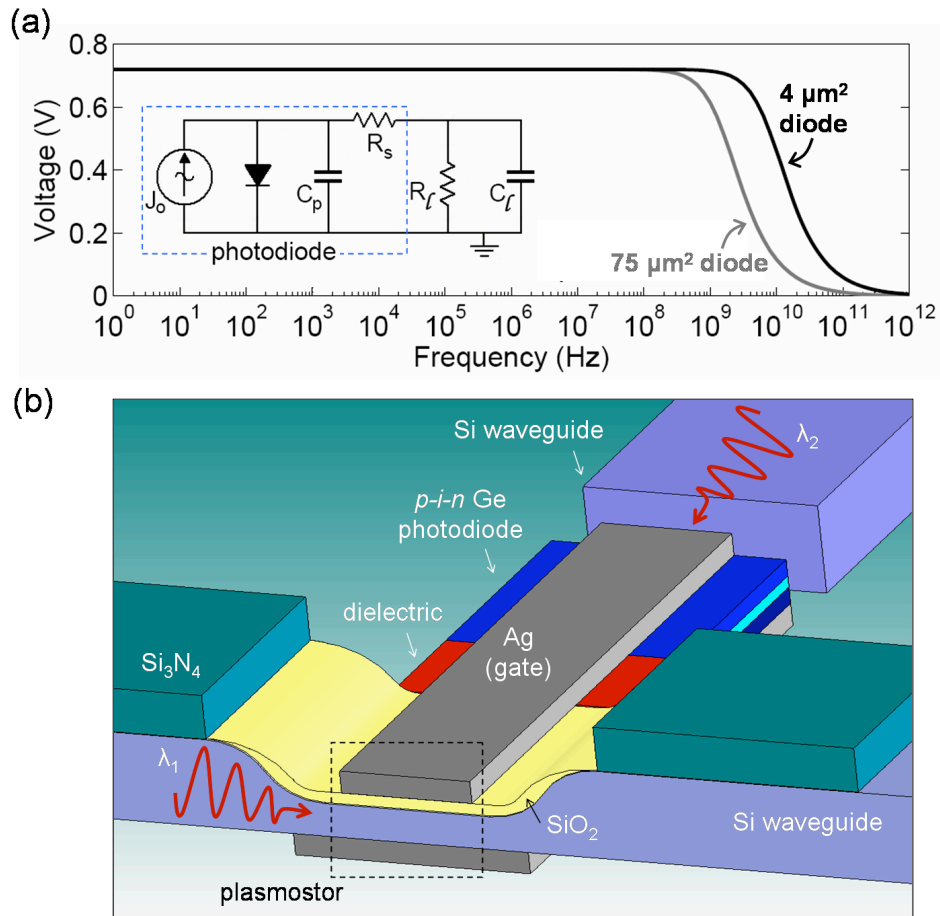


Figure 7.11. Circuit analysis of the coupled photodiode-plasmistor system, modelling the photodiode after reference [57] and the plasmistor as a MOS capacitor with a capacitance of 14 fF. (a). Schematic of an SOI-based all-optical plasmistor (b).

Chapter 8

Transparent Conducting Oxides for Active Plasmonics

8.1 Introduction

In this chapter, a third method for mode modulation within MIM waveguides is discussed. Here we use transparent conducting oxides (TCOs) as the active layer within the waveguide. These materials can achieve carrier concentrations on the order of 1×10^{19} - 1×10^{21} cm^{-3} . Based on Drude model calculations, this results in plasma frequencies at near infrared and visible frequencies. By tuning the plasma frequency close to the frequency of operation of these devices, changes in the real part of the refractive index on the order of $\Delta n_{index} = 1$ are achieved. Here we demonstrate switching in such a device with an MOS geometry. Structures were fabricated with gold as the top and bottom cladding layers and a layer of TCOs and silicon dioxide were sputter deposited between the metal layers. Spectroscopic ellipsometry was used to measure the complex indices of refraction within the multi-layer stack and determine the extent to which the effective index of the supported optical modes was shifted. ¹

8.2 Carrier Modulation in Active Plasmonics

The field of active plasmonics is continually exploring new methods of plasmon mode modulation. Different waveguiding geometries have been developed that take advantage of optical switching in: thermally modulated systems [38], liquid crystal layers [41, 120], quantum dots [84], and ferroelectric films which was reported in the literature [31, 33, 70], as well as in Chapter 6.

In Chapter 7, modulation of the plasmon modes within a waveguide was demonstrated by modulating the carrier density within the dielectric layer of the MIM waveguide. This device had the benefit of being extremely fast (sub nano-second switching) as well as being CMOS compatible. However, the electro-optic effect in silicon is very small [107], and the change in index of refraction

¹This chapter is based on work done with Dr. Eyal Feigenbaum.

for even highly doped silicon is also small. Based on the Drude-Lorentz model [98]:

$$\Delta n_{index} = \frac{-e^2 \lambda_0^2}{8\pi^2 c^2 \epsilon_0 n_{index}} \left(\frac{\Delta n}{m_e^*} + \frac{\Delta p}{m_h^*} \right) \quad (8.1)$$

forming an accumulation layer in an MOS device (with an accumulation layer of $\Delta n = 10^{19} \text{ cm}^{-3}$), $\Delta n_{index} \simeq 0.002$ at $\lambda = 800 \text{ nm}$ and $\Delta n_{index} \simeq 0.009$ at $\lambda = 1500 \text{ nm}$. In Equation 8.1, m_e^* and m_h^* are the effective masses of the electrons and holes, respectively; and Δn and Δp are the changes in electron and hole concentrations (respectively) that induce a change in index of refraction, Δn_{index} . For the plasMOStor, the solution to this issue was to design the structure in such a way that there was exactly one photonic mode that was near cutoff. This produced large switching ratio's for a material with lower ($n = 9 \times 10^{16} \text{ cm}^{-3}$) carrier concentrations.

An alternative solution to this problem is to chose a dielectric material whose carrier density is much higher, and as a result, will have a plasma frequency closer to the visible and near infrared frequencies of interest. Based on the Drude model:

$$\epsilon = \epsilon_\infty - \frac{\omega_p^2}{\omega^2 + i\omega\omega_\tau} \quad (8.2)$$

Here, ϵ_∞ is the high frequency dielectric constant, ω_τ is the scattering frequency, and ω_p is the plasma frequency given by:

$$\omega_p = \frac{ne^2}{\epsilon m^*} \quad (8.3)$$

where m^* is the effective electron mass and n is the carrier concentration. The resulting change in ω_p as a function of carrier density is shown in Figure 8.1. In this figure, $\epsilon_\infty = 1$, $\omega_\tau = 0$, and $m^* = m_e$. The corresponding plasma frequency is given by the points where $\epsilon = 0$. As can be seen from the figure, by working with carrier concentrations on the order of $10^{20} - 10^{21} \text{ cm}^{-3}$, the plasma frequency of the layer will lie in the near infrared to visible frequency regime.

One family of materials that would satisfy these requirements is Transparent Conducting Oxides (TCOs). Both indium tin oxide (InTiO_3) and indium zinc oxide (InZnO_3) are degenerately doped oxides that are widely used as electrical contacts in solar cells, light emitting diodes, flat screen televisions, and cellular phone displays. These materials can be doped to have carrier concentrations between $10^{19} - 10^{21} \text{ cm}^{-3}$ based on manipulating the number oxygen vacancies and interstitial metal dopants. At the same time, these TCOs can have greater than 80% transmittance at visible frequencies [111]. Instead of using these materials as transparent contacts, in this

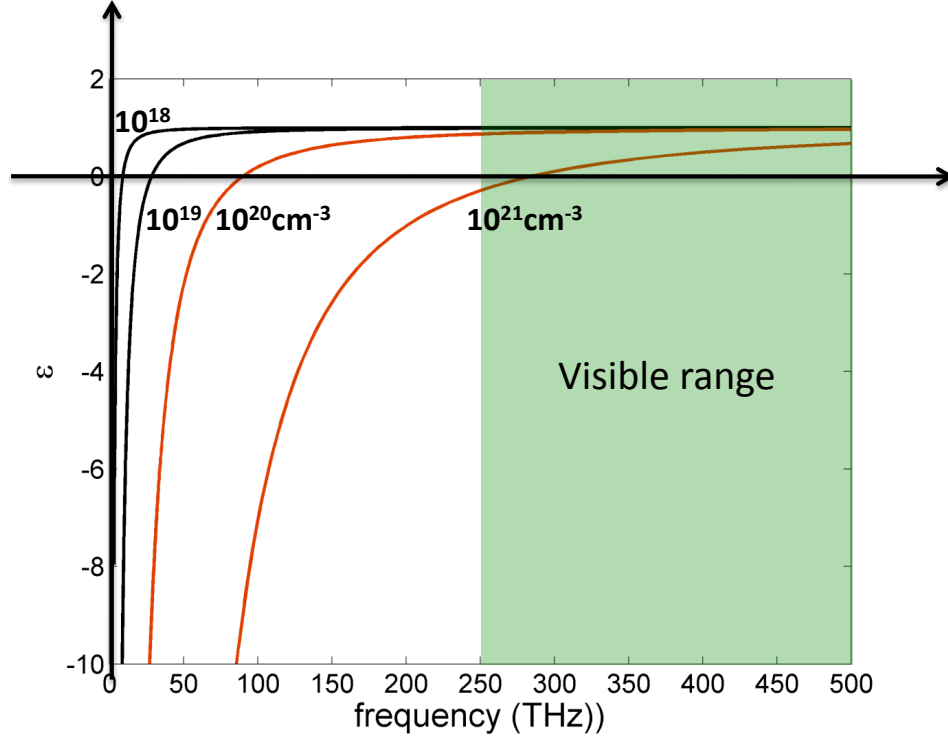


Figure 8.1. For this material: $\epsilon_\infty = 1$, $\omega_\tau = 0$, and $m^* = m_e$. The plasma frequency is given where $\epsilon = 0$.

chapter we demonstrate that these TCOs can be used as the active semiconductor within a MIM waveguide. These materials are used in a metal-oxide-semiconductor (MOS) structure similar to that of the plasmistor in Chapter 7 (Figure 8.2); and under an applied field, the device will form an accumulation layer. We show that by increasing the carrier concentration within the ~ 5 nm thick accumulation layer, the real part of the index of refraction can be shifted on the order of $\Delta n_{index} = 1$.

8.3 Fabrication and Characterization

For all experiments, InTiO_3 and InZnO_3 films were deposited using RF magnetron sputtering in an oxygen/argon plasma. All depositions were done at room temperature and 3 mTorr pressure within the chamber. For TCO depositions, the gas during sputtering was 1.29% O_2 and 98.71% Ar, and the films were sputtered at 200 W. The targets used were $(\text{In}_2\text{O}_3)_{0.9}(\text{ZnO})_{0.1}$, and $(\text{In}_2\text{O}_3)_{0.9}(\text{TiO})_{0.1}$ weight percent. For silicon dioxide (SiO_2) depositions, the gas during sputtering was 28.45% O_2

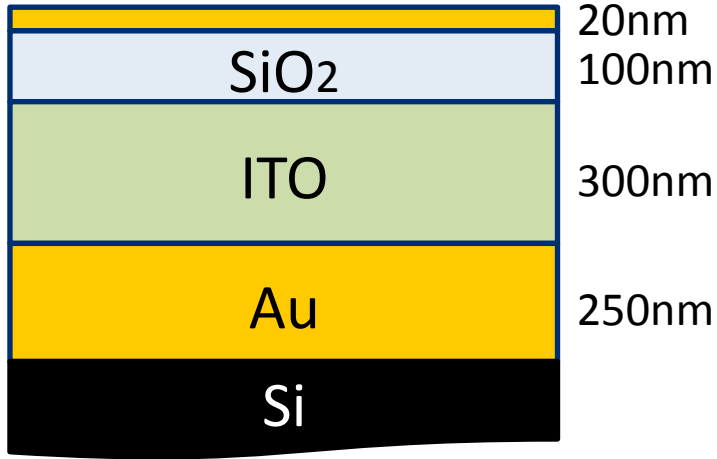


Figure 8.2. MOS structure used in the ellipsometry studies.

and 71.55% Ar, and the films were sputtered at 224 W. All gold films were deposited using thermal evaporation.

Films were characterized using Hall probe measurements and spectroscopic ellipsometry. The specifics of spectroscopic ellipsometry are covered in Appendix C. Films of InTiO₃ were deposited on quartz slides and Hall probe measurements determined that the electron mobility in these films was $\mu = 14.5 \text{ cm}^2/Vs$ and the electron equilibrium concentration was $n = 5 \times 10^{20} \text{ cm}^{-3}$.

To characterize the films in ellipsometry: Au, SiO₂, and InTiO₃ layers were deposited independently onto silicon substrates. All layers were measured from $\lambda = 460 - 820 \text{ nm}$. The layers were then deposited in a MOS structure shown in Figure 8.2. The layered structure deposited on silicon consisted of: 250 nm Au, 300 nm InTiO₃, 100 nm SiO₂, and a 20 nm semi-transparent top Au electrode. Fitting Ψ and Δ for each of the layers as well as the entire layer stack was done by minimizing the mean-square error between the model and measured data by varying the materials parameters. The SiO₂ films were modeled using a Cauchy layer (given by Equations D.1 and D.2) with $n_0 = 1.097$, $n_1 = 1405.8$, $n_2 = -1243.3$, $k_0 = 0.038$, $k_1 = -385.71$, $k_2 = 977.155$, $C_0 = 10^2$, $C_1 = 10^7$, and λ is given in nm. The InTiO₃ layer was modeled as a Drude layer with: $\lambda_p = 2300 \text{ nm}$, $\tau = 1 \text{ fs}$, and $\epsilon_\infty = 4.2$, and the value of λ_p was confirmed using Fourier transform infrared spectroscopy. As a result we obtained $n = 1 \times 10^{20} \text{ cm}^{-3}$, which is in good agreement with the value measured from the Hall probe.

8.4 Index Shifting in Indium Tin Oxide

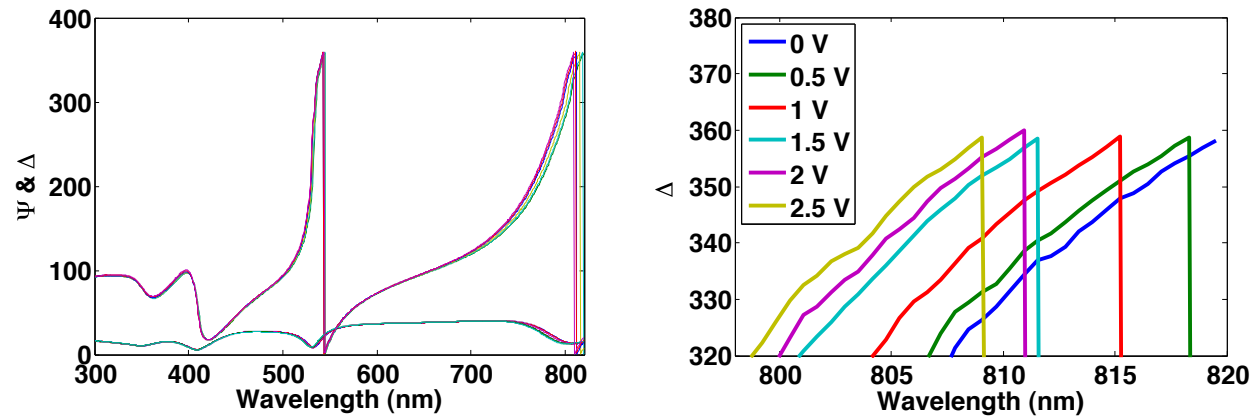


Figure 8.3. The ellipsometry measurements of the thin film stack shown in Figure 8.2 from 0 - 2.5 V in 0.5 V steps. The plot on the right focuses on peak shifting around 800 nm.

Ellipsometry measurements of the thin film stack are shown in Figure 8.3 from 0 - 2.5 V in 0.5 V steps. The plot on the left shows both Ψ and Δ over the entire visible spectrum, and the plot on the right is an expanded view of Δ from 795 - 820 nm. The latter plot clearly shows peak shifting with an applied field. Based on the materials parameters determined above, the complex index of refraction for InTiO_3 can be calculated using the Drude model. This is shown in Figure 8.4. The complex index of refraction is plotted as a function of wavelength and carrier concentration within the InTiO_3 layer from $n = 10^{20} - 10^{22} \text{ cm}^{-3}$. Here we see that by changing the carrier concentration within the material by 1 - 2 orders of magnitude, we can shift $\Delta n_{\text{index}} \simeq 1$ with negligible Δk .

To determine the change in index of refraction in an InTiO_3 accumulation layer, ellipsometry measurements were done on the $\text{Au}/\text{InTiO}_3/\text{SiO}_2/\text{Au}$ stack from 0 - 2.5 V in 0.5 V increments. By converting the changes in Ψ and Δ over the visible spectrum, the change in complex index within the accumulation layer was plotted in Figure 8.5. This plot shows that at $\lambda = 500 \text{ nm}$, $\Delta n_{\text{index}} = 0.4$, and at $\lambda = 800 \text{ nm}$, $\Delta n_{\text{index}} = 1.54$! This shift within the $\sim 5 \text{ nm}$ accumulation layer is a full order of magnitude larger than that seen in traditional electro-optic materials such as lithium niobate [11], and the thickness of this layer was determined using the minimization routine described above. In addition, it can be seen that there is a negligible Δk over the same region. The materials parameters extracted from ellipsometry for each voltage are shown in Table 8.1.

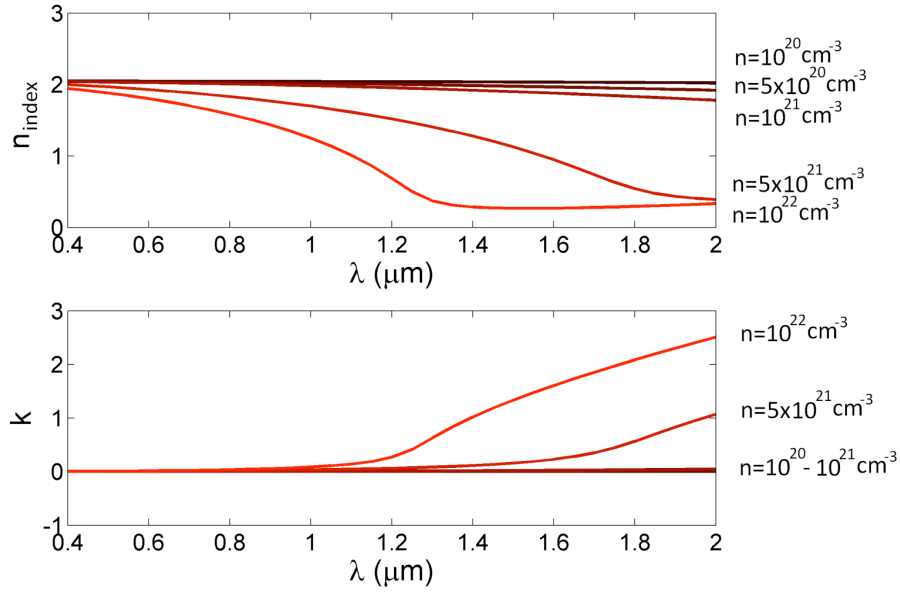


Figure 8.4. Complex index of refraction is plotted as a function of wavelength and carrier concentration within the InTiO₃ layer from $n = 10^{20} - 10^{22} \text{ cm}^{-3}$.

It should be noted that further studies of the layered structure revealed a number of additional features that indicate a plasma frequency shift from charge accumulation. First, this effect was not observed when a negative voltage was applied to the top, semi-transparent electrode and there was no longer an accumulation layer at the InTiO₃/SiO₂ interface. Second, when the thickness of the SiO₂ was doubled, the index shifting was only half as strong for a given voltage, i.e., when the capacitance is reduced. Third, the same amount of peak shifting was observed when the thickness of the InTiO₃ layer was increased or decreased, which implies that there was no change in the accumulation layer. Fourth, no peak shifting is observed unless the SiO₂ layer was present. Finally, with similar carrier concentrations, the same effect was also observed in InZnO₃. These results all indicate a plasma frequency shift from charge accumulation.

8.5 Mode Modulation in Metal/InTiO₃/Metal Waveguides

Based on fitting the ellipsometry data from Figure 8.5, the accumulation layer thickness was determined to be $\sim 5 \text{ nm}$. Mode profile modeling was done at $\lambda = 800 \text{ nm}$ for a MIM structure with 50 nm of SiO₂ and InTiO₃ between 300 nm of Au. This thickness was chosen so that the metal layers

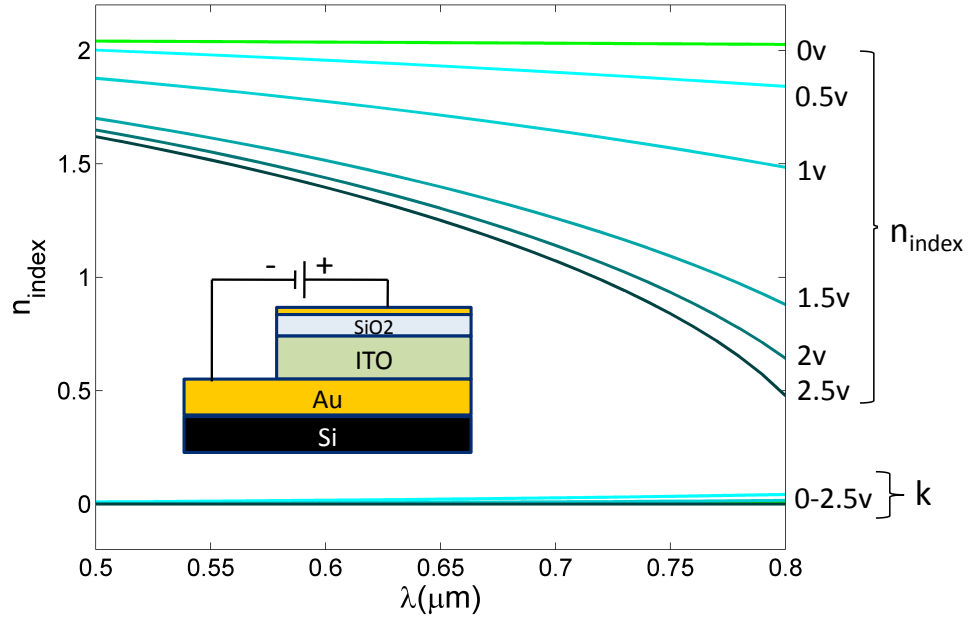


Figure 8.5. Complex index of refraction in and InTiO₃ accumulation layer as a function of voltage. Both n and k are plotted from $V = 0 - 2.5$ V.

would be optically opaque. Due to the high modal confinement within this MIM waveguide, driving the InTiO₃ into accumulation significantly modulates the plasmon modes within the structure.

Figure 8.6 shows optical mode profiles in the MIM waveguide with (right hand side) and without (left hand side) and applied electric field. The electron distribution across the device under an applied field was calculated by taking the peak concentration of $n_0 = 2.83 \times 10^{22} \text{ cm}^{-3}$ (Table 8.1) at the InTiO₃/SiO₂ interface, and plotting the charge distribution base on a solution to Poisson's equation given by:

$$N(x) = n_0 e^{\left(\frac{-x}{L}\right)} \quad (8.4)$$

where “L” is the 5 nm decay length obtained from ellipsometry. n_{index} was calculated for the 20, 1 nm layers next to the InTiO₃/SiO₂ interface using the Drude model. The mode profile was then calculated and plotted on right hand side of Figure 8.5. With no applied voltage, the mode has an effective index of 2.207. With an applied voltage of 2.5 V, the mode has an effective index of 2.108. This corresponds to a change of $\Delta n_{eff} \simeq 0.1$. In addition, with an applied field a significant portion of the optical mode resides at the SiO₂/InTiO₃ interface where the accumulation layer is present.

Table 8.1. Parameters used to model the InTiO₃ accumulation layer as a function of voltage.

Voltage	ϵ_{inf}	λ_p (nm)	ω_τ (THz)	N (cm ⁻³)	$\lambda_p\sqrt{\epsilon_{\text{inf}}}$ (nm)
0	4.21	2310	0.94	1×10^{20}	4.9
0.5	4.41	782	0.36	2.72×10^{21}	1.64
1	4.37	543	0.05	1.65×10^{22}	1.13
1.5	4.25	429	0.00	2.57×10^{22}	0.88
2	4.2	411	0.00	2.77×10^{22}	0.84
2.5	4.16	403	0.00	2.83×10^{22}	0.823

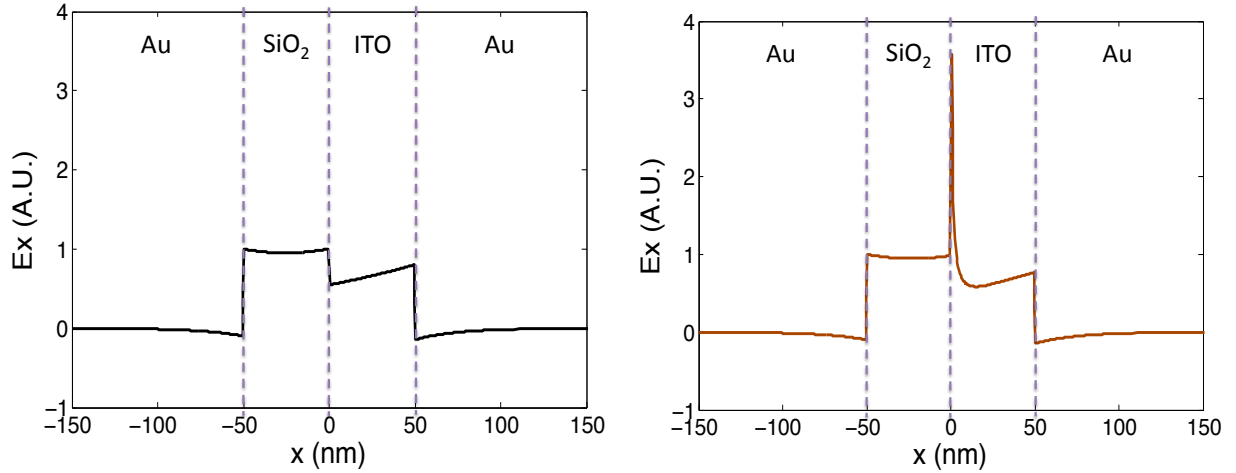


Figure 8.6. Optical Modes in a Au/InTiO₃/SiO₂/Au Waveguide with (right) and without (left) and applied electric field.

8.6 Conclusion

In this chapter we have shown that TCOs can be used as the active layer in a MIM waveguide, and are useful candidates for active plasmonic devices. We have shown that these materials can be deposited using RF magnetron sputtering and that they can achieve carrier concentrations on the order of $1 \times 10^{19} - 1 \times 10^{21} \text{ cm}^{-3}$. Drude model calculations showed that this placed the plasma frequency at infrared and visible frequencies. Spectroscopic ellipsometry as well as Drude modeling showed that with an applied field these structures can be driven into accumulation and the change in carrier concentration within this accumulation layer can shift the plasma frequency through the visible range of the spectrum. As a result, this produces shifts in the real part of the index of

refraction on the order of $\Delta n = 1$ while maintaining negligible loss within the material. This is a full order of magnitude larger shift that is seen in traditional electro-optic materials such as lithium niobate.

In this part of the thesis, we have shown two types of active plasmonic devices that operate based on modulating the carrier density distribution within a MIM waveguide. These devices have a wide range of flexibility in terms of their operating frequencies and speeds. Since these devices are all majority carrier based, their response time can potentially be even faster than traditional MOS structures. Additionally, their operating frequencies can be tuned across the visible, near, and mid-infrared frequencies by simply changing the device thickness (plasMOSStor in Chapter 7) or carrier density (TCOs in Chapter 8). This tunability combined with the fact that silicon and TCOs are already used in an enormous array of applications makes these technologies ideal candidates for integrated optical systems.

Chapter 9

Conclusions

In this thesis we have shown that MIM waveguides can be tuned over a wide range of visible and infrared frequencies by changing the device materials, dimensions, and carrier concentrations used. We have shown that by using ferroelectrics as the active material, these structures can be used as tunable color filters and using semiconducting layers, these structures can be used as electro-optic modulators.

Figure 9.1 shows the different parameters we have studied to affect the transmission spectrum through lithium niobate color filters. To the left of the waveguide, dispersion calculations plot the number of optical modes that a waveguide with a given thickness can support. Representative one- and two-dimensional mode profiles are shown within the cavity of the waveguide. The color bars to the right show that by varying the depth of the output slit into the dielectric layer, we can preferentially couple to the different photonic modes within the waveguide and change the color which is seen through the output slit. Further, by applying an electric field across these devices, we can change the refractive index of the lithium niobate and for certain combinations of slit spacing and slit depth, change the color coming through the output slit. The color bar above the waveguide shows that by varying the spacing between the input and output slits, we can couple to intensity maxima and minima of the different photonic modes that propagate through the device. Finally, initial results show that changing the dimensions of the input and output slits can increase the amount of transmitted light through the device by at least an order of magnitude. This is shown in the plot below the waveguide.

For semiconductors, namely the plasMOStor of Chapter 7, the device takes advantage of a charge accumulation effect at the Si/SiO₂ interface. Here the thickness of the device was chosen based on the dispersion calculations (top left and bottom right of Figure 9.2) so that along with the plasmonic mode, the waveguide would support exactly one photonic mode that was very near cutoff. Upon application of an electric field, the device was pushed into accumulation and the photonic mode no longer contributed significantly to the overall behavior of the device. This was confirmed

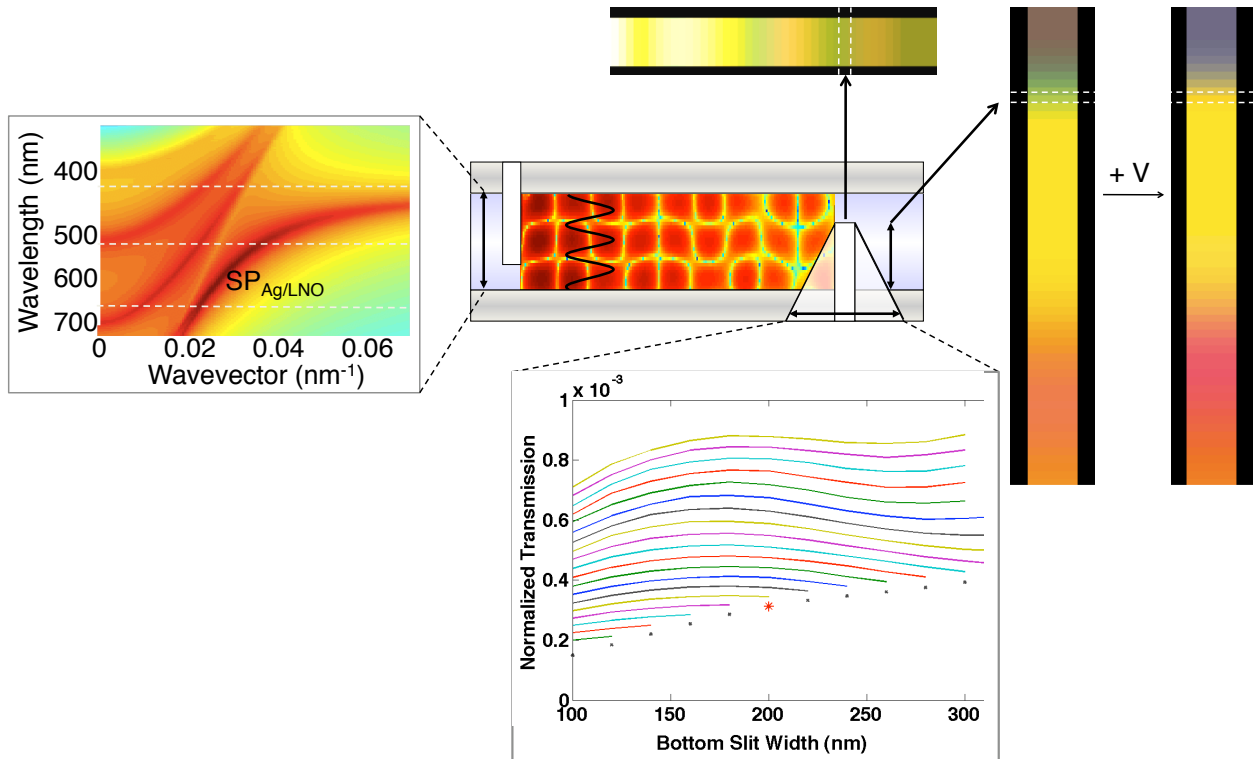


Figure 9.1. Methods for modifying the output of the MIM color filters included: varying the thickness (left); varying the depth of the output slit with and without an applied electric field (right); varying the separation between the input and output slits (top); varying the shape of the input and output slits (bottom). Representative one and two-dimension mode profiles are shown within the waveguide cavity.

using full field electromagnetic simulations which are shown in the cavity portion of the waveguide schematics (top and bottom center). Experimental measurements confirming these calculations are shown in the center of Figure 9.2, and by varying the spacing between the input and output slits, we couple to intensity maxima and minima of the optical mode(s) within the waveguide.

The above examples (as well as the TCO-based devices of Chapter 8) show the high degree of tunability associated with these structures. Although there are dozens of other parameters that could be varied with these devices, two that should be noted are: the number of input/output slits used and the strain within the films. In the future, one parameter that will be extensively studied for optimizing these devices will be using gratings to in-couple and out-couple the light. For broadband application, such as the color filters, this should prove to be a key component in improving total

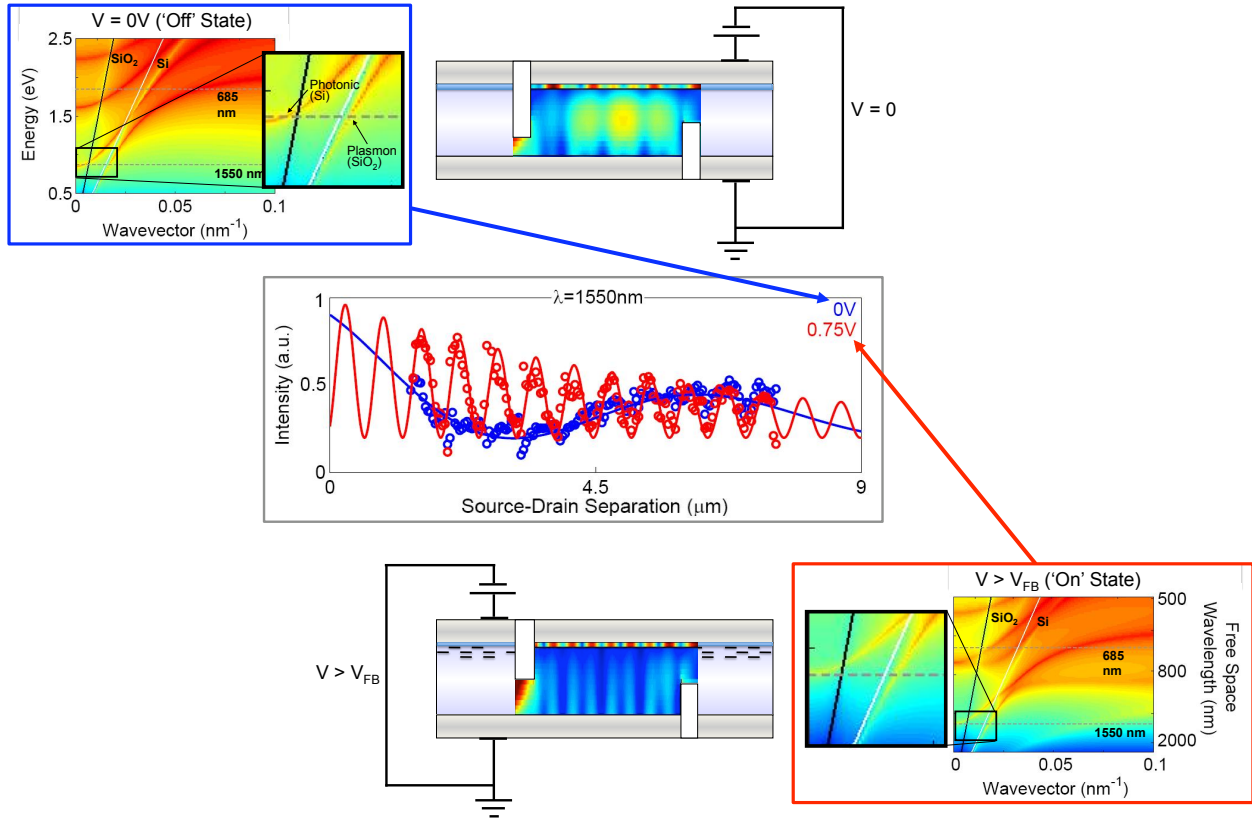


Figure 9.2. Methods for modifying the output of the MIM color filters included: varying the thickness (left); varying the depth of the output slit with and without an applied electric field (right); varying the separation between the input and output slits (top); varying the shape of the input and output slits (bottom). Representative one and two-dimension mode profiles are shown within the waveguide cavity.

power transmission and selectivity of these waveguides to individual wavelengths [85].

The issue of strain was briefly mentioned in regards to silicon in Chapter 7, Figure 7.2, and was a key component of device fabrication in Chapter 4. For the plasMostor, the strain was taken into account in calculating the effective Drude electron mass; however, the effects of strain on the refractive index were not used in any of the calculations or simulations. Similarly, for the lithium niobate color filters, Chapter 4 showed that the films must be in a state of compressive stress (but below a critical value) to form a coherent, transferred film; however, in the experiments and simulations, this was not factored into the refractive indices used (Appendix D). A more detailed analysis of the effect of strain on the distortion of the crystal structure and resulting

optical properties may provide new avenues for device applications [55].

Looking towards the future, these structures have already shown tunability across visible and infrared frequencies with both positive and negative indices of refraction [66]. This has been done using an extremely small subset of the materials at our disposal. One future avenue of exploration that should prove extremely promising is tuning the properties of the films themselves. This has already proved useful in the simple case of varying the doping concentration of the active layer; however, calculating the dispersive properties of the materials required for a given application could open up a wide range of future applications.

Part III

Appendicies

Appendix A

Dispersion Relations for Metal-Insulator-Metal Waveguides

In this appendix, we analyze the thin film dispersion relations for a metal-insulator-metal waveguide.¹ Both the transverse magnetic and transverse electric conditions will be considered. The geometry used for this derivation is shown in Figure A.1.

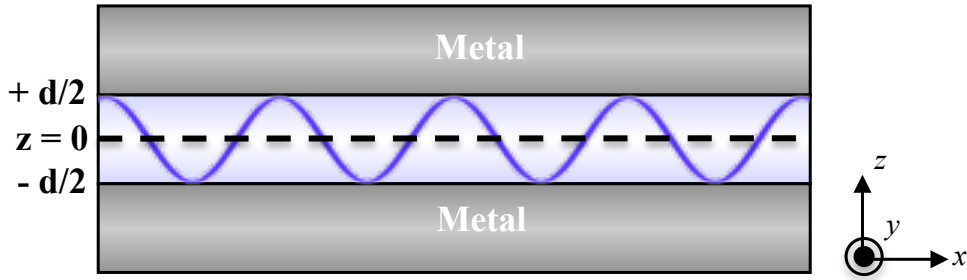


Figure A.1. The coordinate system used for the following three-layer derivation.

To begin, we first assume the form of the electric and magnetic fields given by:

$$\vec{E} = \vec{E}(z)e^{i(k_x x - \omega t)} \quad (\text{A.1a})$$

$$\vec{B} = \vec{B}(z)e^{i(k_x x - \omega t)} \quad (\text{A.1b})$$

where we assume there is no y-dependence in either field.

For this derivation, the curl can be written in its full form for the any vector \vec{U} as:

$$\nabla \times \vec{U} = \left[\frac{\partial U_z}{\partial y} - \frac{\partial U_y}{\partial z} \right] \hat{x} + \left[\frac{\partial U_x}{\partial z} - \frac{\partial U_z}{\partial x} \right] \hat{y} + \left[\frac{\partial U_y}{\partial x} - \frac{\partial U_x}{\partial y} \right] \hat{z} \quad (\text{A.2})$$

¹This appendix is based on texts by Professor Heinz Raether [97], Professor Stefan Maier [71], notes and discussions with Jennifer Dionne.

for for the curl components of \vec{U} in the \hat{x} , \hat{y} , and \hat{z} directions respectively.

We then plug the general form of the electric and magnetic fields into Maxwell's Equations. In the absence of space charge and currents, we have:

$$\nabla \cdot \vec{E} = 0 \quad (\text{A.3a})$$

$$\nabla \cdot \vec{B} = 0 \quad (\text{A.3b})$$

$$\nabla \times \vec{E} = -\frac{1}{c} \frac{\partial \vec{B}}{\partial t} \quad (\text{A.3c})$$

$$\nabla \times \vec{B} = \frac{1}{c} \epsilon_i(\omega) \frac{\partial \vec{E}}{\partial t} \quad (\text{A.3d})$$

We see that plugging (A.1a) and (A.1b) into (A.2) yields two sets of equations for either $\nabla \times \vec{E}$ or $\nabla \times \vec{B}$ which are given by:

$$\nabla \times \vec{E} :$$

$$\hat{x} : -\frac{\partial E_y}{\partial z} = \frac{i\omega}{c} B_x \quad (\text{A.4a})$$

$$\hat{y} : -\frac{\partial E_x}{\partial z} + ik_x E_z = \frac{i\omega}{c} B_y \quad (\text{A.4b})$$

$$\hat{z} : ik_x E_y = \frac{i\omega}{c} B_z \quad (\text{A.4c})$$

$$\nabla \times \vec{B} :$$

$$\hat{x} : -\frac{\partial B_y}{\partial z} = -\frac{i\omega}{c} \epsilon_i E_x \quad (\text{A.5a})$$

$$\hat{y} : \frac{\partial B_x}{\partial z} = -ik_x B_z = -\frac{i\omega}{c} \epsilon_i E_y \quad (\text{A.5b})$$

$$\hat{z} : -ik_x B_y = -\frac{i\omega}{c} \epsilon_i E_z \quad (\text{A.5c})$$

Initially we solve for generally for each component of \vec{E} and \vec{B} . Also note that the sets of solutions either consist of (E_y, B_x, B_z) or (E_x, E_z, B_y) . To simplify the general solution to solve for the set of transverse-magnetic (TM) modes, we can set $E_y = 0 \rightarrow B_x = B_z = 0$. To simplify the general solution to solve for the set of transverse-electric (TE) modes, we can set $B_y = 0 \rightarrow E_x = E_z = 0$.

A.1 The General Solution

We begin by solving for E_z . This is done by combining (A.4b) and (A.5c) :

$$\frac{\partial E_x}{\partial z} = -ik_x E_z = \frac{i\omega}{c} \left(-\frac{\omega}{ck_x} \right) \epsilon_i E_z \quad (\text{A.6})$$

with (A.5a) and (A.5c):

$$-\frac{\partial \left(\frac{\omega}{ck_x} \cdot \epsilon_i E_z \right)}{\partial z} = \frac{i\omega}{c} \epsilon_i E_x \quad (\text{A.7a})$$

$$\Rightarrow -\frac{\partial E_z}{\partial z} = ik_x E_x \quad (\text{A.7b})$$

which yields :

$$E_x = \frac{1}{k_x} \frac{\partial E_z}{\partial z} \quad (\text{A.8})$$

$$\frac{1}{k_x} \frac{\partial^2 E_z}{\partial z^2} - ik_x E_z = -\frac{i}{k_x} \left(\frac{\omega}{c} \right)^2 \epsilon_i E_z \quad (\text{A.9})$$

$$\frac{\partial^2 E_z}{\partial z^2} - k_x^2 E_z = -\left(\frac{\omega}{c} \right)^2 \epsilon_i E_z \quad (\text{A.10})$$

$$\frac{\partial^2 E_z}{\partial z^2} - \left(k_x^2 - \left(\frac{\omega}{c} \right)^2 \epsilon_i \right) E_z = 0 \quad (\text{A.11})$$

Here we use the definition: $k_{zi}^2 \equiv k_x^2 - \left(\frac{\omega}{c} \right)^2 \epsilon_i$ to yield:

$$\frac{\partial^2 E_z}{\partial z^2} - k_{zi}^2 E_z = 0 \rightarrow \lambda^2 - k_{zi}^2 = 0 \rightarrow \lambda = \pm k_{zi} \quad (\text{A.12})$$

$$\boxed{E_z = \mathcal{A}e^{k_{zi} \cdot z} \pm \mathcal{B}e^{-k_{zi} \cdot z}} \quad (\text{A.13})$$

Where the $A = B$ condition yields the even (symmetric) solutions and the $A = -B$ conditions yields the odd (anti-symmetric) solutions. To solve for E_x , we combine this result with that of (A.7b) to get:

$$\frac{\partial E_z}{\partial z} = -ik_x E_x = \mathcal{A}k_{zi}e^{k_{zi} \cdot z} \mp \mathcal{B}k_{zi}e^{-k_{zi} \cdot z} \quad (\text{A.14})$$

$$\boxed{E_x = -\frac{k_{zi}}{ik_x} \left(\mathcal{A}e^{k_{zi} \cdot z} \mp \mathcal{B}e^{-k_{zi} \cdot z} \right)} \quad (\text{A.15})$$

Finally, to solve for E_y , we combine (A.4a), (A.5b), and (A.4c) to obtain:

$$B_x = -\frac{c}{i\omega} \frac{\partial E_y}{\partial z} \quad (\text{A.16})$$

$$\frac{\partial B_x}{\partial z} - ik_x B_z = -\frac{i\omega}{c} \epsilon_i E_y \quad (\text{A.17})$$

$$\frac{\partial \left(-\frac{c}{i\omega} \cdot \frac{\partial E_y}{\partial z} \right)}{\partial z} - ik_x \left(\frac{ck_x}{\omega} \right) E_y = -\frac{i\omega}{c} \epsilon_i E_y \quad (\text{A.18})$$

$$-\frac{c}{i\omega} \cdot \frac{\partial^2 E_y}{\partial z^2} + \frac{c}{i\omega} \cdot k_x^2 E_y + \frac{i\omega}{c} \epsilon_i E_y = 0 \quad (\text{A.19})$$

$$\frac{\partial^2 E_y}{\partial z^2} - \left(k_x^2 + \left(\frac{i\omega}{c} \right)^2 \epsilon_i \right) E_y = 0 \quad (\text{A.20})$$

$$\frac{\partial^2 E_y}{\partial z^2} - \left(k_x^2 - \left(\frac{\omega}{c} \right)^2 \epsilon_i \right) E_y = 0 \quad (\text{A.21})$$

Here we use the definition $\beta_i^2 \equiv -k_x^2 + \left(\frac{\omega}{c} \right)^2 \epsilon_i \rightarrow \beta_i \equiv ik_{zi}$ to obtain:

$$\frac{\partial^2 E_y}{\partial z^2} + \beta_i^2 E_y = 0 \quad (\text{A.22})$$

$$\boxed{E_y = \mathcal{C}e^{i\beta_i \cdot z} \pm \mathcal{D}e^{-i\beta_i \cdot z} = \mathcal{C}e^{-k_{zi} \cdot z} \pm \mathcal{D}e^{k_{zi} \cdot z}} \quad (\text{A.23})$$

To obtain the z-component of \vec{B} , we use the fact that $ik_x E_y = \frac{i\omega}{c} B_z$ from (A.4c). It then follows that:

$$\boxed{B_z = \frac{ck_x}{\omega} \left(\mathcal{C}e^{i\beta_i \cdot z} \pm \mathcal{D}e^{-i\beta_i \cdot z} \right) = \frac{ck_x}{\omega} \left(\mathcal{C}e^{-k_{zi} \cdot z} \pm \mathcal{D}e^{k_{zi} \cdot z} \right)} \quad (\text{A.24})$$

and from (A.4a) it follows that:

$$-\frac{\partial E_y}{\partial z} = -\mathcal{C}\beta_i e^{i\beta_i \cdot z} \pm \mathcal{D}\beta_i e^{-i\beta_i \cdot z} = \frac{i\omega}{c} \cdot B_x \quad (\text{A.25})$$

$$\boxed{B_x = \frac{c}{\omega} \beta_i \left(-\mathcal{C}e^{i\beta_i \cdot z} \pm \mathcal{D}e^{-i\beta_i \cdot z} \right)} \quad (\text{A.26})$$

Finally, using the fact that $ik_x B_y = -\frac{i\omega}{c} \cdot \epsilon_i E_z$ from (A.5c) we obtain:

$$\boxed{B_y = -\frac{\omega}{c} \left(\frac{1}{k_x} \right) \epsilon_i \left(\mathcal{A}e^{k_{zi} \cdot z} \mp \mathcal{B}e^{-k_{zi} \cdot z} \right)} \quad (\text{A.27})$$

Now that we have each component of \vec{E} and \vec{B} , we introduce the boundary conditions necessary

for the metal-insulator-metal waveguide structure. We know that outside the waveguide, both \vec{E} and \vec{B} must decay to 0 as $z \rightarrow \infty$; however, within the waveguide, no such restrictions exist. For the general solution, we have $A = B$ for the even (symmetric) solutions and $A = -B$ for the odd (anti-symmetric) solutions. Combining these assumptions we get two sets of equations for the general solution for waves either inside, or outside of the layered, waveguide structure.

Inside the waveguide:

$$E_x = -\frac{k_{z1}}{ik_x} \left(e^{k_{z1}z} \mp e^{-k_{z1}z} \right) \quad (\text{A.28a})$$

$$E_y = e^{-k_{z1}z} \pm e^{k_{z1}z} \quad (\text{A.28b})$$

$$E_z = e^{k_{z1}z} \pm e^{-k_{z1}z} \quad (\text{A.28c})$$

$$B_x = \frac{ic}{\omega} k_{z1} \left(-e^{-k_{z1}z} \pm e^{k_{z1}z} \right) \quad (\text{A.28d})$$

$$B_y = -\frac{\omega}{c} \left(\frac{1}{k_x} \right) \epsilon_l \left(e^{k_{z1}z} \mp e^{-k_{z1}z} \right) \quad (\text{A.28e})$$

$$B_z = \frac{ck_x}{\omega} \left(e^{-k_{z1}z} \pm e^{k_{z1}z} \right) \quad (\text{A.28f})$$

Outside the waveguide:

$$E_x = -\frac{k_{z2}}{ik_x} \left(\mp \mathcal{B} e^{-k_{z2}z} \right) \quad (\text{A.29a})$$

$$E_y = \mathcal{C} e^{-k_{z2}z} \quad (\text{A.29b})$$

$$E_z = \pm \mathcal{B} e^{-k_{z2}z} \quad (\text{A.29c})$$

$$B_x = -\frac{ic}{\omega} k_{z2} \mathcal{C} e^{-k_{z2}z} \quad (\text{A.29d})$$

$$B_y = -\frac{\omega}{c} \left(\frac{1}{k_x} \right) \epsilon_l \left(\mp \mathcal{B} e^{-k_{z2}z} \right) \quad (\text{A.29e})$$

$$B_z = \frac{ck_x}{\omega} \mathcal{C} e^{-k_{z2}z} \quad (\text{A.29f})$$

A.2 Boundary Conditions

For all solutions, we assume that:

- E_x and D_z are continuous at $z = \pm \frac{d}{2}$

- E_y is continuous at $z = \pm \frac{d}{2}$
- B_z is continuous at $z = \pm \frac{d}{2}$
- $\frac{1}{\mu} B_x$ is continuous at $z = \pm \frac{d}{2}$
- $\frac{1}{\mu} B_y$ is continuous at $z = \pm \frac{d}{2}$

A.2.1 E_x and D_z are continuous:

From (A.28a) and (A.29a) we have:

$$\frac{ik_{z1}}{k_x} \left(e^{k_{z1}z} \mp e^{-k_{z1}z} \right) = \pm \frac{k_{z2}}{ik_x} \left(\mathcal{B}e^{-k_{z2}z} \right) \quad (\text{A.30})$$

From (A.28c) and (A.29c) we have:

$$\epsilon_1 \left(e^{k_{z1}z} \pm e^{-k_{z1}z} \right) = \pm \epsilon_2 \left(\mathcal{B}e^{-k_{z2}z} \right) \quad (\text{A.31})$$

and combining the two we derive:

$$ik_{z1} \left(e^{k_{z1}z} \mp e^{-k_{z1}z} \right) = \frac{k_{z2}}{i} \left(\frac{\epsilon_1}{\epsilon_2} \right) \left(e^{k_{z1}z} \pm e^{-k_{z1}z} \right) \quad (\text{A.32})$$

$$- \epsilon_2 k_{z1} \left(e^{k_{z1}z} \mp e^{-k_{z1}z} \right) = \epsilon_1 k_{z2} \left(e^{k_{z1}z} \pm e^{-k_{z1}z} \right) \quad (\text{A.33})$$

$$- \epsilon_2 k_{z1} = \epsilon_1 k_{z2} \left\{ \begin{array}{l} \coth(k_{z1}d/2) \\ \tanh(k_{z1}d/2) \end{array} \right\} \quad (\text{A.34})$$

which yields the transverse-magnetic dispersion relation:

$$\boxed{\epsilon_1 k_{z2} + \epsilon_2 k_{z1} \left\{ \begin{array}{l} \coth(k_{z1}d/2) \\ \tanh(k_{z1}d/2) \end{array} \right\} = 0} \quad (\text{A.35})$$

Here, the “coth” function represents the symmetric plasmon modes and the “tanh” function represents the antisymmetric modes.

A.2.2 E_y is continuous:

From (A.28b) and (A.29b) we have:

$$e^{-k_{z1}z} \pm e^{k_{z1}z} = \mathcal{C}e^{-k_{z2}z} \quad (\text{A.36})$$

which yields:

$$\boxed{\mathcal{C} = e^{k_{z2}d/2} \left(e^{-k_{z1}d/2} \pm e^{k_{z1}d/2} \right)} \quad (\text{A.37})$$

A.2.3 H_z , H_y , and B_z are continuous:

From (A.28e) and (A.29e) we have:

$$-\frac{\omega}{c} \left(\frac{1}{k_x} \frac{\epsilon_1}{\mu_1} \right) \left(e^{k_{z1}d/2} \mp e^{-k_{z1}d/2} \right) = -\frac{\omega}{c} \left(\frac{1}{k_x} \frac{\epsilon_2}{\mu_2} \right) \left(\mp \mathcal{B}e^{-k_{z2}d/2} \right) \quad (\text{A.38})$$

$$\epsilon_1 \mu_2 \left(e^{k_{z1}d/2} \mp e^{-k_{z1}d/2} \right) = \epsilon_2 \mu_1 \left(\mp \mathcal{B}e^{-k_{z2}d/2} \right) \quad (\text{A.39})$$

which yields:

$$\boxed{\mathcal{B} = \frac{\epsilon_1 \mu_2}{\epsilon_2 \mu_1} e^{k_{z2}d/2} \left(e^{k_{z1}d/2} \mp e^{-k_{z1}d/2} \right)} \quad (\text{A.40})$$

From (A.28f) and (A.29f) we have:

$$\frac{ck_x}{\omega} \left(e^{-k_{z1}d/2} \pm e^{k_{z1}d/2} \right) = \frac{ck_x}{\omega} \mathcal{C}e^{-k_{z2}d/2} \quad (\text{A.41})$$

$$\mathcal{C} = e^{k_{z2}d/2} \left(e^{-k_{z1}d/2} \pm e^{k_{z1}d/2} \right) \quad (\text{A.42})$$

From (A.28d) and (A.29d) we have:

$$\frac{ick_{z1}}{\omega \mu_1} \left(-e^{-k_{z1}d/2} \pm e^{k_{z1}d/2} \right) = -\frac{ick_{z2}}{\omega \mu_2} \mathcal{C}e^{-k_{z2}z} \quad (\text{A.43})$$

$$\mathcal{C} = -\frac{k_{z1}}{k_{z2}} \frac{\mu_2}{\mu_1} e^{k_{z2}d/2} \left(-e^{-k_{z1}d/2} \pm e^{k_{z1}d/2} \right) \quad (\text{A.44})$$

From this we can infer that:

$$-\frac{k_{z1}}{k_{z2}} \left(-e^{-k_{z1}d/2} \pm e^{k_{z1}d/2} \right) = e^{-k_{z1}d/2} \pm e^{k_{z1}d/2} \quad (\text{A.45})$$

$$\frac{k_{z1}\mu_2}{k_{z2}\mu_1} \left(e^{-k_{z1}d/2} \mp e^{k_{z1}d/2} \right) = \left(e^{-k_{z1}d/2} \pm e^{k_{z1}d/2} \right) \quad (\text{A.46})$$

$$\mp k_{z1}\mu_2 \left(e^{k_{z1}d/2} \mp e^{-k_{z1}d/2} \right) = \pm k_{z2}\mu_1 \left(e^{k_{z1}d/2} \pm e^{-k_{z1}d/2} \right) \quad (\text{A.47})$$

$$\mp k_{z1}\mu_2 = \pm k_{z2}\mu_1 \left\{ \begin{array}{l} \coth(k_{z1}d/2) \\ \tanh(k_{z1}d/2) \end{array} \right\} \quad (\text{A.48})$$

which yields the transverse-electric dispersion relation:

$$\boxed{\pm\mu_1 k_{z2} \pm \mu_2 k_{z1} \left\{ \begin{array}{l} \tanh(k_{z1}d/2) \\ \coth(k_{z1}d/2) \end{array} \right\} = 0} \quad (\text{A.49})$$

Thus, by comparing (A.35) and (A.49) we see that the sets of solutions either consist of (E_y, B_x, B_z) or (E_x, E_z, B_y) as was stated at the beginning of the Appendix. From here it can be shown, [71], that there are no non-zero modal solutions to the transverse-electric modes operating within this structure. As a result, we can state that surface plasmon polaritons are strictly transverse-magnetic.

Appendix B

Tensor Representation of Crystals

B.1 Tensor Notation

Many of the physical properties that we study in nature are oftentimes reduced to simple, linear relationships. For example, the conductivity within a material is usually written as:

$$j = \sigma E \tag{B.1}$$

where “ j ” is the current density, σ is the conductivity, and “ E ” is the electric field. However, for a complete analysis of real materials in three-dimensions, these simple, one-dimensional representations are inadequate. Many of the properties in nature (the electro-optic effect, piezoelectricity, ferroelectricity, index of refraction, conductivity, etc.) require a full, three-dimensional representation of the response of materials to external forces and fields. This requires a tensorial representation of the physical properties of crystals [79]. Going back to the case of conductivity, an accurate representation of this property is given by:

$$\begin{bmatrix} j_1 \\ j_2 \\ j_3 \end{bmatrix} = \begin{bmatrix} \sigma_{11} & \sigma_{12} & \sigma_{13} \\ \sigma_{21} & \sigma_{22} & \sigma_{23} \\ \sigma_{31} & \sigma_{32} & \sigma_{33} \end{bmatrix} \begin{bmatrix} E_1 \\ E_2 \\ E_3 \end{bmatrix} \tag{B.2}$$

where $\sigma_{ab} \equiv$ conductivity in the “ a ” direction of a material from a field in the “ b ” direction. Further, the matrices can be represented by:

$$j_i = \sum_{h=1}^3 \sigma_{ih} E_h \rightarrow j_i = \sigma_{ih} E_h \tag{B.3}$$

This is the Einstein Summation Notation for a second-rank tensor and will be used throughout

the rest of this thesis. Taking this one step further, representing piezoelectricity in a crystal requires a third-rank tensor. As was mentioned in Section 2.2.2, the direct piezoelectric effect occurs when a stress is applied to the crystal and an electric field results. The converse piezoelectric effect occurs when an electric field is applied to the crystal and a strain results. This effect is represented by:

$$P_i = d_{ijk}\sigma_{jk} \quad (\text{B.4})$$

where P is the polarization of the crystal, d is the piezoelectric coefficient of the crystal, and σ is the stress applied to the crystal. The polarization of the crystal is given by P_1 , P_2 , and P_3 in the x-, y-, and z-directions respectively, and there is a corresponding 3x3 σ -tensor associated with each polarization. As a result, this gives the third-rank tensor:

$$P_1 = \begin{bmatrix} d_{111}\sigma_{11} & d_{112}\sigma_{12} & d_{113}\sigma_{13} \\ d_{121}\sigma_{21} & d_{122}\sigma_{22} & d_{123}\sigma_{23} \\ d_{131}\sigma_{31} & d_{132}\sigma_{32} & d_{133}\sigma_{33} \end{bmatrix} \quad (\text{B.5})$$

$$P_2 = \begin{bmatrix} d_{211}\sigma_{11} & d_{212}\sigma_{12} & d_{213}\sigma_{13} \\ d_{221}\sigma_{21} & d_{222}\sigma_{22} & d_{223}\sigma_{23} \\ d_{231}\sigma_{31} & d_{232}\sigma_{32} & d_{233}\sigma_{33} \end{bmatrix} \quad (\text{B.6})$$

$$P_3 = \begin{bmatrix} d_{311}\sigma_{11} & d_{312}\sigma_{12} & d_{313}\sigma_{13} \\ d_{321}\sigma_{21} & d_{322}\sigma_{22} & d_{323}\sigma_{23} \\ d_{331}\sigma_{31} & d_{332}\sigma_{32} & d_{333}\sigma_{33} \end{bmatrix} \quad (\text{B.7})$$

which are the 1st, 2nd, and 3rd layers of the tensor.

This approach utilizes the full tensorial representation of crystal properties; however, in many cases, there are a significant number of these elements that are either equivalent or are zero. To that end, we can reduce the number of elements in the previous matrices as follows. Because of the fact that, for a given polarization these tensors are symmetric, we can reduce the number of elements in each layer of the tensor by half. For each layer of the previous tensor we have:

$$\begin{bmatrix} d_{11} & d_{12} & d_{13} \\ d_{21} & d_{22} & d_{23} \\ d_{31} & d_{32} & d_{33} \end{bmatrix} \rightarrow \begin{bmatrix} d_{11} & \frac{1}{2}d_{16} & \frac{1}{2}d_{15} \\ & d_{12} & \frac{1}{2}d_{14} \\ & & d_{13} \end{bmatrix} \quad (\text{B.8})$$

and using this conversion from tensor notation to matrix notation, we can also reduce the stress matrix:

$$(B.9) \quad \begin{bmatrix} \sigma_{11} & \sigma_{12} & \sigma_{13} \\ \sigma_{21} & \sigma_{22} & \sigma_{23} \\ \sigma_{31} & \sigma_{32} & \sigma_{33} \end{bmatrix} \rightarrow \begin{bmatrix} \sigma_1 & \sigma_6 & \sigma_5 \\ \sigma_6 & \sigma_2 & \sigma_4 \\ \sigma_5 & \sigma_4 & \sigma_3 \end{bmatrix}$$

At this point, we can represent the polarization of the crystal in the x-direction as: $P_1 = d_{11}\sigma_1 + d_{12}\sigma_2 + d_{13}\sigma_3 + d_{14}\sigma_4 + d_{15}\sigma_5 + d_{16}\sigma_6$. Using this notation and putting each layer of the tensor in a row, we can more concisely write the equations for the direct (B.10) and converse (B.11) piezoelectric effects as:

$$(B.10) \quad \begin{array}{c|cccccc} & \sigma_1 & \sigma_2 & \sigma_3 & \sigma_4 & \sigma_5 & \sigma_6 \\ \hline P_1 & d_{11} & d_{12} & d_{13} & d_{14} & d_{15} & d_{16} \\ P_2 & d_{21} & d_{22} & d_{23} & d_{24} & d_{25} & d_{26} \\ P_3 & d_{31} & d_{32} & d_{33} & d_{34} & d_{35} & d_{36} \end{array}$$

$$(B.11) \quad \begin{array}{c|cccccc} & \epsilon_1 & \epsilon_2 & \epsilon_3 & \epsilon_4 & \epsilon_5 & \epsilon_6 \\ \hline E_1 & d_{11} & d_{12} & d_{13} & d_{14} & d_{15} & d_{16} \\ E_2 & d_{21} & d_{22} & d_{23} & d_{24} & d_{25} & d_{26} \\ E_3 & d_{31} & d_{32} & d_{33} & d_{34} & d_{35} & d_{36} \end{array}$$

This is the traditional way that these tensors are represented. At this point, we can take advantage of Newmann’s Principle which states that:

“The symmetry elements of any physical property of a crystal must include the symmetry elements of the crystal.”

Using this fact we can reduce the number of non-zero elements in the matrix. As an example, we take the case of the ABO_3 perovskites discussed in Section 2.2.2. For clarity, we will temporarily revert back to the expanded tensor form to illustrate the process.

$$(B.12) \quad \begin{bmatrix} d_{111} & d_{112} & d_{113} \\ & d_{122} & d_{123} \\ & & d_{133} \end{bmatrix} \begin{bmatrix} d_{211} & d_{212} & d_{213} \\ & d_{222} & d_{223} \\ & & d_{233} \end{bmatrix} \begin{bmatrix} d_{311} & d_{312} & d_{313} \\ & d_{322} & d_{323} \\ & & d_{333} \end{bmatrix}$$

In the tetragonal 4mm symmetry group, we have: 4 mirror planes and a 4-fold rotation axis. For the x mirror plane:

$$1 \rightarrow 1, 2 \rightarrow -2, 3 \rightarrow 3$$

which means that any element with an odd number of “2’s” will not be invariant under the transformation. Therefore, these elements are necessarily zero. Similarly, for the y mirror plane:

$$1 \rightarrow -1, 2 \rightarrow 2, 3 \rightarrow 3$$

which means that any element with an odd number of “1’s” will not be invariant under the transformation. For the xy mirror plane

$$1 \rightarrow 2, 2 \rightarrow 1, 3 \rightarrow 3$$

which means $d_{311} = d_{322}$ and $d_{113} = d_{223}$. The resulting tensor has the form:

$$\begin{bmatrix} 0 & 0 & d_{113} \\ 0 & 0 & 0 \\ 0 & 0 & 0 \end{bmatrix} \begin{bmatrix} 0 & 0 & 0 \\ 0 & 0 & d_{223} \\ 0 & 0 & 0 \end{bmatrix} \begin{bmatrix} d_{311} & 0 & 0 \\ 0 & d_{322} & 0 \\ 0 & 0 & d_{333} \end{bmatrix} \quad (\text{B.13})$$

which when returned to the reduced form gives:

$$\begin{bmatrix} 0 & 0 & 0 & 0 & d_{15} & 0 \\ 0 & 0 & 0 & d_{15} & 0 & 0 \\ d_{31} & d_{31} & d_{33} & 0 & 0 & 0 \end{bmatrix} \quad (\text{B.14})$$

B.2 Orientation Effects of Crystal Properties

The reduced form of a crystal’s tensor gives the materials direct and shear components of a response to an applied stimulus. The process can be taken one step further. By choosing a reference orientation (here we will pick the \hat{z} or d_{33} direction), the response of a crystal can be calculated and mapped out for every possible orientation of applied stimulus. To map out the piezoresponse of a 4mm crystal, the angles between each of the non-zero piezoresponse coefficients and the applied electric field can be calculated in polar coordinates [103]. By summing these five terms together

we obtain the equation:

$$d_{33}^* = (d_{31} + d_{15})\cos\theta\sin^2\theta + d_{33}\cos^3\theta \quad (\text{B.15})$$

This is plotted for barium titanate in Figure B.1.

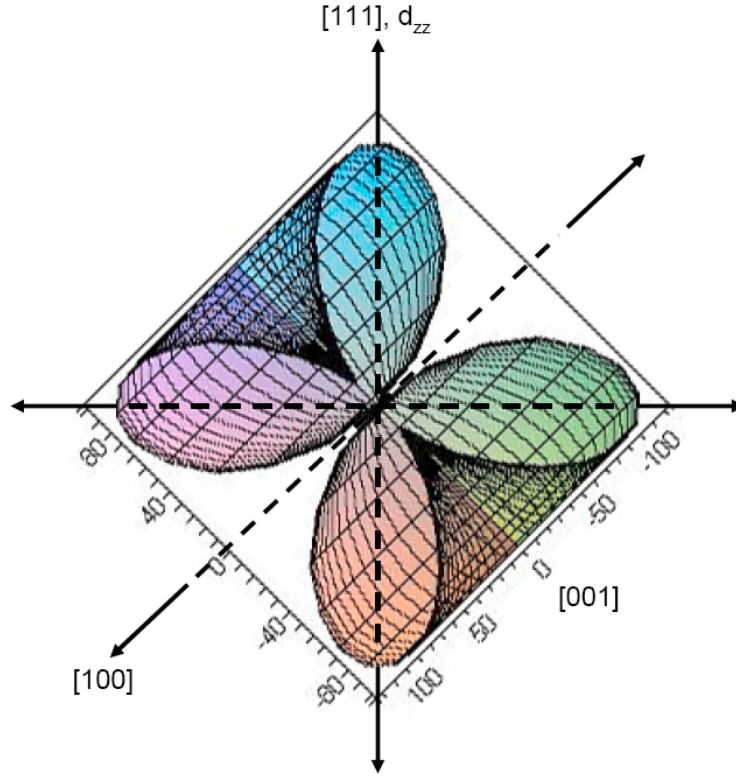


Figure B.1. Three-dimensional piezoresponse plot for barium titanate. The different orientations are labeled on their respective axes, and intensity of piezoresponse is represented as distance from the origin. The scale on the axes is pm/V.

Appendix C

Spectroscopic Ellipsometry

Spectroscopic ellipsometry is a thin film optical characterization technique that sends s- and p-linearly polarized light onto layered thin films and measures the light that is reflected back. By doing so, the technique is able to determine the thickness of the individual layers as well as their complex optical constants, $\tilde{n} = n + i\kappa$.

More specifically, the s- and p-polarized light reflects from each layer in the film stack based on the Fresnel equations. For a single layer, these are given as:

$$R_{s,p} = \frac{r_{s,p}^{12} + r_{s,p}^{23} e^{-\beta}}{1 + r_{s,p}^{12} r_{s,p}^{23} e^{-\beta}} \quad (\text{C.1})$$

where $r_{s,p}^{ab}$ corresponds to the reflection coefficient from the “ab” interface for s- and p-polarized light, respectively. To relate these coefficients to the complex index of refraction for the layer, $\tilde{n} = n + i\kappa$, we look at β :

$$\beta = 2\pi \left(\frac{d}{\lambda} \right) \tilde{n}_2(\lambda) \cos(\phi_2) \quad (\text{C.2})$$

where d is the thickness of layer 2, λ is the wavelength at which the measurement was taken, $n_2(\lambda)$ is the complex index of refraction of layer 2 at λ , and ϕ is the phase shift that results from the s- or p-polarized light propagating through the layer.

By measuring $R_{s,p}$ and β , as well as the change in phase between the incident light and reflected light for both polarizations, two parameters can be calculated:

$$\Psi = \left| \frac{R_p}{R_s} \right| \quad (\text{C.3})$$

$$\Delta = \delta_1 - \delta_2 \quad (\text{C.4})$$

where $\delta_{1,2}$ are the differences in phase between the s- and p-polarized light before (1) and after (2) propagating through the layer.

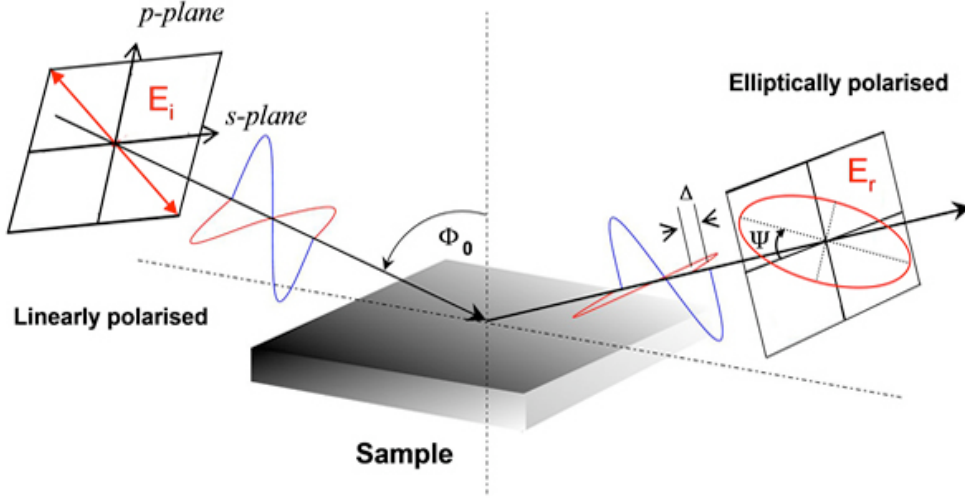


Figure C.1. Shown here is layout for spectroscopic ellipsometry [4] which shows: both s- and p-polarized light incident on the sample surface, the angle of incidence, ϕ ; the difference in phase differences, Δ ; and the ratio of R_p and R_s ; Ψ .

Each layer in the film stack is mathematically represented by an appropriate model which relates the thickness and dielectric constants of the material. The model for the entire stack is plotted against the measured Ψ and Δ data. By measuring these values over a range of wavelengths and angles of incidence, a minimization routine is able to fit the experimental data to the models. Once an acceptable fit is achieved, the models for each layer can be used to extract the dispersion of the materials being studied: $\tilde{n}(\lambda) = n(\lambda) + i\kappa(\lambda)$.

As an example, ellipsometry data for lithium niobate that was used in this thesis was modeled using a Cauchy layer fit which is an empirical model for ellipsometry data. As was stated in Chapter 6, the data was fit from 400 - 700 nm using:

$$n(\lambda) = n_0 + C_0 \frac{n_1}{\lambda^2} + C_1 \frac{n_2}{\lambda^4} \quad (\text{C.5})$$

$$k(\lambda) = k_0 + C_0 \frac{k_1}{\lambda^2} + C_1 \frac{k_2}{\lambda^4} \quad (\text{C.6})$$

where $n_0 = 2.093$, $n_1 = 305.9$, $n_2 = 52.9$, $k_0 = 0.02$, $k_1 = 24.541$, $k_2 = 23.276$, $C_0 = 10^2$,

$C_1 = 10^7$, and λ is given in nm.

In contrast, the indium tin oxide discussed in Chapter 8 was modeled using the drude model which is a physical model given by:

$$\epsilon = \epsilon_\infty - \frac{\omega_p^2}{\omega^2 + i\omega\omega_\tau} \quad (\text{C.7})$$

$$\omega_p = \frac{ne^2}{\epsilon m^*} \quad (\text{C.8})$$

where the parameters $m^* = 0.45m_e$, $\epsilon_\infty = 4.2$, $\tau = 1 \text{ fs}$, $\lambda_p = 2300 \text{ nm}$, and $n = 4 \times 10^{20} \text{ cm}^{-3}$ were extracted using ellipsometry. Shown in Figure C.2 is an example of the Ψ and Δ data that was taken for a thin film stack of Au/InTiO₃/SiO₂/Au across the visible spectrum with and without an applied voltage.

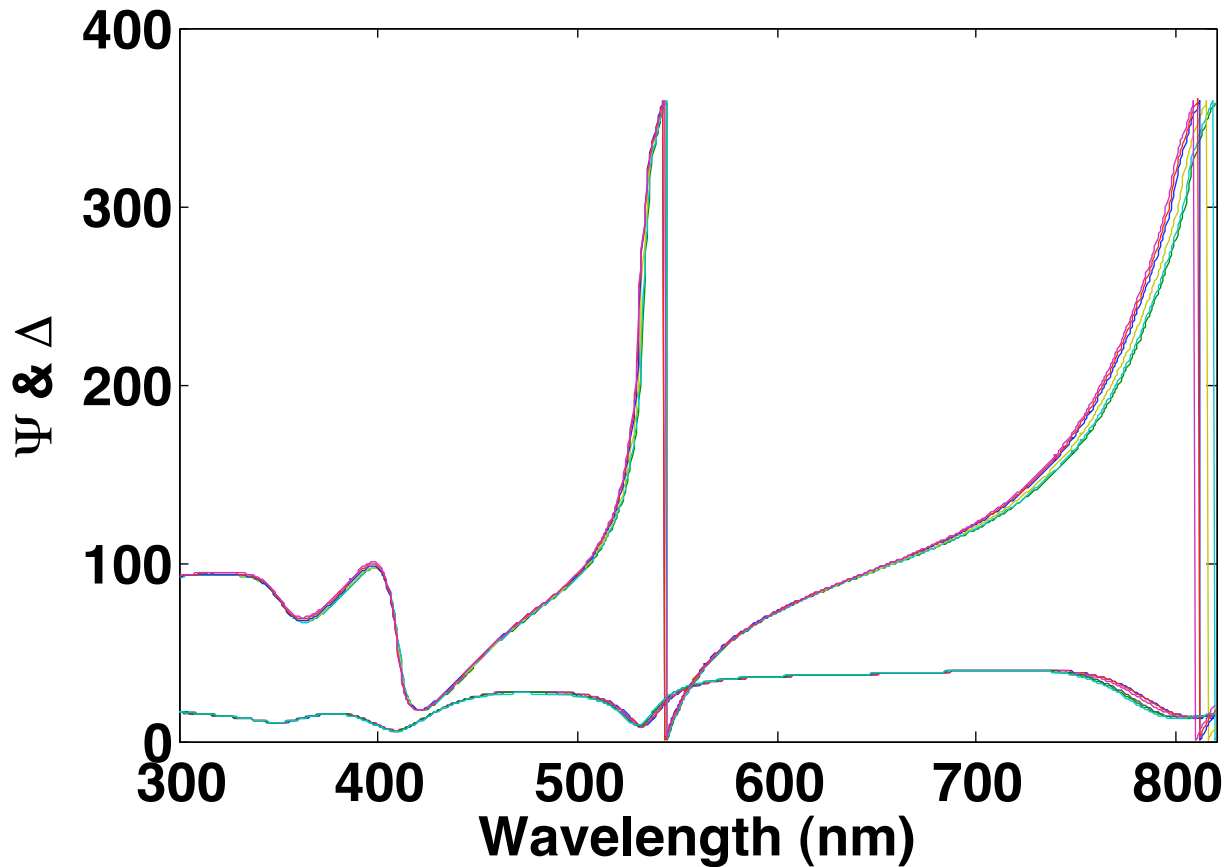


Figure C.2. The ellipsometry measurements of the thin film stack shown in Figure 8.2.

Appendix D

Lithium Niobate Optical Properties

The following table lists the optical properties used for the finite-difference time-domain simulations of lithium niobate color filtering used in Chapter 6. The data was obtained through a combination of spectroscopic ellipsometry (Appendix C) of x-cut lithium niobate single crystal samples [3], and from Reference [11].

The experimental lithium niobate data was fit from 400 - 700 nm as a Cauchy layer given by:

$$n(\lambda) = n_0 + C_0 \frac{n_1}{\lambda^2} + C_1 \frac{n_2}{\lambda^4} \quad (\text{D.1})$$

$$k(\lambda) = k_0 + C_0 \frac{k_1}{\lambda^2} + C_1 \frac{k_2}{\lambda^4} \quad (\text{D.2})$$

where $n_0 = 2.093$, $n_1 = 305.9$, $n_2 = 52.9$, $k_0 = 0.02$, $k_1 = 24.541$, $k_2 = 23.276$, $C_0 = 10^2$, $C_1 = 10^7$, and λ is given in nm.

For lithium niobate with and without an applied electric field, the imaginary part of the index of refraction was kept constant.

λ (nm)	index (V = 0)	index (V = Applied)	k
401.02526	2.295547794937	2.4811	0.042641086753
403.42627	2.292915889071	2.4724	0.042479604977
405.22704	2.290220480056	2.4662	0.041942041808
407.0278	2.286990340738	2.4604	0.042214882671
409.42881	2.286026168866	2.4529	0.041374350774
411.22958	2.285425935878	2.4477	0.041877079415
413.03034	2.282431581504	2.4427	0.041445679342

λ (nm)	index ($V = 0$)	index ($V = \text{Applied}$)	k
415.43136	2.279966319221	2.4364	0.040676174432
417.23212	2.277795129075	2.4319	0.040615512823
419.03288	2.278910830714	2.4277	0.041104888292
421.4339	2.274188880289	2.4224	0.041134279634
423.23466	2.273746292495	2.4187	0.040516113998
425.03542	2.271451574133	2.4152	0.040462235188
427.43644	2.269774672465	2.4108	0.040339049254
429.2372	2.268345389284	2.4077	0.04000318701
431.03796	2.266298826854	2.4048	0.039411300994
433.43898	2.263197744359	2.4011	0.03928415182
435.23974	2.261341755004	2.3986	0.039384665092
437.05143	2.259935128628	2.3961	0.038946835023
439.47428	2.25818164547	2.3931	0.038986820125
441.29143	2.255412782436	2.391	0.038574236313
443.10857	2.256097845995	2.3889	0.038248913181
445.53143	2.255317977897	2.3864	0.038940901467
447.34857	2.254592989005	2.3846	0.038639297794
449.16571	2.252856467425	2.3829	0.038025880732
451.58857	2.249629378184	2.3807	0.03760654238
453.40571	2.250908699316	2.3792	0.038182430589
455.22286	2.246089233332	2.3777	0.037111405325
457.04	2.244748068969	2.3763	0.037353289677
459.46286	2.241808351136	2.3744	0.036764937843
461.28	2.240764124125	2.373	0.036860061753
463.09714	2.2379256399	2.3717	0.036035534084
465.52	2.239242050242	2.3699	0.036465321264

λ (nm)	index ($V = 0$)	index ($V = \text{Applied}$)	k
467.33715	2.237030323115	2.3686	0.036207846931
469.15429	2.237964714116	2.3672	0.035898843425
471.57715	2.234177505899	2.3654	0.035854047051
473.39429	2.2335359336	2.3641	0.035935482701
475.21143	2.231849223515	2.3627	0.035309255449
477.02858	2.230681746645	2.3614	0.035567273397
479.45143	2.230494398356	2.3596	0.035034845206
481.26858	2.229035773325	2.3583	0.034584633557
483.08572	2.226294411702	2.357	0.034935406597
485.50858	2.227499217249	2.3552	0.034634480114
487.32572	2.223739802698	2.3538	0.034870354576
489.14286	2.225152475139	2.3524	0.034839664448
491.56572	2.223450090601	2.3506	0.033643944321
493.38286	2.220418051273	2.3493	0.034480765961
495.20001	2.222105572746	2.3479	0.034054848208
497.01715	2.221531576874	2.3466	0.034379173006
499.44001	2.219402852086	2.345	0.033407835672
501.25715	2.218389248616	2.3438	0.033764955447
503.07429	2.219626095105	2.3427	0.03337352644
505.49715	2.216619003587	2.3414	0.032779262417
507.3143	2.217686599371	2.3404	0.032838448584
509.13144	2.214931089318	2.3395	0.033552394516
511.5543	2.211594081761	2.3384	0.032089013321
513.37144	2.212054998039	2.3375	0.032534282952
515.18858	2.211793191858	2.3367	0.032691289963
517.00573	2.21277231374	2.3358	0.032032312494

λ (nm)	index ($V = 0$)	index ($V = \text{Applied}$)	k
519.42858	2.212475258751	2.3345	0.031602194739
521.24573	2.210164496519	2.3336	0.032351716416
523.06287	2.209180177114	2.3326	0.03197502082
525.48573	2.206979432532	2.3314	0.031814076593
527.30287	2.208212917783	2.3304	0.031299248444
529.12001	2.205797756892	2.3295	0.031143985951
531.54287	2.202749330335	2.3282	0.031820874302
533.36001	2.204151669529	2.3273	0.031504426013
535.17716	2.204431199275	2.3264	0.031405280968
537.60002	2.200727780531	2.3252	0.030920951346
539.41716	2.203431984846	2.3243	0.031677409181
541.2343	2.204941152164	2.3234	0.031016980409
543.05145	2.201577706581	2.3225	0.030548518703
545.4743	2.198392565327	2.3214	0.031171522965
547.29832	2.198461211603	2.3206	0.031031469631
549.12577	2.199752990946	2.3197	0.03076527891
551.56236	2.196946981393	2.3186	0.030139540608
553.38981	2.195113463733	2.3178	0.03083848737
555.21726	2.197399768609	2.317	0.030550105186
557.04471	2.197071876184	2.3162	0.031098167226
559.48131	2.194649490887	2.3152	0.029370110902
561.30876	2.195204118874	2.3144	0.030498374513
563.13621	2.196700909541	2.3137	0.031272109273
565.57281	2.192231120891	2.3127	0.029781594097
567.40025	2.190097861767	2.312	0.029801134882
569.2277	2.189152495703	2.3112	0.02998194035

λ (nm)	index ($V = 0$)	index ($V = \text{Applied}$)	k
571.05515	2.192003324649	2.3105	0.029301143845
573.49175	2.184366555474	2.3096	0.031241157331
575.3192	2.189708472662	2.3089	0.029763429199
577.14665	2.191524128982	2.3082	0.029067192221
579.58325	2.184802435272	2.3073	0.029805898884
581.4107	2.184890243556	2.3067	0.02870992971
583.23815	2.185306692374	2.306	0.030031157319
585.06559	2.186261077891	2.3054	0.028794480564
587.50219	2.192100021931	2.3045	0.029617318151
589.32964	2.185435918315	2.3039	0.02881657328
591.15709	2.186863406349	2.3033	0.029086579226
593.59369	2.186678540584	2.3025	0.029862045055
595.42114	2.185196011682	2.3019	0.02906069493
597.24859	2.181772339395	2.3013	0.029689046827
599.07604	2.18218189584	2.3007	0.029190396102
601.51263	2.183127282914	2.2999	0.027721432644
603.34008	2.179356414814	2.2993	0.028443297323
605.16753	2.189309778319	2.2988	0.028396370583
607.60413	2.186779961645	2.298	0.028218135452
609.43158	2.173323583877	2.2975	0.028267675088
611.25903	2.179423722739	2.2969	0.02889179145
613.08648	2.177644404099	2.2964	0.028278353395
615.52308	2.180137548989	2.2957	0.027272526035
617.35052	2.180620151686	2.2952	0.027738103764
619.17797	2.177027372489	2.2947	0.028119462632
621.00542	2.173156689346	2.2942	0.027404417869

λ (nm)	index ($V = 0$)	index ($V = \text{Applied}$)	k
623.44202	2.173883799245	2.2935	0.027305713974
625.26947	2.17989293822	2.293	0.027635389683
627.09692	2.179475106873	2.2925	0.027465910429
629.53352	2.185592040394	2.2919	0.027035194544
631.36097	2.168215958126	2.2914	0.026026853308
633.18842	2.172650790625	2.2909	0.027569972329
635.01586	2.173202410334	2.2904	0.026268829933
637.45246	2.174181573092	2.2898	0.02674623731
639.27991	2.176229755329	2.2893	0.026294592776
641.10736	2.164889544323	2.2889	0.026340120368
643.54396	2.174844716569	2.2883	0.026445817283
645.37141	2.172663435937	2.2878	0.026278612096
647.19886	2.178957488219	2.2874	0.026587905539
649.02631	2.16868444964	2.287	0.028383915752
651.4629	2.176746486213	2.2864	0.025702919695
653.29035	2.173289219561	2.2859	0.025552505524
655.1178	2.166357544031	2.2855	0.025541591091
657.5544	2.175280175351	2.2849	0.025852691809
659.38185	2.177850136368	2.2845	0.024734731358
661.2093	2.170548560355	2.2841	0.026540626906
663.03675	2.175102831575	2.2837	0.025807555118
665.47335	2.172607303241	2.2831	0.024717102527
667.3008	2.172155089829	2.2827	0.025636857576
669.12824	2.169962799807	2.2823	0.025207845949
671.56484	2.162078648812	2.2818	0.025506919331
673.39229	2.173205603574	2.2814	0.024661790652

λ (nm)	index ($V = 0$)	index ($V = \text{Applied}$)	k
675.21974	2.167413076397	2.281	0.02630575861
677.04719	2.162001422702	2.2806	0.025369020208
679.48379	2.168977307923	2.28	0.024264548093
681.31124	2.163138163318	2.2796	0.024254139542
683.13869	2.16902872799	2.2792	0.024374636952
685.57528	2.169269641001	2.2787	0.025776000858
687.40273	2.154264788399	2.2783	0.026447812887
689.23018	2.161039994855	2.2779	0.026034923451
691.05763	2.159770867746	2.2775	0.025316378965
693.49423	2.164054423597	2.277	0.023498716441
695.32168	2.163088338121	2.2766	0.025752554405
697.16007	2.164523676774	2.2762	0.024176896755
699.02035	2.164164354689	2.2758	0.025124714717
699.64044	2.165886613617	2.2757	0.025104436349

Bibliography

- [1] [Online]. Available: <http://www.chemie.hu-berlin.de/agrad/publications/Lycurgus.pdf>
- [2] [Online]. Available: <http://www.cvrl.org/>
- [3] [Online]. Available: <http://www.mtixtl.com/>
- [4] [Online]. Available: <http://www.tcd.ie/Physics/Surfaces/ellipsometry2.php>
- [5] Solgasmix-code with chemsage.
- [6] Srim 2003. [Online]. Available: <http://www.srim.org/>
- [7] (1966, 08). [Online]. Available: <http://www.startrek.com/startrek/view/series/TOS/episode/68672.html>
- [8] Color science: concepts and methods, quantitative data and formulae. Wiley, 1982.
- [9] Chemical Mechanical Planarization of Microelectronic Materials. John Wiley and Sons, 1997.
- [10] Properties of Lithium Niobate. INSPEC, Inc, 2002.
- [11] Properties of Lithium Niobate. The Institution of Engineering and Technology, 2002.
- [12] S. Aggarwal, S. Perusse, C. Tipton, R. Ramesh, H. Drew, T. Venkatesan, D. Romero, V. Podobedov, and A. Weber, Applied Physics Letters, vol. 73, p. 1973, 1998.
- [13] M. Alexe and U. Gösele, Wafer Bonding: Applications and Technology. Springer, 2004.
- [14] B. Aspar, M. Bruel, M. Zussy, and A. Cartier, Electronic Letters, vol. 32, p. 1985, 1996.
- [15] B. Aspar, H. Moriceau, E. Jalaguier, C. Lagahe, A. Soubie, B. Biasse, A. Papon, A. Claverie, J. Grisolia, G. Benassayag, F. Letertre, O. Rayssac, T. Barge, C. Maleville, and B. Ghyselen, Journal of Electronic Materials, vol. 30, p. 834, 2001.

- [16] J. Ayers, Heteroepitaxy of Semiconductors: Theory, Growth, and Characterization. CRC Press, 2007.
- [17] B. Barnes and R. Sambles, Physics World, vol. 19, p. 17, 2006.
- [18] D. Betancourt and C. del Rio, IEEE Sensor Array Workshop, p. 93, 2006.
- [19] S. Bhagat, H. Han, and T. Alford, Thin Solid Films, vol. 515, p. 1998, 2006.
- [20] M. Bohr, “Intel’s silicon research and development pipeline,” Intel, Tech. Rep., 2006.
- [21] S. Bozhevolnyi, V. Volkov, E. Devaux, J. Laluet, and T. Ebbesen, Nature, vol. 440, p. 508, 2006.
- [22] M. Bruel, Electronic Letters, vol. 31, p. 1201, 1995.
- [23] ———, Nuclear Instruments and Methods in Physics Research, vol. 108, p. 313, 1996.
- [24] BYU. (2009, 06). [Online]. Available: <http://ee.byu.edu/cleanroom/OxideTimeCalc.phtml>
- [25] K. Chen, A. Fan, C. Tan, R. Reif, and C. Wen, Applied Physics Letters, vol. 81, p. 3774, 2002.
- [26] K. Chen, C. Tan, A. Fan, and R. Reif, Electrochemical and Solid-State Letters, vol. 7, p. G14, 2004.
- [27] B. Cotterell and J. Rice, International Journal of Fracture, vol. 16, p. 155, 1980.
- [28] K. Crosby and R. Bradley, Physical Review E, vol. 59, p. R2542, 1999.
- [29] B. Derby and E. Wallach, Metal Science, vol. 16, p. 49, 1982.
- [30] ———, Metal Science, vol. 18, p. 427, 1984.
- [31] M. Dicken, L. Sweatlock, D. Pacifici, and H. Atwater, Nano Letters, vol. 8, p. 4048, 2008.
- [32] K. Diest, M. Archer, J. Dionne, Y. Park, M. Czubakowski, and H. Atwater, Applied Physics Letters, vol. 93, p. 092906, 2008.
- [33] K. Diest, J. Dionne, M. Spain, and H. Atwater, Nano Letters, vol. 9, p. 2579, 2009.
- [34] J. Dionne*, K. Diest*, L. Sweatlock, and H. Atwater, Nano Letters, vol. 9, p. 897, 2009.

- [35] J. Dionne, H. Lezec, and H. Atwater, Nano Letters, vol. 6, p. 1928, 2006.
- [36] J. Dionne, L. Sweatlock, and H. Atwater, Physical Review B, vol. 72, p. 075405, 2005.
- [37] J. Dionne, L. Sweatlock, H. Atwater, and A. Polman, Physical Review B, vol. 73, p. 035407, 2006.
- [38] A. Dmitriev and M. Shur, Journal of Applied Physics, vol. 103, p. 084511, 2008.
- [39] T. Ebbesen, H. Lezec, H. Ghaemi, T. Thio, and P. Wolff, Nature, vol. 391, p. 667, 1998.
- [40] G. Eriksson, Acta chemica Scandinavica, vol. 25, p. 2651, 1971.
- [41] P. Evans, G. Wurtz, W. Hendren, R. Atkinson, W. Dickson, A. Zayats, and R. Pollard, Applied Physics Letters, vol. 91, p. 043101, 2007.
- [42] M. Fejer, G. Magel, D. Jundt, and R. Byer, IEEE Journal of Quantum Electronics, vol. 28, p. 2631, 1992.
- [43] L. Freund, Applied Physics Letters, vol. 70, p. 3519, 1997.
- [44] L. Freund and S. Suresh, Thin Film Materials. Cambridge University Press, 2003.
- [45] R. Goldstein and R. Salganik, International Journal of Fracture, vol. 10, p. 507, 1974.
- [46] W. Han and J. Yu, Journal of Applied Physics, vol. 89, p. 6551, 2001.
- [47] A. Hill and E. Wallach, Acta Metallurgica, vol. 37, p. 2425, 1989.
- [48] C. Himcinschi, M. Reiche, R. Scholz, S. H. Christiansen, and U. Gösele, Applied Physics Letters, vol. 90, p. 231909, 2007.
- [49] J. Hodgdon and J. Sethna, Physical Review B, vol. 47, p. 4831, 1993.
- [50] R. Hopkins and A. Rohatgi, Journal of Crystal Growth, vol. 75, p. 67, 1986.
- [51] H. Huntington, The Elastic Constants of Crystals. Academic, 1958.
- [52] J. Hutchinson and Z. Suo, Advanced Applied Mechanics, vol. 29, p. 63, 1991.
- [53] H. Iwai, Solid-State Electronics, vol. 48, p. 497, 2004.

- [54] T. Izuhara, I. Gheorma, R. Osgood, A. Roy, H. Bakhru, Y. Tesfu, and M. Reeves, Applied Physics Letters, vol. 82, p. 616, 2003.
- [55] R. Jacobsen, K. Andersen, P. Borel, J. Fage-Pedersen, L. Frandsen, O. Hansen, M. Kristensen, A. Lavrineko, G. Moulin, H. Ou, C. Peucheret, B. Zsigri, and A. Bjarklev, Nature, vol. 441, p. 199, 2006.
- [56] B. Johnson, “Caltech lecture notes on statistical mechanics,” March 2005.
- [57] M. Jutzi, M. Berroth, G. Wohl, M. Oehme, and E. Kasper, IEEE Photonics Technology Letters, vol. 17, p. 1510, 2005.
- [58] B. Kim, J. An, and K. Hwang, Journal of Materials Science, vol. 41, p. 2165, 2006.
- [59] I. Kim, Y. Avrahami, H. Tuller, Y. Park, M. Dicken, and H. Atwater, Applied Physics Letters, vol. 86, p. 192907, 2005.
- [60] E. Kretschmann and H. Raether, Zeitschrift fur Naturforschung, vol. 23A, p. 2135.
- [61] M. Kuijk and R. Vounckx, Journal of Applied Physics, vol. 66, p. 1544, 1989.
- [62] H. Larralde and J. Rice, Europhysics Letters, vol. 30, p. 87, 1995.
- [63] E. Laux, C. Genet, T. Skauli, and T. Ebbesen, Nature Photonics, vol. 2, p. 161, 2008.
- [64] C. Lee, M. Dupeux, and W. Tuan, Materials Science and Engineering: A, vol. 467, p. 125, 2007.
- [65] M. Levy, R. Osgood, R. Liu, L. Cross, G. Cargill, A. Kumer, and H. Bakhru, Applied Physics Letters, vol. 73, p. 2293, 1998.
- [66] H. Lezec, J. Dionne, and H. Atwater, Science, vol. 316, p. 430, 2007.
- [67] A. Lien, C. Cai, R. John, J. Galligan, and J. Wilson, Displays, vol. 22, p. 9, 2001.
- [68] A. Liu, R. Jones, L. Liao, D. Samara-Rubio, D. Rubin, O. Cohen, R. Nicolaescu, and M. Paniccia, Nature, vol. 427, p. 615, 2004.
- [69] J. Liu, M. Beals, A. Pomerene, S. Bernardis, R. Sun, J. Cheng, L. Kimerling, and J. Michel, Nature Photonics, vol. 2, p. 433, 2008.

- [70] S. Liu and M. Xiao, Applied Physics Letters, vol. 88, p. 143512, 2006.
- [71] S. Maier, Plasmonics: Fundamentals and Applications. Springer, 2007.
- [72] G. Mie, “Beiträge zur optik trüber medien, speziell kolloidaler metallösungen,” Annalen Der Physik, vol. 25, p. 377, 1908.
- [73] D. Miller, Proceedings of the IEEE, vol. 88, p. 728, 2000.
- [74] K. Mitani and U. Gösele, Applied Physics A, vol. 54, p. 543, 1999.
- [75] A. Movchan, H. Gao, and J. Willis, International Journal of Solids and Structures, vol. 35, p. 3419, 1998.
- [76] Z. Munir, Journal of Materials Science, vol. 14, p. 8, 1979.
- [77] ———, Powder Metallurgy, vol. 24, p. 177, 1981.
- [78] T. Nason, G. Yang, K. Park, and T. Lu, Journal of Applied Physics, vol. 70, p. 1392, 1991.
- [79] J. Nye, Physical Properties of Crystals, Their Representation by Tensors and Matrices. Oxford University Press, 2000.
- [80] A. Okyaym, A. Pethe, D. Kuzum, S. Latif, D. Miller, and K. Saraswat, Optics Letters, vol. 32, p. 2022, 2007.
- [81] R. Oriani, Annual Review of Materials Science, vol. 8, p. 327, 1978.
- [82] A. Otto, Zeitschrift fur Physik, vol. 216, p. 398, 1968.
- [83] E. Ozbay, Science, vol. 311, p. 189, 2006.
- [84] D. Pacifici, H. Lezec, and H. Atwater, Nature Photonics, vol. 1, p. 402, 2007.
- [85] ———, Physical Review B, vol. 77, p. 115411, 2008.
- [86] H. Park, C. Barrelet, Y. Wu, B. Tian, F. Qian, and C. Lieber, Nature Photonics, vol. 2, p. 622, 2008.
- [87] Y. Park, K. Diest, and H. Atwater, Journal of Applied Physics, vol. 102, p. 074112, 2007.
- [88] Y. Park, B. Min, K. Vahala, and H. Atwater, Advanced Materials, vol. 18, p. 1533, 2006.

- [89] Y. Park, P. Nardi, X. Li, and H. Atwater, Journal of Applied Physics, vol. 97, p. 074311, 2005.
- [90] Y. Park, J. Ruglovsky, and H. Atwater, Applied Physics Letters, vol. 85, p. 455, 2004.
- [91] G. Parry, A. Cimetière, C. Coupeau, J. Jolin, and J. Grilhé, Physical Review E, vol. 74, p. 066601, 2006.
- [92] J. Pendry, D. Schurig, and D. Smith, Science, vol. 312, p. 1780, 2006.
- [93] D. Polla and L. Francis, Annual Review of Materials Science, vol. 28, p. 563, 1998.
- [94] L. Ponson, K. Diest, H. Atwater, G. Ravichandran, and K. Bhattacharya, Journal of Applied Physics, vol. 105, p. 073514, 2009.
- [95] C. Qian and B. Terreault, Journal of Applied Physics, vol. 90, p. 5152, 2001.
- [96] I. Radu, I. Szafraniak, R. Scholz, M. Alexe, and U. Gösele, Journal of Applied Physics, vol. 94, p. 7820, 2003.
- [97] H. Raether, Surface Plasmons on Smooth and Rough Surfaces and on Gratings. Springer-Verlag, 1988.
- [98] G. Reed and C. Png, Materials Today, vol. 8, p. 40, 2005.
- [99] R. Ritchie, Physical Review, vol. 106, p. 874, 1957.
- [100] R. Ritchie, E. Arakawa, J. Cowan, and R. Hamm, Physical Review Letters, vol. 21, p. 1530, 1968.
- [101] L. Robins, D. Kaiser, L. Rotter, P. Schenck, G. Stauf, and D. Rytz, Journal of Applied Physics, vol. 76, p. 7487, 1994.
- [102] B. Rodriguez, “Nanoscale investigation of the piezoelectric properties of perovskite ferroelectrics and iii-nitrides,” Ph.D. dissertation, North Carolina State University, 2003.
- [103] J. Ruglovsky, J. Li, K. Diest, K. Bhattacharya, and H. Atwater, Acta Materialia, vol. 54, p. 3657, 2006.
- [104] S. Sass, The Substance of Civilization: Materials and Human History From the Stone Age to the Age of Silicon. Arcade Publishing, 1998.

- [105] J. Scott and C. P. de Araugo, Science, vol. 264, p. 1400, 1989.
- [106] A. Sommerfeld, Annalen der Physik und Chemie, vol. 67, p. 233, 1899.
- [107] R. Soref and B. Bennett, IEEE Journal of Quantum Electronics, vol. 23, p. 123, 1987.
- [108] L. Sweatlock, “Plasmonics: Numerical methods and device applications,” Ph.D. dissertation, California Institute of Technology, 2008.
- [109] L. Sweatlock, S. Maier, H. Atwater, J. Penninkhof, and A. Polman, Physical Review B, vol. 71, p. 235408, 2005.
- [110] I. Szafraniak, I. Radu, R. Scholz, M. Alexe, and U. Gösele, Integrated Ferroelectrics, vol. 55, p. 983, 2003.
- [111] M. Taylor, D. Readey, C. Teplin, M. van Hest, J. Alleman, M. Dabney, L. Gedvilas, B. Keyes, B. To, and J. P. D. Ginley, Measurement Science Technology, vol. 16, p. 90, 2005.
- [112] J.-C. Tolédano and P. Tolédano, The Landau Theory of Phase Transitions, ser. World Scientific Lecture Notes in Physics. World Scientific, 1987, vol. 3.
- [113] J. Tominaga, C. Mihalcea, D. Buchel, H. Fukuda, T. Nakano, N. Atoda, H. Fuji, and T. Kikukawa, Applied Physics Letters, vol. 78, p. 2417, 2001.
- [114] Q. Tong and U. Gösele, Semiconductor Wafer Bonding: Science and Technology. John Wiley and Sons, 1999.
- [115] Q. Tong, K. Gutjahr, S. Hopfe, U. Gösele, and T. Lee, Applied Physics Letters, vol. 70, p. 1390, 1997.
- [116] K. Uchino, Ferroelectric Devices. Marcel Dekker, Inc., 2000.
- [117] N. van Hulst, Nature Photonics, vol. 2, p. 139, 2008.
- [118] G. Veronis and S. Fan, Optics Express, vol. 3, p. 1211, 2007.
- [119] Y. Vlasov, M. O’Boyle, H. Hamann, and S. McNab, Nature, vol. 438, p. 65, 2005.
- [120] Y. Wang, Applied Physics Letters, vol. 67, p. 2759, 1995.
- [121] M. Weldon, M. Collot, Y. Chabal, V. Venezia, A. Agarwal, T. Haynes, D. Eaglesham, S. Christman, and E. Chaban, Applied Physics Letters, vol. 73, p. 3721, 1998.

- [122] M. Weldon, V. Marsico, Y. Chabal, A. Agarwal, D. Eaglesham, J. Sapjeta, W. Brown, D. Jacobson, Y. Caudano, S. Christman, and E. Chaban, Journal of Vacuum Science and Technology, vol. B15, p. 1065, 1997.
- [123] M. Wiegand, M. Reiche, and U. Gösele, Journal of The Electrochemical Society, vol. 147, p. 2734, 2000.
- [124] Q. Xu, B. Schmidt, S. Pradhan, and M. Lipson, Nature, vol. 435, p. 325, 2005.
- [125] Y. Xu, Ferroelectric Materials and Their Applications. Elsevier, 1991.
- [126] H. Yu and J. Hutchinson, International Journal of Fracture, vol. 113, p. 39, 2002.
- [127] J. Zahler, C. Ahn, S. Zaghi, H. Atwater, C. Chu, and P. Iles, Thin Solid Films, vol. 403, p. 558, 2002.
- [128] J. Zenneck, Annalen Der Physik, vol. 23, p. 846, 1907.
- [129] X. Zhang and J. Raskin, Electrochemical and Solid-State Letters, vol. 7, p. G172, 2004.